Technische Universität München
Max-Planck-Institut für Astrophysik

Progenitor systems of Type Ia Supernovae: mergers of white dwarfs and constraints on hydrogen-accreting white dwarfs

Rüdiger M. Pakmor

Vollständiger Abdruck der von der Fakultät für Physik der Technischen Universität München zur Erlangung des akademischen Grades eines

Doktors der Naturwissenschaften (Dr. rer. nat.)

genehmigten Dissertation.

Vorsitzender: Univ.-Prof. Dr. R. Krücken

Prüfer der Dissertation:

1. Priv.-Doz. Dr. F. K. Röpke
2. Univ.-Prof. Dr. H. Friedrich

Die Dissertation wurde am 19.07.2010 bei der Technischen Universität München eingereicht und durch die Fakultät für Physik am 14.12.2010 angenommen.

Contents

List of Figures

List of Tables

1 Introduction

Most objects on the sky appear static when observed at human timescales, as they evolve on timescales of millions to billions of years. Thus, we will never be able to observe the evolution of a star or a galaxy directly. So we have to observe most objects as the are and try to infer their past and future by comparison with other, similar but newer and older objects. There are, however, objects that appear and disappear again on timescales of days, months or years. Supernovae are among the most spectacular ones and humans have noticed and described them already a thousand years ago. If they are located in the Milky Way they appear as luminous very bright stars on the sky. Some of the most famous historical supernovae, e.g. SN 1006 and SN 1054 have been observed and documented by astronomers on different continents providing an opportunity to historians to synchronize calendars of different civilizations.

Supernovae are magnificent events. Their properties are extreme in every sense. Within a second, they release a staggering amount of energy, similar to the energy the sun produces over its whole lifetime. This energy release causes a powerful explosion, that ejects material of the order of the mass of the sun at velocities up to tens of thousands kilometers per second. A small fraction of this energy is released in the form of light and powers the visual display of the supernova. Figure 1.1 shows supernova SN 1994D in the outskirts of disk galaxy NGC 4526. The supernova is as bright as the center of the galaxy. In the explosion itself temperatures of several billion Kelvin are reached that lead to explosive nucleosynthesis. This way, supernovae have produced virtually all heavy elements and thus shaped the Universe.

As supernovae are subject to such extremes, they probe physical conditions that are not accessible on Earth. While this enables us to use them to learn about the laws of Nature in regimes we could not test otherwise, it also makes it very challenging to understand supernovae from a theoretical point of view. Since there are many different physical processes

Figure 1.1: Supernova 1994D in the outskirts of disk galaxy NGC 4526. (Credit: NASA)

involved that interact with each other in very complex ways, supernovae elude any simple theoretical description. However, it is possible to use numerical models which incorporate the relevant physics to try to understand the properties of supernovae we observe. In principle they allow to follow the evolution of complex systems if we know the initial state of the system and model the physical processes involved adequately.

To model supernovae, it is necessary to account for many different areas of physics including hydrodynamics, nuclear reactions, equations of state of extremely dense and arbitrarily degenerate matter, radiative transfer, and many more. Unfortunately, some of these are not completely understood themselves, let alone their combination. At the same time, it is not even feasible to model all physical processes as good as possible in a numerical model that includes all of them due to constrains in computational resources. Thus, to understand a supernova in which processes of different physical areas act at the same time in numerical models we have to use approximations to the basic laws of Nature. In addition, we do not know the initial conditions from which supernovae arise in detail. Nevertheless, as shown in this thesis, we are able to understand qualitatively how some of these events work and even do quantitative tests of our models.

Beside being fascinating objects in their own right, supernovae are directly connected to several other fields of astrophysics. They play an important role in the evolution of galaxies and they are the key to the chemical evolution of the Universe. Supernovae of

type Ia, a specific species of supernovae, are one of the most important tools in cosmology. Due to their brightness, they can be seen in galaxies far away from which it took the light billions of years to reach us. Therefore, they enable us to probe the Universe at it was billions of years younger. A special property of type Ia supernovae is that their intrinsic brightness can be inferred without knowing their distance. This makes them a great tool to measure cosmological distances and led to the discovery of the accelerated expansion of the Universe ten years ago. Since then, this discovery has been confirmed by independent approaches. Today, type Ia supernovae are still one of the most important tools in cosmology and one of the most promising ways to determine the equation of state of dark energy and thus to understand what the dominant constituent of our Universe really is.

For all the reasons described above, it is important to understand where type Ia supernovae come from and how they explode. Today, however, neither the progenitor systems are known nor the explosion mechanism of type Ia supernovae is understood. The goal of this thesis is to shed some light on both. There are two different progenitor scenarios that have been proposed for type Ia supernovae. Using two different approaches, we address both using partially the same methods. We study mergers of two carbon/oxygen white dwarfs which have been proposed as progenitors of type Ia supernovae a long time ago, but yet have not been shown to be able to lead to such an explosion. Showing how such mergers can explode as a type Ia supernova is necessary to proof the viability of this scenario in general and might provide insights on how to decide the question for the progenitor systems of type Ia supernovae observationally. In addition, we study the impact of a type Ia supernova explosion on potential companion stars in a binary system which is one of the most promising diagnostics to finally decide which of the proposed progenitor scenarios of type Ia supernovae is realized in Nature.

This thesis is organized in four parts. Chapter 2 provides an overview about the observational properties of type Ia supernovae and their current theoretical understanding. Chapter 3 presents several models of mergers of white dwarfs and discusses how they might lead to type Ia supernova explosions. To learn about the progenitor systems of type Ia supernovae, Chapter 4 covers several simulations of impacts of the ejecta of type Ia supernova explosions on binary companions. In Chapter 5 the numerical codes used in this work are described. Finally, Chapter 6 summarizes this work.

2 Type Ia supernovae

2.1 Observational properties

2.1.1 Classification

Supernovae are divided into different classes on a purely observational basis. Spectral properties, in particular the presence of hydrogen, helium and silicon lines define their type. Figure 2.1 gives an overview of the classification scheme. If early (pre maximum brightness) spectra show hydrogen lines, the supernova is called type II, otherwise type I. Type I supernovae are subdivided into three classes. Type Ia supernovae show silicon lines. If the spectrum of a supernova shows no silicon but helium lines, it is a type Ib supernova. If it shows neither of them, it is called type Ic supernova.

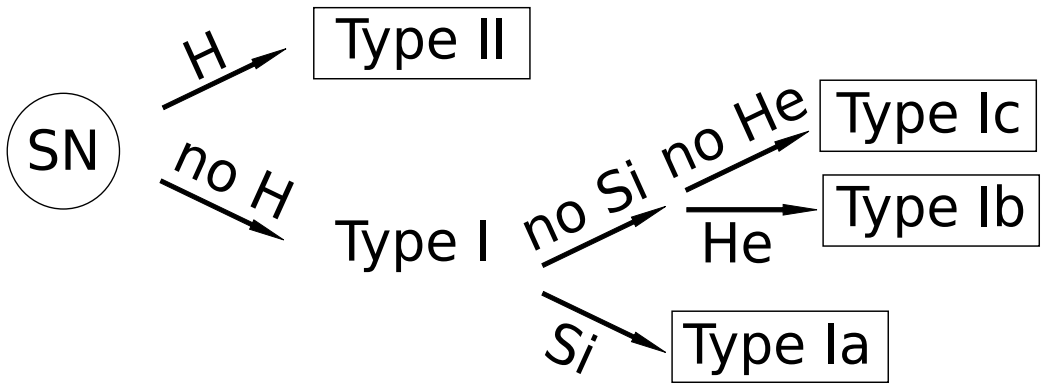

Figure 2.1: Supernova classification scheme

The classification itself does not consider the nature of the exploding object or the physi-

cal mechanism behind the explosion. There is, however, general agreement that type Ib/Ic and type II supernovae share the same explosion mechanism and that it is fundamentally different from the explosion mechanism of type Ia supernovae.

The former are associated with the death of massive stars ($M \gtrsim 8 - 10 M_{\odot}$). After their core has been burned to iron, nuclear burning stops and the nuclear energy release ceases. However, this energy release has maintained the pressure in the center of the star which stabilized the core against the pull of its own gravity so far. Consequently, the iron core collapses forming a neutron star or a black hole. The collapse releases enough gravitational binding energy to blow apart the outer shells of the star in a supernova explosion. However, most of the energy is released in the form of neutrinos. After the explosion only the core of the star remains in the form of a neutron star or a black hole. This basic picture is supported by several kinds of observational evidence. First, for a small number of nearby core collapse supernovae the progenitor star has been identified on pre-explosion images (see, e.g. Sonneborn et al., 1987; Maund et al., 2005; Mattila et al., 2008; Maund & Smartt, 2009). For the closest supernova explosion in modern astronomy, SN 1987A in the Large Magellanic Cloud, even the neutrino signal was detected confirming the scenario (see, e.g. Arafune & Fukugita, 1987). So far, core collapse supernovae have only been found in young stellar populations or galaxies that show recent star formation, supporting the picture of massive progenitor stars with short lifetimes. The theoretical understanding of the development of the explosion is still incomplete, as the problem is very demanding (for the current state of knowledge see e.g. Janka et al., 2007; Marek & Janka, 2009).

Type Ia supernovae, in contrast, are found in all types of galaxies and in stellar populations of vastly different ages (100Myrs to a few Gyrs) and, as far as we know, leave no compact remnant behind. Therefore they cannot originate from the death of massive stars and gravitational binding energy can be excluded as the main power source of these explosions. Unfortunately, there is no direct detection of a progenitor system of a type Ia supernova yet, so their progenitor system is still a matter of debate.

As we are only interested in type Ia supernovae in this work, we will discuss their observational properties and our current theoretical picture of their progenitors and explosion mechanism in detail.

2.1.2 Lightcurves

Type Ia supernovae lightcurves in general look rather similar. Their luminosity rises steeply for about 20 days until it peaks (Riess et al., 1998b). After that it declines slowly and eventually turns into an exponential decline until the supernova becomes invisible for us typically after several months (A few supernovae, however, have been followed to much later times, e.g. SN 2003du up to 480d [Stanishev et al. (2007)]). Type Ia supernovae are, on average, brighter than core collapse supernovae, with a typical maximum luminosity between −18.5mag and −19.5mag. The shape of the lightcurves can be modeled very well under the assumption that its dominant source of power is the radioactive decay of ^{56}Ni via

^{56}Co to ^{56}Fe (e.g., Arnett, 1982; Woosley et al., 2007). Before type Ia supernovae reach their maximum brightness, most of the radiation that emerges from the decay of ^{56}Ni is trapped within the ejecta, because of high density of the ejecta that leads to high opacity. At the time type Ia supernovae reach their peak luminosity, most of the original ^{56}Ni ($\tau_{1/2}$ = 6d) has already decayed to ^{56}Co and the decay of ^{56}Co ($\tau_{1/2}$ = 77d) now powers the light curve.

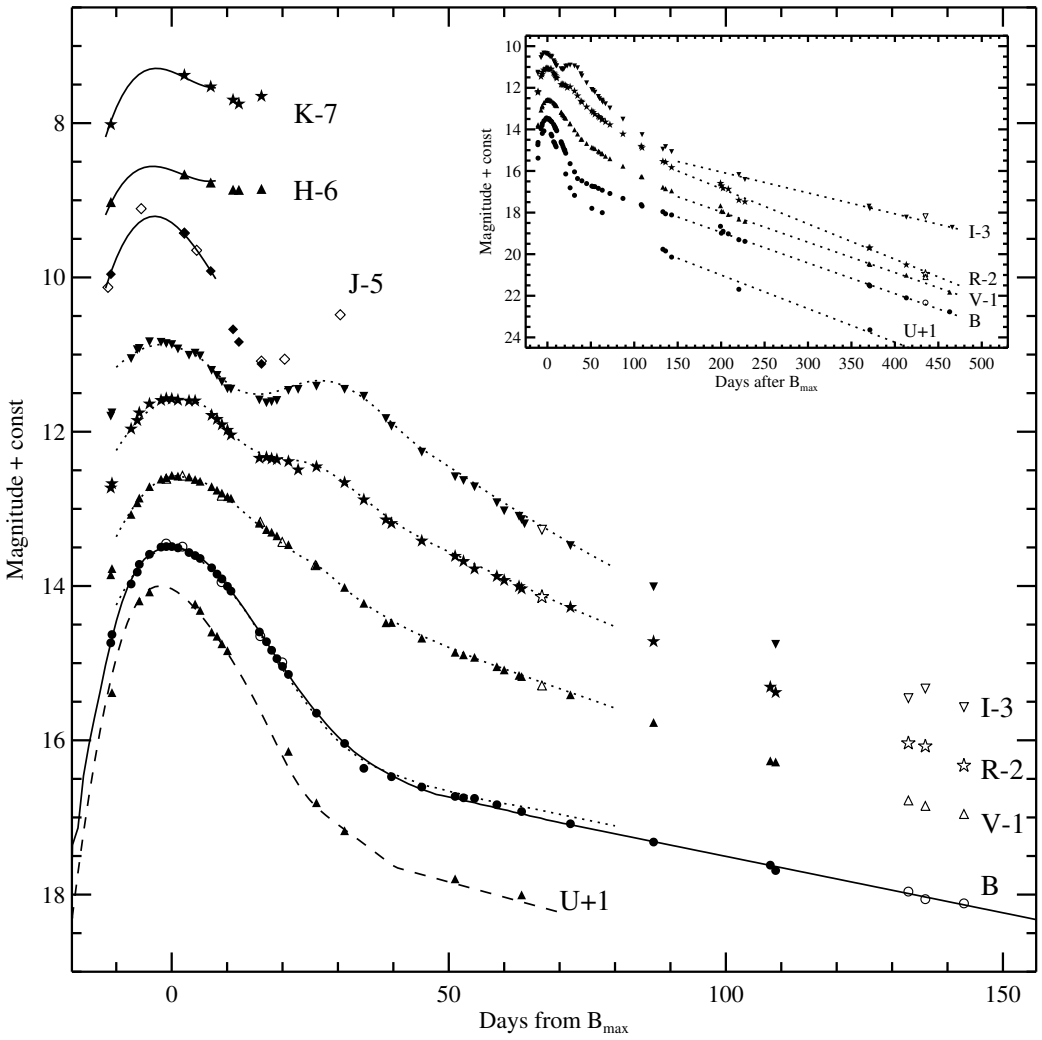

Figure 2.2: Lightcurves of SN 2003du in UBVRIJHK bands taken from Stanishev et al. (2007). The symbols show observational data points. Over-plotted lines show template fits to the lightcurves of different bands. The subpanel in the upper right part of the plot shows the same plot extended to very late times. An arbitrary offset is added to the magnitude of the lightcurves.

Lightcurves of type Ia supernovae are usually observed in different broad-band filters that cover the whole range from optical to near-infrared radiation. Figure 2.2 shows color lightcurves of SN 2003du, a well observed type Ia supernova with prototypical lightcurves and spectra. One distinct feature of light curves of normal type Ia supernovae is the second peak in the I-band, that can be seen nicely here.

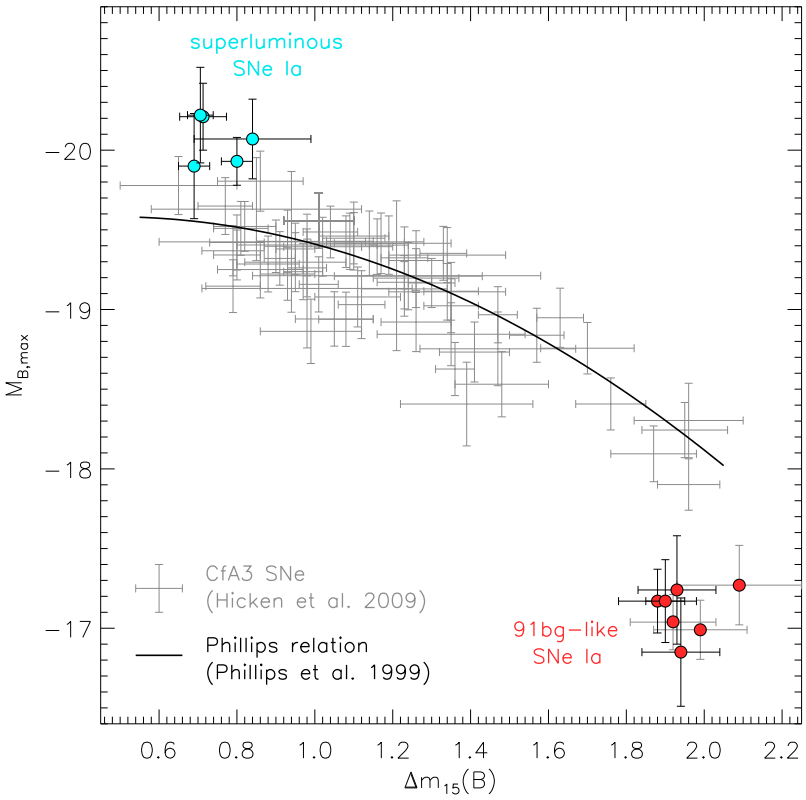

Figure 2.3: Relation between B-band brightness and light curve width for type Ia supernovae. The width of the lightcurves is measured by the decline of the light curve from the time it reaches its maximum luminosity until 15 days later. Gray crosses show supernovae from the Hicken et al. (2009) sample. The black line shows a fit to the relation of Phillips et al. (1999). Light blue and red points show superluminous and subluminous type Ia supernovae (Taubenberger et al., 2008). Both groups do not follow the relation, pointing to the possibility of different progenitors or explosion mechanisms. (courtesy: S. Taubenberger)

Probably the most remarkable property of type Ia supernovae is the existence of a relation between their absolute brightnesses and the width of their lightcurves. Figure 2.3 shows the relation for a large number of nearby events whose distance is known as the distance to their host galaxy is known. Thus their absolute brightness can be determined. Basically, more luminous supernovae have broader lightcurves. This can be understood in terms of the amount of ^{56}Ni in the ejecta. The more ^{56}Ni the ejecta contain, the brighter the supernova is. However, more ^{56}Ni also increases the amount of iron group elements, the dominant source of opacity, thus broadening the light curve. This relation allows us to determine the intrinsic brightness of a supernova from the shape of its light curve only. The intrinsic luminosity can in turn be used to measure the distance to the object. Therefore, together with an independent identification of their redshift, it is possible to use type Ia supernovae to probe the expansion history of the Universe. This lead to the discovery that the expansion of the universe is accelerating by Riess et al. (1998a) and Perlmutter et al. (1999).

2.1.3 Spectra

The class of type Ia supernovae is defined by their spectral properties. Most type Ia supernovae are spectroscopically similar (≈ 70% according to Li et al., 2001). Around the time they reach their maximum brightness, their spectra are dominated by absorption lines from intermediate mass elements (silicon, sulfur, magnesium, calcium). Later, these lines become weaker and absorption lines of iron group elements develop. This can be understood as an effect of the expansion of the ejecta. While the ejecta expand their opacity drops, allowing us to look deeper into the core of the ejecta, as the outer layers of the ejecta become optically thin first.

As the ejecta move with a high velocity (typical line velocities are in the range of 10000 – 20000km s^{-1}), the position of the lines are redshifted. This allows us to infer the velocity of the ejecta from spectra. Moreover, it is possible to use the temporal evolution of the spectra to reconstruct the radial composition of the ejecta via abundance tomography (Stehle et al., 2005; Hachinger et al., 2009). At late times (typically several months after maximum brightness), the ejecta reach the nebular phase, i.e. they become completely transparent for optical radiation. At that time, the spectrum is dominated by emission rather than absorption lines.

An important feature of spectra of type Ia supernovae is the absence of hydrogen and helium absorption or emission lines. In the nebular phase, the absence of hydrogen emission lines can be used to place tight constrains ($M_H < 0.01 M_\odot$) on the amount of hydrogen contained in the supernova ejecta (Mattila et al., 2005; Leonard, 2007).

Light curve and spectral information together can be used to estimate the amount ^{56}Ni of the explosion and their total ejecta mass (Arnett, 1982). Note however, that in particular the estimate of the total ejecta mass carries large uncertainties.

2.1.4 Subclasses

As indicated above, not all type Ia supernovae look completely alike. This has lead to further discrimination into subclasses. These differ mainly in their brightness, but also in their spectroscopic features. Most type Ia supernovae are **normal** ones, as defined by Branch et al. (1993). According to Li et al. (2001) they make up about 64% of all type Ia supernova events. With a peak brightness of –18.7mag to –19.4mag and a B-band decline rate of $\Delta m_{15}(B) = 0.9$ to 1.6 they follow the Phillips relation (Phillips et al., 1999). Normal type Ia supernovae contain approximately $0.4 M_\odot$ .. $0.8 M_\odot$ of ^{56}Ni, as inferred from light curve modeling. They are found in all types of host galaxies.

Just slightly brighter than the bright end of normal type Ia supernovae, there is the group of **1991T-like** objects, named after their prototype, SN 1991T (Phillips et al., 1992). These supernovae peak around –19.6mag, with a decline rate of $\Delta m_{15}(B) = 0.75$ .. 1.0. They also obey the Phillips relation. To power their lightcurves, approximately $1.0 M_\odot$ of ^{56}Ni is

needed (Mazzali et al., 1995). At the same time, 1991T-like objects are also spectroscopically peculiar, as their early spectra show Fe III lines (Mazzali et al., 1995). However, at later times their spectra look normal. About 20% of all type Ia supernovae are 1991T-like objects (Li et al., 2001). They are located mostly in spiral galaxies, indicating that they are connected to recent star formation.

Even brighter are the so-called **superluminous** objects. They reach peak luminosities up to −20mag (Yamanaka et al., 2009) and their lightcurves decline only very slowly with $\Delta m_{15}(\mathrm{B}) \approx 0.7$. As shown in Figure 2.3, they do not follow the Phillips relation. To explain their luminosity, considerably more than one solar mass of ^{56}Ni is necessary. Estimates from light curve modeling range between $1.3\mathrm{M}_{\odot}$ for SN 2003fg (Howell et al., 2006) up to $1.7\mathrm{M}_{\odot}$ for SN 2009dc (Silverman et al., 2010). At the same time, they show low to very low line velocities. Sim et al. (2007) showed that the peak luminosity may also be a result of an aspheric distribution of ^{56}Ni in the ejecta. This configuration, however, has problems to explain the overall shape of the lightcurve, which is much broader than the lightcurves of normal type Ia supernovae, thus considerably more energy is required to power it. It is also in disagreement with spectropolarimetry observations of SN 2009dc (Tanaka et al., 2010) showing that the ejecta are spherically symmetric. The main characteristic of this subclass is their brightness, spectroscopically they are not a homogeneous group. Today, despite their brightness, only a handful superluminous type Ia supernovae have been found, indicating that these are rare events. There seems to be a tendency for superluminous type Ia supernovae to occur in regions of recent star formation (Silverman et al., 2010), but its significance is unclear. As the galaxies in which these supernovae are found tend to be ignored in supernova surveys, their rareness may be a selection effect.

On the other end of the luminosity distribution of type Ia supernovae the group of subluminous **1991bg-like** (Leibundgut et al., 1993) objects can be found. With a peak luminosity of −16.9mag to −17.9mag they are fainter than normal type Ia supernovae and their lightcurves decline considerably faster with a decline rate of $\Delta m_{15}(\mathrm{B}) = 1.8$ to 1.95. They do not obey the Phillips relation, as shown in Figure 2.3. Their ejecta contain only about $0.1\mathrm{M}_{\odot}$ of ^{56}Ni (Mazzali et al., 1997). It is interesting to note, that there seems to be a gap in the luminosity distribution between normal and 1991bg-like supernovae, which may be an indication of different progenitor systems or explosion mechanisms at work. The group of 1991bg-like supernovae has very similar spectra (Taubenberger et al., 2008), which show some differences to normal type Ia supernovae, most notably a strong Ti II absorption. Their line velocities are low compared to normal type Ia supernovae, but not as low as in superluminous events. According to Li et al. (2001), about 16% of all type Ia supernovae are 1991bg-like events. This estimate, however, carries large uncertainties as most supernovae surveys are magnitude limited and thus favor luminous over subluminous events. Therefore, to estimate the overall rate of 1991bg-like objects, their observed rate has to be corrected for that. 1991bg-like supernovae seem to occur predominantely in old elliptical galaxies (Sullivan et al., 2006), pointing to old progenitor systems.

2.1.5 Polarization

As nearly all supernovae we observed in recent times (with the exception of SN 1987A) are too far away to resolve them spatially, and we are only able to see them from one line of sight, it is not possible to learn about the geometry of the ejecta directly. There is, however, the possibility to use spectropolarimetry to infer their geometry indirectly. Basically, there are two different sorts of inhomogeneities that cause polarization. Asymmetries of the inner part of the ejecta, below the photosphere, lead to continuum polarization. Inhomogeneities in the outer layers, above the photosphere, will result in line polarization. Unfortunately, only few spectropolarimetry observations of type Ia supernovae exist (Wang & Wheeler, 2008), as they are observationally very expensive. These show that normal type Ia supernovae have only a very low degree of polarization, if any. This leads to the conclusion, that most of the ejecta of normal type Ia supernovae are rather spherical and do not show large-scale asymmetries (Wang et al., 2007). They show, however, polarization in some lines, which indicates that the structure of the outer parts of the supernova ejecta (above the photosphere) is somewhat clumpy. Of the other subclasses of type Ia supernovae, only for two objects spectropolarimetry observations exist. SN 2009dc, a superluminous type Ia supernova, is very similar to normal objects. It shows nearly no continuum polarization, but a small amount of line polarization (Tanaka et al., 2010). The only 1991bg-like supernova for which we have spectropolarimetry, SN 1999by, however, looks very different. Its continuum is highly polarized, suggesting a strong global asymmetry of the ejecta (Howell et al., 2001). This can be seen as another hint for 1991bg-like supernovae being fundamentally different from normal ones.

2.2 Theoretical description

There is general agreement that type Ia supernovae are thermonuclear explosion in degenerate matter, as proposed already by Hoyle & Fowler (1960). The ejected mass being of the order of one solar mass, the fact that type Ia supernovae do not leave any compact remnant behind, and their delay times, i.e. the time between the formation of the progenitor system and the explosion of the supernovae, up to several Gyrs leave only white dwarfs as progenitor stars.

Of the three known types of white dwarfs (helium, carbon/oxygen and oxygen/neon), helium white dwarfs can be excluded as they can not be more massive than $\approx 0.45 M_{\odot}$, since helium burning starts at the center otherwise. Oxygen/neon white dwarfs can be excluded for several type Ia supernovae, as they show carbon lines. Also, there are arguments against them from the point of view of explosion mechanisms, as discussed later. However, they can not be completely excluded and may contribute to a minor fraction of all type Ia supernovae.

Thus, at least a large majority of all type Ia supernovae will be exploding carbon/oxygen white dwarfs. Single white dwarfs are born with masses below the Chandrasekhar-mass ($\approx 1.38 M_{\odot}$) (Chandrasekhar, 1931), thus they are stable forever. Therefore, the explosion has ultimately to be caused externally, that is by a companion star in a binary system. As the

companion star interacts with the white dwarf via mass transfer, there are two possibilities that can lead to an explosion. Either the white dwarf accretes enough mass to approach the Chandrasekhar mass and thus becomes unstable. Or the mass transfer directly causes an ignition of the white dwarf.

This leads to the two most important questions of type Ia supernova theory:

I) What explodes? How massive is the white dwarf and what is the nature of its companion?

II) How does it explode? What causes the actual thermonuclear explosion?

Both questions, that of the progenitor system and that of the explosion mechanism of type Ia supernovae still lack a definite answer. It is not even excluded that there are different types of progenitor systems and/or explosion mechanisms at work. In the following we will discuss possible progenitor systems and explosion mechanisms.

2.2.1 Progenitor systems

Progenitor systems can be categorized according to the nature of the companion star. It is common practice to distinguish two different types of progenitor systems, the **single degenerate scenario** and the **double degenerate scenario**. In the former the companion is a main sequence star, a red giant or a helium star that transfers either hydrogen-rich material or pure helium to the white dwarf. In the double degenerate scenario the companion is a carbon/oxygen or helium white dwarf. For a general overview on progenitor systems and observational constraints, see Livio (2000).

The **single degenerate scenario** has first been proposed by Iben & Tutukov (1984). In its most widely discussed version, the white dwarf accretes hydrogen-rich material from its companion star. The hydrogen is then burned to helium first and further to carbon on the surface of the white dwarf, increasing the mass of the carbon/oxygen white dwarf. As the mass of the white dwarf approaches the Chandrasekhar-mass, the white dwarf becomes unstable and explodes (for the mechanism, see chapter 2.2.2).

Carbon/oxygen white dwarfs are born with typical masses of about $0.7M_\odot$ (but up to $1.2M_\odot$ in the most extreme case). Hence, to reach the Chandrasekhar-mass, a white dwarf has to accrete several tenths of a solar mass of material and convert it to carbon. Accretion can happen either as Roche-lobe overflow, from a main sequence or red giant companion that evolves and grows to fill its Roche-lobe, or via winds if the companion is a red giant. As Nomoto & Kondo (1991) showed, stable hydrogen burning can only be sustained for an accretion rate of $\approx 10^{-7} M_\odot\ \mathrm{yr}^{-1}$. If the accretion rate is too low, the hydrogen will burn in flashes which expel at least as many material as has been accreted. Therefore, the white dwarf does not grow. If the accretion rate is too large, carbon will be ignited on the surface of the white dwarf, and the carbon/oxygen white dwarf is converted into an oxygen/neon

white dwarf. This again is expected to collapse to a neutron star, rather than explode when it reaches the Chandrasekhar mass (Saio & Nomoto, 1985). The strong constrains on the accretion rate, however, reduce the expected supernova rate from this scenario. To increase the rate, Hachisu et al. (1999) proposed that an optically thick wind may originate from the accreting white dwarf, which stabilizes the mass transfer. It is, however, not yet clear whether such a wind really exists.

Population synthesis studies are used to make theoretical predictions about the frequency of different progenitor scenarios. Unfortunately, the show no consistent picture whether the single degenerate scenario produces enough type Ia supernova events to explain observed rates. Whereas Ruiter et al. (2009) find that the observed rate is at least an order of magnitude larger than the rate they predict for hydrogen accretion Chandrasekhar-mass explosions, Han & Podsiadlowski (2004) predict a rate that is nearly as large as the observed one. The difference is mainly attributed to a different treatment of mass transfer and mass loss, which are both theoretically not completely understood.

There are several observational constrains on this scenario. The hydrogen burning on the surface of the white dwarf emits the nuclear energy released in this process in X-rays. Therefore, these systems should be visible as super-soft X-ray sources (Kahabka & van den Heuvel, 1997). After the white dwarf reached the Chandrasekhar-mass and exploded, the X-ray source should be gone. Using pre-supernova X-ray observations, Voss & Nelemans (2008) claimed to have found an X-ray source close to the position of a type Ia supernovae, that vanished afterwards. Roelofs et al. (2008), however, showed that this was most likely a false identification, as the X-ray source was at a slightly different position than the supernova. Nonetheless, this method may eventually be able to confirm the hydrogen accretion progenitor scenario.

Also, without resolving individual objects, the expected X-ray luminosity from these systems can be used to constrain the viability of the scenario. Gilfanov & Bogdán (2010) analyzed the total X-ray flux of several nearby elliptical galaxies. They found, that it is not large enough to explain the observed type Ia supernova rate with hydrogen accreting Chandrasekhar-mass progenitor systems . Indeed, they conclude that these progenitors contribute at most a few percent to the total type Ia supernova rate in the galaxies they looked at.

Another observational constraint is the presence of hydrogen in the progenitor system. During the mass transfer, some hydrogen is expelled from the binary system. When the supernova ejecta hit this hydrogen-rich circumstellar material, it may affect the supernova spectra. However, as there are no hydrogen lines in type Ia supernova spectra, there has to be a small enough amount of hydrogen, that it is not visible directly. Patat et al. (2007) found some variability in the NaI lines in spectra of the type Ia supernova SN 2006X. They associated it with the presence of hydrogen in the circumstellar medium the ejecta run into. Another constraint originates from nebular spectra of type Ia supernovae. Modeling nebular spectra, Leonard (2007) was able to put an upper limit of only about $0.01 M_\odot$ on the amount of hydrogen that can be hidden in the ejecta without being seen in spectra. However, as the supernova ejecta hit the companion star, it is expected that some hydrogen-rich

material from the envelope of the star mixes into the ejecta (Marietta et al., 2000). Chapter 4 will discuss this constraint in detail.

After the explosion of the white dwarf, its companion is left behind and moves with its tangential velocity away from the center of the explosion. It gains some additional momentum as the supernova ejecta hit it, but this is small compared to the tangential velocity of the star (Marietta et al., 2000). For nearby remnants of historical type Ia supernovae, it is possible to look for the remaining companion star. Ruiz-Lapuente et al. (2004) claimed, that they identified the companion for Tycho's supernova (1572). They determined proper motion and radial velocity of all visible stars in the vicinity of the explosion and concluded that one of them, Tycho G, is consistent with having been at the center of the explosion some 400 years ago. Better data, however, showed that neither Tycho G, nor any other of the visible stars near the explosion can be associated with the supernova event (Kerzendorf et al., 2009).

Instead of hydrogen that is burned to helium on the surface, the white dwarf can accrete helium directly from helium stars (Woosley & Weaver, 1994). The existence of systems that contain a massive white dwarf accreting helium has recently been confirmed by observations (Kato & Hachisu, 2003). This way, the white dwarf can accrete until it reaches the Chandrasekhar-mass and explode. It would, however, be far less bright in X-rays, as the energy release from the burning of helium to carbon is only a small fraction of the energy release from the burning of hydrogen to helium. Therefore, this scenario could be reconcilable with the observations by Gilfanov & Bogdán (2010), but population synthesis calculations (Ruiter et al., 2009) indicate that these systems are not frequent enough to explain the observed type Ia supernova rate.

There is, however, the possibility, that a massive carbon/oxygen white dwarf with a helium envelope explodes, before it reaches the Chandrasekhar-mass. The basic idea is, that if helium is not burned steadily, it accumulates on the surface of the white dwarf. If this helium shell becomes massive enough, it may become dynamically unstable. A detonation of the helium shell could then lead to a detonation of the sub-Chandrasekhar carbon/oxygen core (Woosley & Weaver, 1986). Details of this scenario are discussed in Section 2.2.2. If this scenario works, it is expected produce much more frequent events than the Chandrasekhar-mass scenario, as the white dwarf has to accrete significantly less material before it can explode. Therefore, also systems with initially less massive white dwarfs may finally explode. This scenario may be a result of either accretion of helium, or accretion of hydrogen that is burned to helium on the surface of the white dwarf.

In the **double degenerate scenario**, both objects in the binary system are white dwarfs. Thus, intrinsically there is no hydrogen around in the system, except maybe some old circumstellar material that has been ejected when the white dwarfs formed. The mass transfer is not initiated by evolutionary effects, but the emission of gravitational waves as the two white dwarfs orbit each other takes away angular momentum from the system and shrinks the orbit. As the white dwarfs come closer and closer, eventually one of them fills its Roche-lobe and mass transfer sets in. Depending on the mass ratio of the white dwarfs, mass transfer may be stable or unstable. Whether it is stable or unstable is crucial for the

fate of the system.

If the companion star is a helium white dwarf, the system is similar to the helium accreting single degenerate scenario. As the maximum mass of a helium white dwarf is only about $0.45 M_\odot$ and typical helium white dwarfs are less massive, however, the amount of mass the primary white dwarf can accrete through mass transfer from the helium white dwarf is limited. Therefore, this scenario is mainly a candidate for the sub-Chandrasekhar explosion, rather than the Chandrasekhar-mass scenario. This idea is supported by a recent study (Guillochon et al., 2010) showing that if the accretion from a helium white dwarf onto a carbon/oxygen white dwarf becomes dynamically unstable, instabilities in the accretion stream may likely lead to a detonation of the helium layer at the surface of the white dwarf.

For two carbon/oxygen white dwarfs the situation is much more unclear. If the mass ratio is small, i.e. the mass difference between primary and secondary white dwarf is large, mass transfer is stable. The threshold for stable mass transfer is probably around a mass ratio of 2/3 (Paczyński, 1967), but its exact value is unknown, because dynamical effects play a role. If mass transfer is stable and the total mass of the system exceeds the Chandrasekhar-mass, the primary white dwarf may again explode as it approaches the Chandrasekhar-mass. In this case, the explosion scenario would be similar to the single degenerate Chandrasekhar-mass scenario.

If the mass ratio is larger than the threshold, mass transfer becomes unstable. This scenario has been studied numerically by several groups (see, e.g. Benz et al., 1990; Yoon et al., 2007; Motl et al., 2007; Lorén-Aguilar et al., 2009) with similar results. Soon after mass transfer sets in, the secondary white dwarf is disrupted by tidal forces. Its material forms a hot, thin envelope around the primary white dwarf and is accreted onto it at a very high rate. As shown by Saio & Nomoto (1998), the high accretion rate will ignite carbon at the surface of the remaining white dwarf and turn it into an oxygen/neon white dwarf. This oxygen/neon white dwarf again will collapse rather than lead to a thermonuclear explosion (Saio & Nomoto, 1985). Yoon et al. (2007) explored whether this fate may be avoided by a fine tuning of the accretion rate, but this scenario does not seem to be too likely.

There is, however, another way to avoid this fate. If, during the merger itself, conditions arise in the system that allow a detonation to form directly, a thermonuclear explosion will develop. To study this scenario, which has not been analyzed in detail yet, is one of the main objectives of this theses. It is discussed in Chapter 3. In such a model, the explosion comes with more mass than a Chandrasekhar-mass, leading to a super-Chandrasekhar explosion.

There are only very few observational constraints on the existence of massive binary systems of two white dwarfs. Until now, only one system has been found, which is expected to merge within a Hubble-time and has a total mass slightly larger than the Chandrasekhar-mass (Napiwotzki et al., 2004). This, however, is probably a result of observational limitations, rather than a proof of the non-existence of these systems. On the contrary, population synthesis calculations suggest, that of all proposed progenitor systems only double degenerate systems are frequent enough to explain the observed type Ia supernova rate (Ruiter

et al., 2009), assuming that all binary systems of two white dwarfs whose total mass exceeds the Chandrasekhar-mass and that merge within a Hubble-time do explode as a type Ia supernova.

If the merger of two white dwarfs does not lead to an explosion in the process of merging and does not cause the conversion of the primary white dwarf into an oxygen/neon white dwarf, it will accrete mass from the remains of the secondary white dwarf. Inherited from the binary system, the system of primary white dwarf plus hot envelope has a considerable angular momentum. If accretion will make the primary white dwarf rotating differentially, its mass may grow up to two solar mases, much larger than the Chandrasekhar-mass of non-rotating white dwarfs (Yoon & Langer, 2004). In principle, also accretion in the single degenerate scenario may produce differentially rotating, very massive white dwarfs, if angular momentum transfer is efficient. However, it is difficult to see how this should work given the constraints on the accretion rate that already restrict the single degenerate Chandrasekhar-mass scenario significantly (Yoon & Langer, 2005).

Regardless of the details of the progenitor system, any system that claims to explain at least a large fraction of all type Ia supernovae, has to account for several general observational constraints:

I) The progenitor system has to be frequent enough to explain the observed type Ia supernova **rate**. As indicated above, this is already a problem for most scenarios.

II) The progenitors have to reproduce the observed **delay time distribution** of type Ia supernovae. Here, single degenerate and double degenerate scenarios are inherently different. In the single degenerate scenario, the delay time is given by the evolutionary timescale of the companion star. Thus, it is connected to the mass of the companion. In the double degenerate scenario, in contrast, it is controlled by the timescale of the emission of gravitational waves, which depends on the total mass of the system and the initial separation of the binary.

III) A progenitor scenario, together with the explosion scenario, has to provide a large enough parameter space to explain the **variability** of normal type Ia supernovae (in particular a synthesized ^{56}Ni mass between 0.4 and 1.0$M_{\odot}$). At the same time, the variability has to be small enough to not destroy the observed general homogeneity of type Ia supernovae.

IV) The progenitor scenario has to explain the correlation between several observational properties (luminosity, delay time) of type Ia supernovae with the type their **host galaxies**.

A progenitor scenario that is not able to explain these points can not be the dominant source of type Ia supernovae. However, it may still be responsible for a small fraction of all

supernovae, in particular for some peculiar events.

2.2.2 Explosion scenarios

The explosion scenarios proposed for type Ia supernovae can be divided into three categories, according to the mass of the exploding star. Chandrasekhar-mass models where the mass of the exploding white dwarf is close to the Chandrasekhar-mass have been widely discussed in the past. In addition there are sub-Chandrasekhar and super-Chandrasekhar models in which less and more massive white dwarfs explode. These models have been disregarded in the past, but after recent observational and theoretical improvements, they attract interest again.

A fundamental difference between various explosion scenarios is the way the nuclear burning proceeds. Explosive burning allows for two different modes of flame propagation. A deflagration flame propagates subsonically, driven by thermal conduction. As it is slower than the speed of sound, information about the flame front travels ahead of the flame. Thus the white dwarf as a whole can react to the flame, in particular it is able to expand as a reaction to being heated in the center. A detonation flame propagates supersonically with respect to the speed of sound in the unburned material in front of the flame. It is driven by a hydrodynamic shock, that compresses material before it is burned. As no information about the flame can be communicated faster than the flame moves, the yet unburned parts of the white dwarf can not react to the flame and only "see" it when they are also burned. Thus the white dwarf does not expand prior to being burned.

In general, knowledge about the ignition, i.e. how the flame forms, is poor in all explosion scenarios. This is often due to stochastic processes dominating the ignition. Another problem is that the ignition itself is a microscopic process that occurs on length scales of the order of centimeters to meters. These scales, however, are still far from being resolved in full-star numerical simulations of white dwarfs, that are necessary to model the environment in which the flame is supposed to form.

Chandrasekhar-mass models

Chandrasekhar-mass white dwarfs are appealing as progenitors of type Ia supernovae, as the white dwarf naturally becomes unstable as it approaches the Chandrasekhar-mass limit. The idea is that while the mass of the white dwarf grows, its central density and temperature increase. When it approaches the Chandrasekhar-mass, it is highly degenerate at the center with a central density around 10^9g cm^{-3} and the central temperature becomes large enough to ignite carbon burning. With carbon burning a simmering phase starts, in which the energy released in the center of the white dwarf is mostly transported away by convection. Some energy, however, is used to slowly heat up the center further. This phase can last for several hundred years. As the nuclear burning rates involved are highly temperature sensitive, the energy release grows as the temperature increases. Therefore, at some point

the cooling mechanisms are not efficient enough any more to transport away the energy that is released. As the white dwarf is completely degenerate in the center, there the pressure does not depend on the temperature. Thus the white dwarf is not able to expand and cool, as the temperature rises in the center which leads to a thermonuclear runaway and the formation of a flame.

Despite attempts to model the simmering phase just before ignition, it is largely unclear what the initial flame configuration looks like (see, e.g. Almgren et al., 2006; Zingale et al., 2009). Initial flame geometries used for type Ia supernova modeling range from single off-center bubbles (Plewa et al., 2004; Röpke et al., 2007b) to isotropic ensembles of a large number of bubbles in the center (Röpke et al., 2007a) and a time-dependent, stochastic ignition process (Schmidt & Niemeyer, 2006).

A priori it is also not clear whether the flames that emerge from the simmering phase are deflagrations or detonations. Numerical simulations show, however, that detonated Chandrasekhar-mass white dwarfs produce only iron group elements and virtually no intermediate mass elements (Arnett, 1979; Khokhlov et al., 1993), as a result of the high densities at the center and the flat density profile of white dwarfs. This is in clear contradiction to spectra of type Ia supernovae that are defined by their strong silicon II line and show strong lines of other intermediate mass elements also. Thus, current Chandrasekhar-mass explosion models all assume that the simmering phase leads to the formation of a deflagration flame at or close to the center of the white dwarf.

Due to hydrodynamical instabilities and very large Reynolds numbers, the deflagration flame is highly turbulent. Compared to the laminar flame speed, this increases the propagation velocity of the flame by up to two orders of magnitude (Niemeyer & Hillebrandt, 1995; Niemeyer & Woosley, 1997). Once the flame is ignited at the center, it burns through the white dwarf which expands at the same time. When the density drops below some threshold, burning ceases. Thus, faster flame propagation leads to less expansion of the white dwarf and thus on average burning at higher densities. Also, the initial flame configuration changes the properties of the nuclear burning (Röpke et al., 2006b).

Pure deflagrations, however, seem unable to explain normal type Ia supernovae. Recent high resolution studies (Röpke et al., 2007a) with an initial flame configuration chosen to maximize the ^{56}Ni production show that a pure deflagration is able to release enough energy to unbind the star, but produces at most $\approx 0.4 M_\odot$ of ^{56}Ni. Also, the elements produced in the explosion are mixed to a large extend as a result of large-scale Rayleigh-Taylor instabilities. This contradicts observations, indicating that there is no unburned carbon in the central parts of type Ia supernova ejecta, and at the same time no iron group elements in the outer part of the ejecta. There are, however, several peculiar objects that may be explained with them (Jha et al., 2006; Phillips et al., 2007).

Since neither pure detonation nor pure deflagration Chandrasekhar-mass models can explain normal type Ia supernovae, it has been proposed that the nuclear burning starts out as deflagration and changes into a detonation later (Khokhlov, 1991). Three different ways

how the detonation may form have been proposed.

In the **delayed detonation** model, turbulent mixing of fuel and ash provides the conditions that lead to a detonation. As parts of the flame reach the outer parts of the white dwarf, it burns at lower densities and becomes broader. There, at some point the burning changes from the flamelet into the distributed burning regime (Niemeyer & Woosley, 1997). In this regime, homogeneous regions of mixed ash and fuel can emerge, that have a smooth temperature gradient. These regions then can give rise to detonations (Lisewski et al., 2000; Woosley, 2007; Woosley et al., 2009), but see (Niemeyer, 1999).

After the detonation has formed, it burns most of the remaining unburned material of the white dwarf in a short time. The main parameter that determines the outcome of the explosion is the strength of the deflagration (see, e.g. Khokhlov, 1991; Röpke & Niemeyer, 2007). A stronger deflagration burns more material, thus more energy is released and the white dwarf expands further. The nuclear synthesis products of the detonation depend basically only on the densities at which the fuel is burned. The higher the density, the further nuclear burning proceeds. Since densities are lower if the white dwarfs has expanded further, the detonation that forms later produces less iron group elements and more intermediate mass elements. Inversely, weaker deflagrations keep the white dwarf at higher densities until the detonation forms and therefore the explosion produces more iron group elements.

Kasen et al. (2009) showed, that an ensemble of these models with different initial flame configurations and different metallicities can reproduce the observed range of ^{56}Ni masses of normal type Ia supernovae. Synthetic observables calculated for these models reproduce the Phillips relation between brightness and lightcurve width reasonably well. At least some of these objects also show good agreement with observed type Ia supernova spectra. The main difficulty of the delayed detonation model is the formation of the detonation. It is still not understood in detail, and the models used to estimate the probability to form a detonation somewhere are highly parametrized. As the properties of the explosion depend crucially on the timing of the detonations (the earlier the detonation forms, the higher are the densities of the material it burns), the formation of the detonation has to be understood before this scenario can finally be judged.

The **gravitationally confined detonation** scenario assumes that the initial deflagration flame starts at a single point, slightly off-center. Due to buoyancy forces the bubble rises straight to the surface of the white dwarf. At the point where the bubble breaks through the surface, a shock wave develops that sweeps around the star and converges at the other side of the white dwarf. There, material is compressed and heated up, leading to conditions that may allow a detonation to form (Plewa et al., 2004; Meakin et al., 2009; Jordan et al., 2008). Three-dimensional simulations of the gravitationally confined detonation scenario show very bright supernovae. Since the scenario requires a very weak deflagration to achieve shock convergence, the detonation burns most of the star at high densities. Thus, the ejecta consist mostly of iron group elements which contain about one solar mass of ^{56}Ni, but only $\approx 0.1 M_\odot$ of intermediate mass elements are produced (Meakin et al., 2009). This is clearly not in agreement with normal type Ia supernovae, but may explain bright, 91T-like objects.

There are, however, no derived synthetic observables from these simulations yet, so it is not possible to judge whether they are really able to reproduce the optical display of any observed supernova events.

In addition, Röpke et al. (2007b) examined the gravitationally confined detonation using a different code with a different treatment of the deflagration. They conclude, that the conditions at the point on the surface where the shocks converge are not sufficient to form a detonation robustly. They argue, that previous simulations by Plewa et al. (2004) underestimate the energy release during the deflagration burning phase.

The **pulsating reverse detonation** scenario (e.g. Khokhlov, 1991; Bravo & García-Senz, 2006) finally assumes a deflagration that is weak enough not to unbind the white dwarf. After the deflagration flame has ceased, the star begins to pulsate. Material that is flowing back onto the core of the white dwarf may be compressed high enough to allow a detonation to form. The detonation then burns most of the white dwarf and causes the explosion. As Bravo & García-Senz (2006) showed, the pulsating reverse detonation scenario is able to explain the observed range of ^{56}Ni masses of normal type Ia supernovae, since it produces a range of ^{56}Ni masses between 0.4 and 0.9$M_\odot$. Synthetic spectra derived from these models, however, show carbon lines and iron group elements in the outer part of the ejecta, both in contradiction with normal type Ia supernovae.

None of the Chandrasekhar-mass models can explain 1991bg-like or superluminous type Ia supernovae, as the range of possible ^{56}Ni masses does not cover low and high enough values, respectively. Thus, even if Chandrasekhar-mass models are the correct explanation for normal type Ia supernovae, different explosion models have to be invoked to explain other subclasses.

Sub-Chandra models

The sub-Chandrasekhar explosion models start with a carbon/oxygen white dwarf that is significantly below the Chandrasekhar-mass and surrounded by a thin shell of helium. If, for some reason, a detonation forms somewhere in the helium shell, it sweeps around the star, burning the whole shell. The energy release during the nuclear burning sends shock waves into the carbon/oxygen core. If these shocks converge, they will create a very hot, very dense spot in which a detonation can form (Woosley & Weaver, 1995; Livne & Arnett, 1995). As shown by Fink et al. (2007), for geometrical reasons the shock convergence always leads to very high densities and temperatures, well beyond the conditions that are needed to form a detonation. A recent study by Fink et al. (2010) concluded, that even for small helium shells that contain only little mass (below 0.1$M_\odot$) detonations can form.

One advantage of these models is that they are supposed to be frequent enough to explain the observed type Ia supernova rate. Moreover, they are able to explain the observed range of ^{56}Ni masses in a natural way, because more massive carbon/oxygen cores contain more material at higher densities, where nuclear burning proceeds further.

Synthetic observables of sub-Chandra explosions, however, are not in very good agreement with observations (Kromer et al., 2010). The main problem is caused by iron group elements in the ashes of the helium shell. These iron group elements in the outermost parts of the ejecta redistribute too much flux from blue to red wavelengths. Sim et al. (2010) showed that toy models which contain only a carbon/oxygen core and are detonated artificially at the center do not show these problems, but are in good agreement with observed spectra and lightcurves of type Ia supernovae. This indicates, that the validity of the sub-Chandra scenario will depend on whether the effects of the helium shell on observables can be hidden somehow.

Super-Chandra models

Today, there are several type Ia supernovae whose ejecta have been claimed to contain more mass than a Chandrasekhar-mass (see section 2.2.1). If these claims are correct, the explosion of a super-Chandrasekhar object is required to explain these events. One possibility for super-Chandra explosions is a double degenerate merger exploding during the merging process. This scenario is the main topic of this thesis and discussed in detail in chapter 3.

Another super-Chandra scenario involves differentially rotating white dwarfs. These can have masses up to two solar masses (Yoon & Langer, 2005). Similar to Chandrasekhar-mass white dwarfs, these objects may also start to burn close to the center at some point. Pfannes et al. (2010a) and Pfannes et al. (2010b) studied pure deflagrations and pure detonations of such massive white dwarfs. They find that these objects lead to very bright explosions, bright enough for superluminous type Ia supernovae. However, they release large amounts of nuclear energy. Thus the ejecta velocities are by far too fast compared with observations. In addition, their ejecta are aspherical, which is only observed for very faint, 1991bg-like objects.

3 The Dynamic Merger Scenario

3.1 The Scenario

The dynamic merger scenario provides, for the first time, a robust path from a carbon/oxygen-white dwarf binary to a type Ia supernova. In this scenario, a violent merging event directly causes a detonation.

Once a binary system of two white dwarfs has formed, gravitational wave emission leads to continuus shrinking of its orbit. At some point, the two the white dwarfs are close enough to interact directly. If the mass ratio of the two white dwarfs is close to unity, the interaction becomes very violent and the less massive, and therefore less compact white dwarf is destroyed. Its material crashes onto the remaining white dwarf, is compressed and heated up. At the interface it can become hot enough to ignite carbon. As carbon burning starts, the material is heated up further. If these hotspots occur at high enough densities, they can reach conditions sufficient to ignite a detonation.

The detonation then propagates through the system and burns most of the original material to heavier nuclei. As the detonation flame moves supersonically with respect to the fuel and the timescale of the flame to cross the whole star are much lower than dynamical timescales involved, the system is effectively frozen in and burned nearly instantaneously at the moment the detonation is ignited. With enough energy released from nuclear burning to overcome its gravitational binding energy, the material becomes unbound, explodes, and finally reaches a state of homologous expansion.

3.2 Modeling pipeline

The entire evolution of a double white dwarf binary system to the visible appearance of a type Ia supernova covers a broad range of different areas of physics, including hydrodynamics, nuclear physics and radiative transfer. As these effects cannot be modeled in one

single approach, the evolution is split into five consecutive phases each being dominated by different physical processes.

These phases are:

A) **The stable binary system**
All our simulations start from a binary system of two CO white dwarfs. However, as described in 2.2.1, we do not know any binary systems of two CO white dwarfs with a total mass significantly larger than the Chandrasekhar-mass and only one system which exceeds the Chandrasekhar-mass (Napiwotzki et al., 2004). Therefore we have to rely on population synthesis models to determine which binaries exist at all and how frequent they are. In addition, we can use population synthesis to constrain delay times of specific progenitor systems and explore correlations between their frequency and host galaxy environment. We can then use this information to constrain the progenitor systems of specific Type Ia supernova subclasses by comparing them statistically with samples of observed Type Ia supernovae.

When the binary system forms, the separation is too large to cause any direct interaction. Both white dwarfs are in hydrostatic equilibrium. As time evolves, the orbit shrinks due to gravitational wave emission until they get close enough for mass transfer to set in. As the less massive white dwarf has a larger radius, mass transfer always takes place from the less massive to the more massive white dwarf. As discussed in Section 2.2.1 the stability of the mass transfer depends mainly on the mass ratio of the two white dwarfs. The dynamic merger scenario requires a large mass ratio. In this case the mass transfer is always unstable.

We do not follow the gradual shrinking of the orbit due to gravitational waves, as this proceeds on timescales of several 100Myrs to Gyrs. Instead, we start our simulations when the orbit becomes just close enough for mass transfer to start. This is possible because before all important parameters of the binary system save its orbital frequency are conserved.

B) **Inspiral and Merger**
The actual merger between the two white dwarfs happens on a timescales of a few tens of seconds. To model it we use a modified version of the Smoothed Particle Hydrodynamics (SPH) code GADGET (Springel, 2005) (for details on the code and the modifications made see Section 5.1). As SPH is a purely Lagrangian method, it is well suited for intrinsically three-dimensional problems with separated objects such as the merger of two white dwarfs.

The initial setup of the simulation consists of two white dwarfs in hydrostatic equilibrium on a circular orbit. The orbital period is chosen so that the binary is stable for at least one full orbit before it becomes unstable. The white dwarfs are realized from radial profiles of density, pressure and internal energy that are computed by integrating the equations of hydrostatic equilibrium starting from a central density assuming constant temperature and composition. For the contributions to the equation of state (EOS) from the electron gas, positrons and radiation, we use tables derived from the

Timmes EOS (Timmes & Arnett, 1999). The ions are treated as a fully ionized ideal gas. The detailed procedure to create a particle distribution in hydrostatic equilibrium resembling these one-dimensional profiles is explained in Section 5.1.6.

The merger is dominated by dynamic interactions of the two white dwarfs. The region where they come into contact with each other is strongly heated up. There the temperatures can become high enough to ignite nuclear fusion reactions of carbon. Therefore the change in composition and the additional energy release due to nuclear reactions have to be taken into account. To this end a nuclear reaction network that incorporates all α-elements up to ^{56}Ni is used. The implementation of this network and its coupling to hydrodynamics is described in Section 5.1.

If temperature and density at the contact interface become high enough, a detonation is assumed to form that causes the explosion of the merged object.

C) **Thermonuclear explosion**
When the detonation has formed, it is important to model its propagation and energy production from thermonuclear burning correctly. To this end we use a grid-based hydrodynamics code, as it is superior compared to SPH codes for following the propagation of shock waves. In our code, the equations of hydrodynamics are solved according to the Piecewise Parabolic Method (Colella & Woodward, 1984) on a uniform Cartesian grid, while the burning front is modeled with the level-set technique (Osher & Sethian, 1988). For details of the implementation see Section 5.2. The same EOS as for the SPH part is adopted.

The material that is crossed by the flame is burned promptly as described in Section 5.2. The corresponding difference in binding energies of fuel and ash is released behind the flame front. The code uses 5 species (He, C, O and one representative each of the intermediate mass and iron group elements), sufficient to model the energy release of the burning adequately.

The mapping of the state of the SPH simulation at the moment the detonation forms onto the Cartesian grid is described in Section 5.3.2. The detonation is then ignited in the simulation at the cell with the highest temperature.

The detonation needs about one to two seconds to burn the merged object (depending on its size). The energy release from nuclear burning is sufficient to overcome the gravitational binding energy of the merged object and to disrupt it. After that, the hot, unbound material expands and cools down. In order to keep the ejecta inside the computational domain while following them to homologous expansion, a moving-grid technique is employed (Röpke, 2005). After about 100 seconds, the ejecta have finally reached homologous expansion.

D) **Nucleosynthesis**
To obtain synthetic lightcurves and spectra from detailed radiative transfer we need to know the abundances and spatial distribution of all relevant isotopes. As it is far too expensive to couple a large nuclear network directly with the hydrodynamics, we compute the detailed nucleosynthesis in a separate ”post-processing“ step (Travaglio et al., 2004). For this purpose we place about 10^5 Lagrangian tracer particles of equal

mass in the simulation domain representing the mass distribution on the grid. The method to distribute the particles is described in Section 5.3.1.

The tracer particles are advected passively with the flow and record their thermodynamical trajectories. The trajectories and the initial composition of the white dwarfs (carbon/oxygen-ratio and electron fraction) are input to a reaction network calculation which involves a large nuclear network of 384 nuclei (Travaglio et al., 2004). From this, the detailed composition of the final ejecta is obtained.

E) **Radiative Transfer**
To compare our models quantitatively with observations, we use radiative transfer simulations to calculate synthetic observables. Density and composition structure from explosion and detailed nucleosynthesis are input to the radiative transfer simulations. Using the three-dimensional Monte Carlo radiative transfer code ARTIS, synthetic lightcurves and spectra are obtained. The physics of this code and the implementation are beyond the scope of this work, but extensively discussed in Kromer & Sim (2009).

This work concentrates on the modeling from merger to nucleosynthesis (steps B, C, D). Results of subsequent radiative transfer simulations (step E) performed by M. Kromer are used to compare the models with observations. For some models also results from population synthesis calculations (step A) by A. Ruiter are shown.

3.3 Model parameters

A binary system of two white dwarfs is uniquely defined by the *mass* and *composition* of each white dwarf and their *orbital separation*.

Most important to determine the fate of the system are the masses of the two white dwarfs. As described before, it has long been known that the mass ratio, defined as ratio between the mass of the secondary, less massive white dwarf to the mass of the primary, more massive white dwarf, $q = \frac{M_{secondary}}{M_{primary}}$, determines whether mass transfer between the two stars is stable. The Dynamic Merger Scenario requires violently unstable mass transfer, therefore the mass ratio has to be close to one.

The appearance of the supernova explosion is caused by the composition that are results from the nuclear burning in the explosion. The results of the nucleosynthesis themselves strongly depend on the density at which nuclear burning takes place. Therefore changing the mass of the white dwarfs leads to different density profiles and can significantly change the nucleosynthesis. Also explosions of systems with the same total mass but a different mass ratio and therefore different density profiles will look differently.

The initial composition mainly affects the nucleosynthesis, but may also influence the formation of a detonation in the first place.

The initial orbital separation for the modeling presented in this work is determined by requiring that the binary system is just about to become dynamically unstable and mass transfer sets in.

Table 3.1 gives an overview of the different models that are explored in this work. These models span a large range of ^{56}Ni-masses from very dim to very luminous events. They also cover models with similar primary white dwarf masses, but different mass ratios. As the code used is improved continuously, different methods for the setup of the SPH simulation, the relaxation of the objects in the SPH code and the determination of the pre-shock densities have been applied. The methods and their differences are discussed in Section 5. Table 3.1 shows which methods have been used for the individual models.

In the following section, first the merger of two $0.89 M_\odot$ white dwarfs is presented. This model is used as a showcase to discuss the different steps of the modeling in detail. After that a wide range of less and more massive mergers is covered.

Masses	Chapter	SPH Mass Resolution	Initial Period	Detonated at t	T	ρ	E_{nuc}	E_{kin}	$M_{^{56}Ni}$	M_{IME}	M_O	M_C	Methods Setup	Relax	Det.
$[M_\odot]$		$[M_\odot]$	[s]	[s]	$[10^9 K]$	$[10^6 g\,cm^{-3}]$	$[10^{51} erg]$	$[10^{51} erg]$	$[M_\odot]$	$[M_\odot]$	$[M_\odot]$	$[M_\odot]$			
0.89 + 0.89	3.4	$8.9 \cdot 10^{-7}$	28	66	2.9	3.8	1.6	1.3	0.1	1.1	0.5	< 0.1	A	A	A
0.89 + 0.90	3.4.3	$9.0 \cdot 10^{-7}$	25							B	B				
0.89 + 0.90	3.4.3	$1.8 \cdot 10^{-7}$	25							B	B				
0.81 + 0.90	3.4.7	$9.0 \cdot 10^{-7}$	33							B	B				
0.70 + 0.90	3.4.7	$9.0 \cdot 10^{-7}$	40							B	B				
0.8 + 0.8	3.5	$8.0 \cdot 10^{-7}$	33	49	2.6	1.8	1.3	1.1	$< 10^{-2}$	0.9	0.6	< 0.1	A	A	A
1.0 + 1.0	3.6	$1.0 \cdot 10^{-6}$	21	42	3.7	5.3	2.2	1.7	0.4	1.2	0.4	< 0.1	A	A	B
1.1 + 1.1	3.6	$1.1 \cdot 10^{-6}$	16	40	3.9	6.5	2.8	2.3	0.7	1.3	0.1	< 0.1	A	A	B
1.0 + 1.2	3.7	$1.2 \cdot 10^{-6}$	21	47	3.0	3.8	2.7	2.1	1.0	0.7	0.5	< 0.1	B	B	B

Table 3.1: Merger models discussed in this thesis. Shown are the masses of both white dwarfs, the mass resolution of the SPH particles and the initial orbital period of the binary system, followed by time from the start of the simulation, local temperature and density of the hottest particle when detonation conditions are reached. If in addition the explosion is modeled, the table presents the total nuclear energy E_{nuc} that is released in the burning, the final asymptotic kinetic energy E_{kin} of the ejecta and the amount of ^{56}Ni synthesized in the explosion. The last three columns distinguish different numerical approaches used for the simulations. The different modes are the method used to define the initial particle distribution of the white dwarfs (A: cube method, B: Healpix method), the relaxation method (A: passive, B: active) and the way to determine the pre-shock flame density of the detonation (A: static, B: dynamic). Details of these approaches are explained in Section 5.

3.4 The merger of two $0.89M_\odot$ white dwarfs

3.4.1 Setup

In a first step, a one-dimensional model of a carbon/oxygen white dwarf in hydrostatic equilibrium is constructed. This is done by integrating over the mass profile of a white dwarf, starting at the center with a given central density and assuming a constant temperature and nuclear composition throughout the whole star. Here, a central density of $\rho_C = 1.4{\cdot}10^7 \mathrm{g\ cm^{-3}}$, a temperature of $T = 5{\cdot}10^5 \mathrm{K}$ and a uniform composition of $X_C = X_O = 0.5$ is used, which yields a white dwarf with a total mass of $M = 0.89M_\odot$.

In a second step, this one-dimensional model is mapped on a distribution of SPH particles resembling the one-dimensional profile. The mapping is carried out by radial deformation of a uniform grid of particles in order to avoid Poisson noise as described in 5.1.6 . After the mapping, the white dwarf contains 10^6 particles with a particle mass of $8.9 \cdot 10^{-6} M_\odot$ each. Using GADGET the white dwarf is then passively relaxed for 100s to get rid of spurious numerical noise introduced by the setup.

The following basic code setup was used in all simulations:

- The number of neighbors is chosen to be 50.
- The gravitational softening length equals the smoothing length.
- All particles are given the same mass.
- A nuclear reaction network containing all 13 α-elements up to ^{56}Ni is used.

After relaxation, the white dwarf is duplicated and both stars are set onto a circular orbit around their combined center of mass with an orbital period of 28s, where all particles of one star are given the same initial velocity. This period was chosen to provide a marginally stable orbit, meaning that the system is stable for more than one complete orbit before tidal interactions lead to deformations and mass transfer between the white dwarfs. It is important to note, that the setup of the binary system is not perfectly symmetric to the center of mass of the system, as the second white dwarf is identical to the first one, but moved along the x-axis with no rotation. This explains why the binary system does not evolve symmetrically at later times.

3.4.2 Inspiral and merger

The density and temperature evolution of the white dwarf binary is shown in Fig 3.1 and Fig 3.2. They show the density and temperature on slices in the orbital plane and through the center of the z–axis for several snapshots. The binary is rotating clockwise.

The binary system is stable for nearly two orbits, but both stars are slightly distorted by tidal forces. After 50s the system clearly shows asymmetries. This is a direct consequence of the marginal asymmetries in the setup, it does not occur for perfectly symmetric initial conditions. However, in nature a perfectly symmetric system does not exist and thus the broken symmetry is the more realistic initial setup. The asymmetry leads to the complete disruption of one of the white dwarfs (from now on called “secondary”), whose material

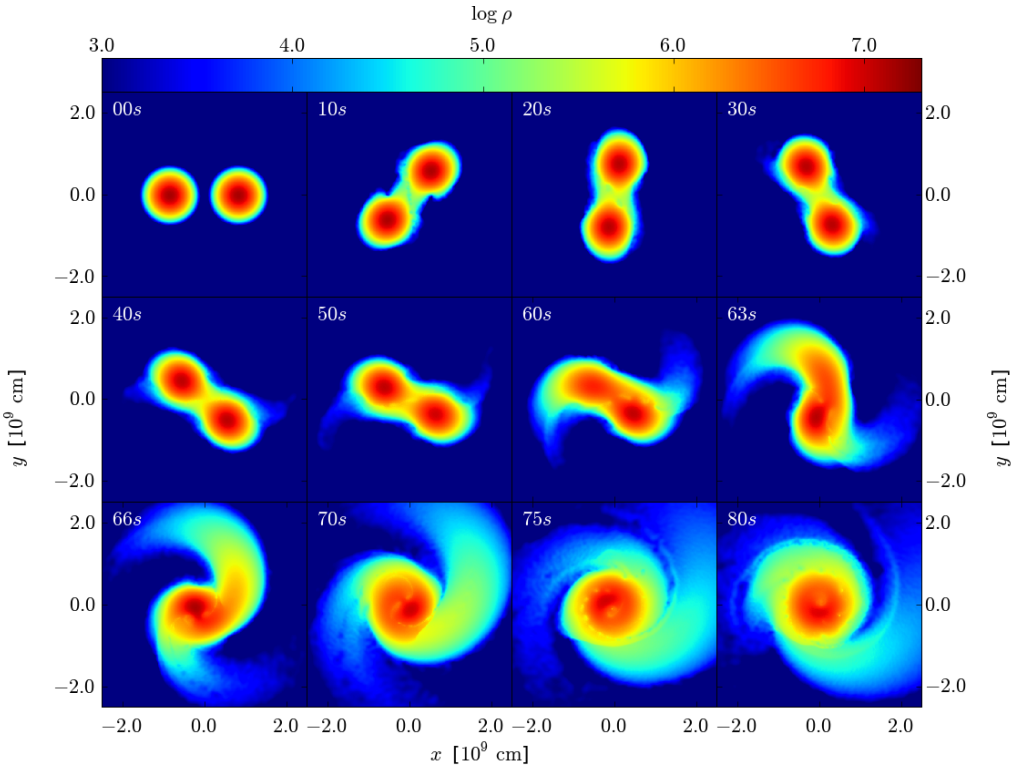

Figure 3.1: Density evolution of the merger of two 0.89$M_\odot$ white dwarfs. Color-coded is the logarithm of the density.

is violently merged with the remaining core of the other white dwarf (from now on called "primary"). In this phase some of the material of the secondary is heated up significantly first by compression and later also by nuclear reactions. We follow the evolution of the binary system for 85s, stopping more than 15s after the maximum of the temperature occurred. The maximum temperatures reached are well above 10^9K.

The evolution of the binary is qualitatively similar to previous studies of merging double degenerate systems (e.g., Guerrero et al., 2004; Yoon et al., 2007; Lorén-Aguilar et al., 2009). These studies also found, that the less massive white dwarf is disrupted during the merger and its material builds up a hot, thin envelope around the remaining white dwarf. Lorén-Aguilar et al. (2009) also find, that when material of the secondary first hits the primary, the temperature at the interface becomes high enough to start carbon fusion. In their simulations, this leads to an rapid increase of the temperature there due to nuclear energy release. As the temperature increases, the material becomes non-degenerate, expands and cools down, thereby quenching the nuclear reactions. In the end, only a very small amount of material is burned. This is equivalent to what we observe in our simulations.

There is, however, an important difference in the interpretation. Lorén-Aguilar et al. (2009) do not discuss the possibility of a detonation forming at the hot-spot. In case a detonation forms there, it will be able to burn the whole white dwarf. This is a direct consequence of the fact that the detonation propagates supersonically and therefore burns all the

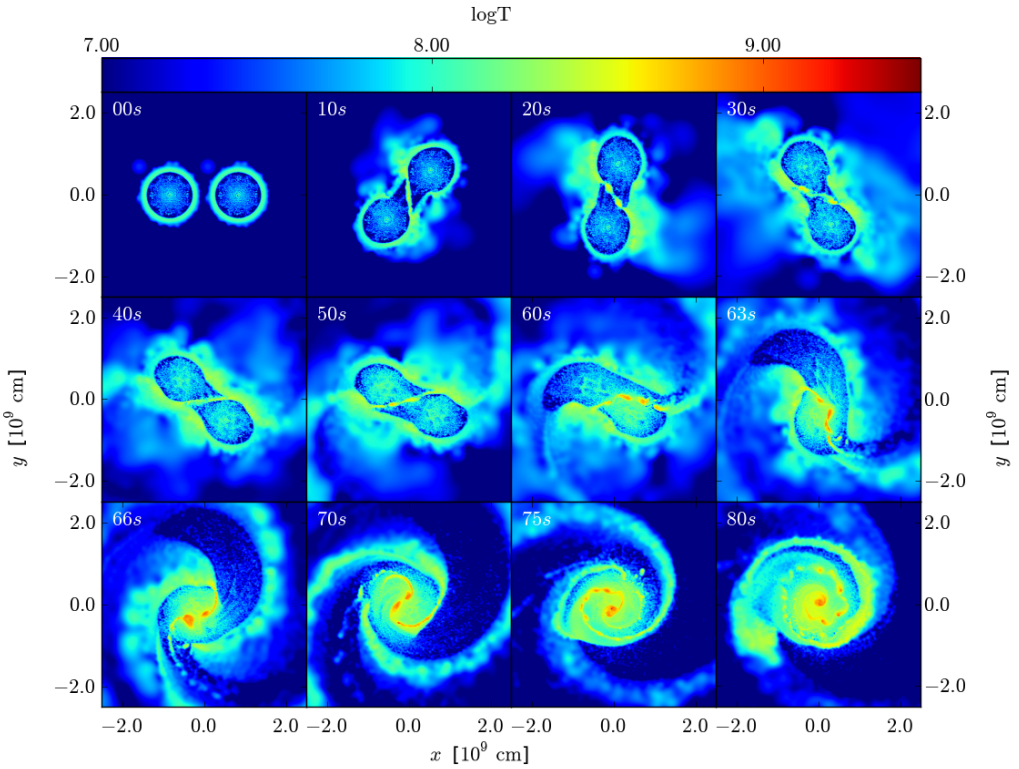

Figure 3.2: Temperature evolution of the merger of two $0.89M_{\odot}$ white dwarfs. Color-coded is the logarithm of the temperature.

material before it can expand.

Hence, the crucial question that decides if the dynamic merger scenario works is whether the merging process leads to the formation of a detonation. In the next section, we discuss this question in detail.

3.4.3 Formation of the detonation

The conditions and the process leading to the formation of a detonation are still a topic of active research (e.g., Seitenzahl et al., 2009; Röpke et al., 2007b). There are basically two ways a detonation can form.

Detonation ignition mechanisms

First, a strong enough shock may lead to *direct formation* of a detonation. In this case, an already existing shock wave compresses and heats the material causing nuclear burning behind the shock. If the nuclear energy release behind the shock becomes large enough, it may be sufficient to create a self-sustained detonation (e.g., Body, 1997). As the merger is very violent, we naturally expect strong shocks to occur in the interaction region. Unfortunately, however, we are far from being able to resolve these shocks on scales small enough to observe the formation of a detonation. As all SPH particles in our simulation have the same

mass, the mass resolution is constant. Therefore regions with higher density are resolved better than regions with low density. Given that the interaction between the two white dwarfs occurs at comparatively low densities, their spatial resolution is intrinsically worse. In fact, we only barely resolve shocks in the interaction region at all. Therefore we are not able to judge from our current simulations whether a detonation can form directly from a shock. As typical detonation flames are of the order of a few meters and the best resolved regions in our simulations are of the order of 10^5m, only future simulations with very high adaptivity may be able to resolve them in global simulations.

Second, it may be possible to form a detonation spontaneously without a preceding shock. In this case, as first proposed by Zel'dovich et al. (1970), nuclear burning in a preconditioned region (i.e. with a spatial density, temperature or composition gradient) creates a spontaneous ignition wave. If the preconditioning is favorable, and this ignition wave may have a supersonic phase velocity, it forms a shock wave that is followed by nuclear burning. If the release of nuclear energy behind the shock wave is sufficient to sustain the shock after it reaches the bottom of the gradient, it becomes a self-sustained detonation.

Again, we are not able able to resolve this mechanism in our simulations. Therefore we have to rely on studies that model this mechanism for different conditions to get an indication whether we should expect a detonation to form. To this end, we use the recent study by Seitenzahl et al. (2009). They carried out one-dimensional simulations of the gradient mechanism for different initial conditions (varying i.e. temperature, density and steepness of the gradient) where they resolved the shock. They show, that for the most favorable conditions of geometry and gradient the density threshold to form a detonation in carbon/oxygen material is 10^6g cm^{-3}. At this density, a temperature larger then $2.8 \cdot 10^9$K is required over a range of some meters. For higher densities, the temperatures required drop. These values, however, carry large uncertainties, therefore they can only provide a hint to whether a detonation forms or not. In the following, we impose that given a hot-spot with a density larger than $2 \cdot 10^6$g cm^{-3} and a temperature larger then $2.5 \cdot 10^9$K exists, it is reasonable to assume that a detonation may form.

Conditions

Figure 3.3 shows density versus temperature of all particles for several snapshots from 60 s to 70 s after the start of the simulation in a scatter plot. This is the timerange when the material of the secondary white dwarf has just hit the primary and a hot-spot at the interface emerges. Afterwards, the temperature drops again as the hot material expands. Temperatures larger than $2 \cdot 10^9$K are reached, but only for a small number of particles. These particles are special as they ignited carbon and already burned a small amount of carbon into intermediate mass elements (in this case Mg / Si). They fulfill the criterion we require to form a detonation.

However, the overall number of these particles is quite small, so their exact properties have to be taken with caution. Therefore we have to check whether they show a barely resolved physical effect or are just a numerical artifact. This can be tested by redoing the simulation with significantly higher resolution.

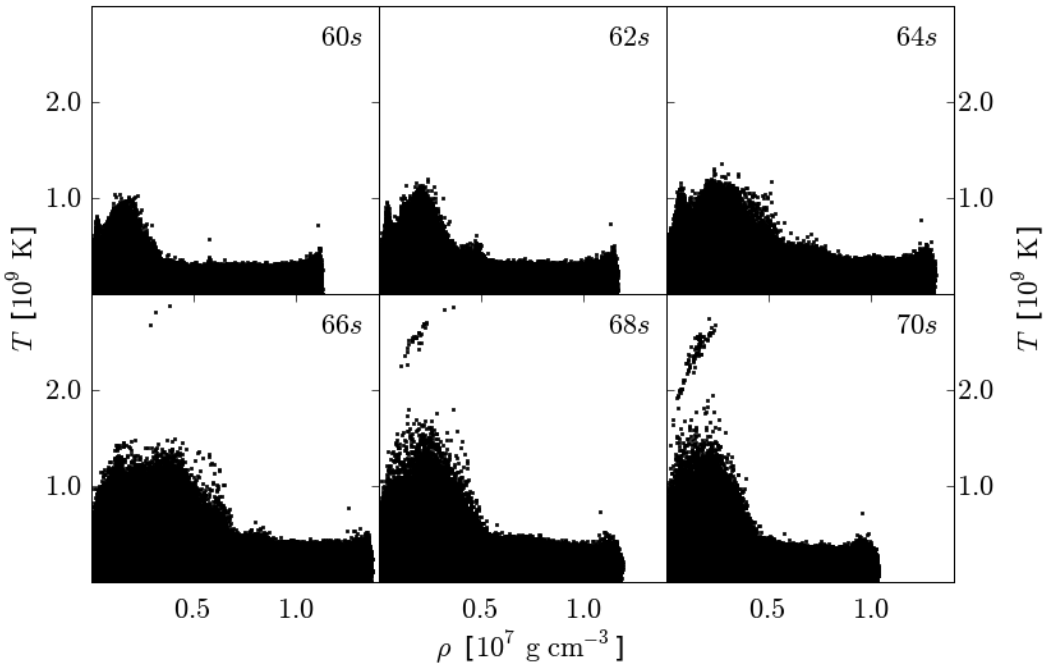

Figure 3.3: Density vs. temperature scatter plot for all particles of the merger of two $0.89M_\odot$ white dwarfs.

Resolution study

For the resolution study, we alter the initial conditions slightly and start with a binary system of two white dwarfs of $0.90M_\odot$ and $0.89M_\odot$, respectively. The main advantage of this model is that always the less massive white dwarf is disrupted, whereas for a merger of two white dwarfs with exactly the same mass it depends on numerical noise which of them is destroyed.

Figure 3.4 shows the density of two simulations of such a merger with $2 \cdot 10^6$ and 10^7 particles respectively. It shows excellent agreement between both simulations in the density structure . Over-plotted are the positions of all particles with a temperature larger than $2 \cdot 10^9$K. In both simulations the particles form at the same locations. The number of these particles, however, increases from 11 to 127 from the lower resolved to the higher resolved simulation. As the number of particles is only increased by a factor of five, the total mass at temperatures larger than $2 \cdot 10^9$K is approximately twice as large in the high resolution simulation. Therefore we can conclude, that these hot particles are real, rather than a numerical artifact. The high resolution simulation also indicates, that we underestimate the conditions in these hot-spots due to a lack of resolution.

Additional unresolved effects on the detonation conditions

There are two additional effects that may influence the formation of a detonation, but are basically ignored in our simulations.

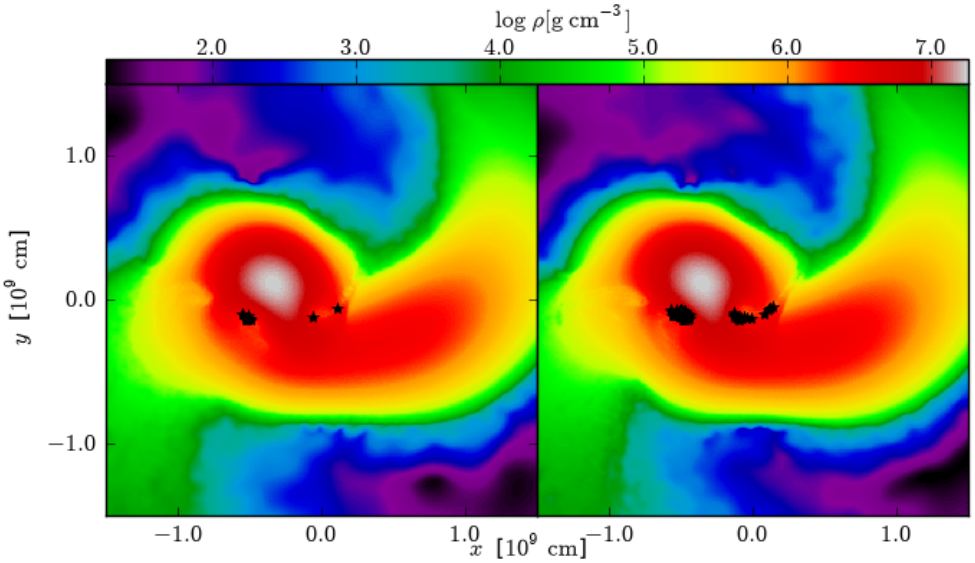

Figure 3.4: Resolution test of the detonation conditions of the merger of two white dwarfs of $0.90M_\odot$ and $0.89M_\odot$ with an initial period of 25s. The left panels shows a simulation with $2 \cdot 10^6$ particles, the simulation shown in the right panel contains 10^7 particles. Both panels show a density slice after the system has evolved for 32s. The black stars mark all particles with a temperature larger than $2 \cdot 10^9$K.

As discussed above, we do not resolve shocks at the interface very well. This effect can only be overcome by choosing a scheme that allows for refinement according to arbitrary criteria.

Second, according to stellar evolution calculations there is a small helium shell on top of a carbon/oxygen white dwarf. For a white dwarf around $0.9M_\odot$ this shell is expected to contain of the order of $10^{-3}M_\odot$ of helium (A. Serenelli, personal communication). It is also known from latest studies by Seitenzahl et al. (2009) that already a small mass fraction of helium mixed into carbon fuel significantly lowers the density that is required for the formation of a detonation. As the helium layer is located exactly in the region where the merger is most violent and the hot-spots form, it may be an important ingredient that lowers the density necessary to ignite a detonation.

In summary, the conditions we apply to decide whether or not a detonation forms are conservative.

3.4.4 Explosion

Assuming that the conditions are sufficient to form a detonation, we map the state of the simulation after 66s, when the first hot particles appear, onto a uniform Cartesian grid. The mapping procedure is described in detail in Section 5.3.2. We then use the MPA Type Ia supernova code as described in Section 5.2 to model the propagation of the detonation and the subsequent nuclear burning. We ignite the detonation in the cell with the highest temperature.

Figure 3.5 shows the density evolution after the merger. The detonation takes about two

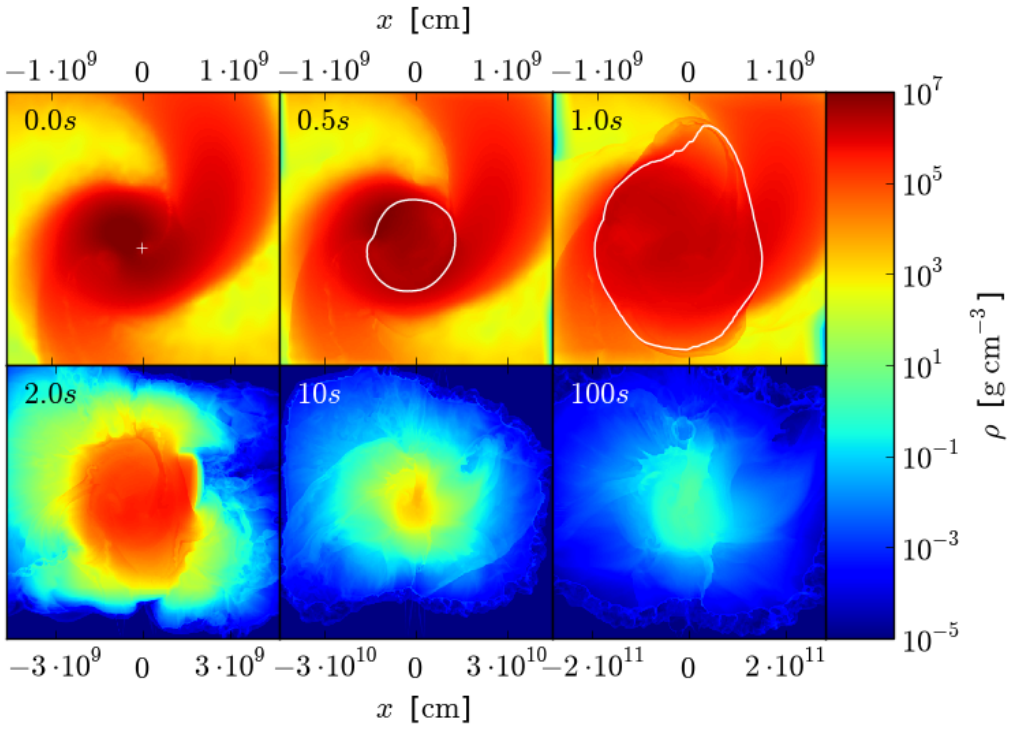

Figure 3.5: Density evolution of the thermonuclear explosion of a merger of two $0.89 M_\odot$ white dwarfs. Color-coded is the logarithm of the density. The white cross in the upper left panel shows the point where the detonation is ignited. The white contours show the position of the detonation front.

seconds to cross the whole object and burn its material. This is significantly faster then the timescale on which the hydrodynamical properties of the object change. Thus, the merged object is burned instantaneously as it is the moment the detonation forms. As the density is basically kept fixed while the burning proceeds, it is possible to obtain a simple estimate for the total amount of iron group elements that will be synthesized during the nuclear burning from the total mass that is above a density of $10^7 \mathrm{g\ cm^{-3}}$. The energy released from nuclear burning is sufficient to unbind the object. Subsequently the hot ejecta expand and cool down until they have reached homologous expansion after 100 s. The ejecta then have an asymptotic kinetic energy of $1.3 \cdot 10^{51}$erg, similar to the kinetic energy of the W7 Chandrasekhar mass explosion model of Nomoto et al. (1984) that is widely regarded as a good model for standard type Ia supernovae. The total mass of the ejecta, however, is $1.72 M_\odot$ or 1.2 Chandrasekhar masses and therefore significantly larger compared to the W7 model. Thus the average velocity of the ejecta is smaller. The final composition of the ejecta consists of $0.03 M_\odot$ of carbon, $0.54 M_\odot$ of oxygen, $1.05 M_\odot$ of intermediate mass elements and $0.1 M_\odot$ of iron group elements (in this case basically only ^{56}Ni). Therefore, despite being Super-Chandrasekhar, this explosion is subluminous rather than superluminous as proposed by Hicken et al. (2007) for SN 2006gz. The distribution of the mass of the ejecta

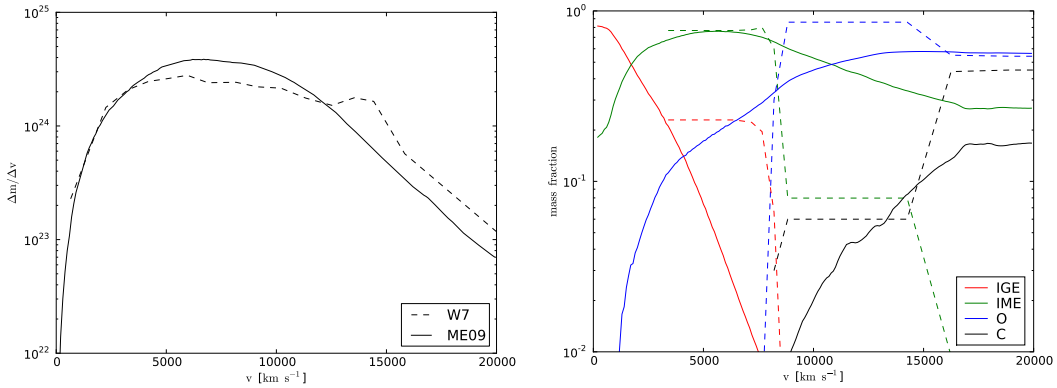

(a) Mass distribution in velocity space compared to the W7 model.

(b) Composition in velocity space compared to an abundance tomography study of the subluminous SN 2005bl by Hachinger et al. (2009). The solid lines show our model, the dashed lines the composition inferred for SN 2005bl.

Figure 3.6: Mass and abundance distribution in velocity space.

in velocity space is compared to the W7 model in the left panel of Figure 3.6. As expected, the additional mass is at low velocities between 5000km s^{-1} and 10000km s^{-1}. At higher velocities it contains less mass than the W7 model.

With a ^{56}Ni mass of only $0.1 M_\odot$ this merger is similar to the most subluminous type Ia supernovae observed today. We argue, that it falls into the class of 1991bg-like supernovae described in Taubenberger et al. (2008). For one object of this class, SN 2005bl, a detailed study including abundance tomography was done by Hachinger et al. (2009). In this study the authors find, that there has to be significantly less mass at higher velocities compared to a W7 mass profile to be able to model observed spectra. This is in agreement with our simulation. The right panel of Figure 3.6 shows a comparison between our final abundance pattern and the results of the abundance tomography for SN 2005bl. Despite differences in details, main features are well reproduced. There are basically three different layers. The outermost layer is dominated by oxygen, with contributions of unburned carbon and some amount of intermediate mass elements. Below velocities of about 12, 000km s^{-1} intermediate mass elements dominate down to very low velocities. Carbon is found down to velocities of $\approx$ 10, 000km s^{-1}. Iron group elements are found up to velocities of $\approx$ 10, 000km s^{-1}, but dominate only in the very innermost part of the ejecta. Note that the abundances in this plot are angle averaged. The composition is for incomplete Silicon-burning. As the densities are not high enough to reach nuclear statistical equilibrium, only a small fraction of the material is burned to iron group elements and most of it to intermediate mass elements. Thus, the ejecta are dominated by intermediate mass elements with a small contribution of iron group elements.

As neither the binary system in the beginning nor the merged object at the onset of the detonation are close to spherical, we expect a significant asphericity also in the structure of

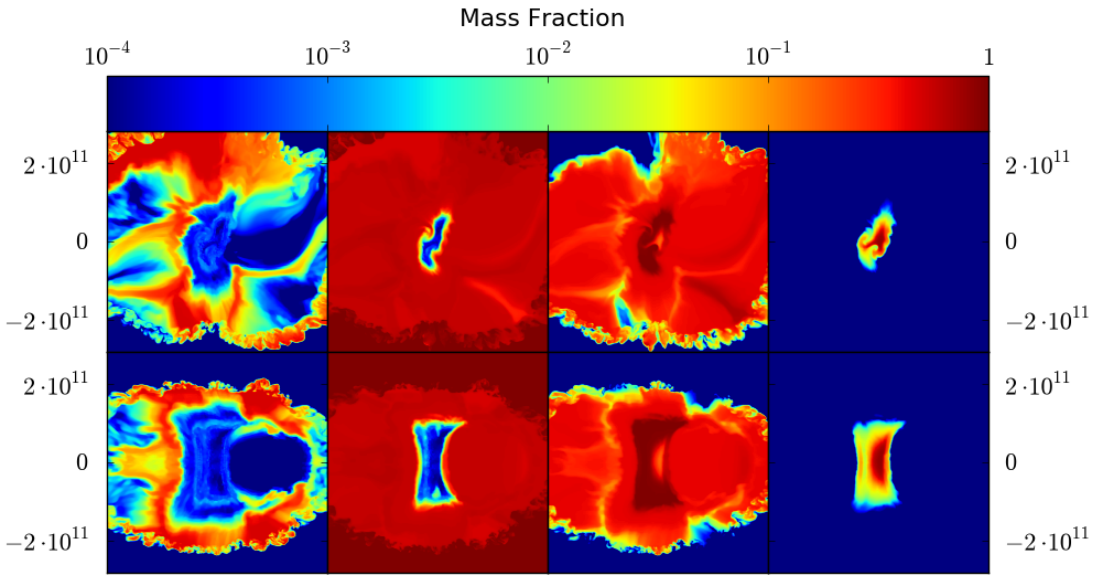

Figure 3.7: Final composition of the ejecta in homologous expansion 100s after the explosion. The panels show from the left to the right the abundances of carbon, oxygen, intermediate mass elements and iron group elements. The upper and lower panels show the system viewed face-on and edge-on, respectively.

the ejecta. Figure 3.7 shows the final abundance distribution in slices in the plane of rotation and perpendicular to it as inferred from our hydrodynamical simulation. It shows significant asphericities for all species with an axis ratio of $\approx 2:1$. This fits with spectropolarimetry observations of SN 1999by (Howell et al., 2001), which is a 1991bg-like object and the only type Ia supernova known so far that shows significant polarization. It also shows that iron group elements are always mixed with intermediate mass elements but separated from oxygen and carbon. This is in agreement with observations, the former required by abundance tomography of SN 2005bl, the latter required generally for all type Ia supernovae, as they do not show oxygen emission lines in their nebular spectra (see e.g. Filippenko, 1997).

3.4.5 Nucleosynthesis

To calculate synthetic observables for our model we need to know the detailed nuclear composition of the ejecta. As it is computationally not feasible to evolve a large nuclear reaction network directly with the hydrodynamical code, we try to reconstruct the detailed composition in a post-processing step. To this end we use 150000 tracer particles that are advected with the explosion and record trajectories of density and temperature as described in Travaglio et al. (2004). The initial distribution of the tracer particles according to the mass distribution on the grid is explained in Section 5.3.1. We then use these trajectories to run a large nuclear network on them that contains 384 isotopes up to palladium.

The initial composition of the white dwarf is not known in detail. In explosion simulations of type Ia supernovae it usually assumed that it consists of equal amounts by mass of carbon and oxygen. In addition, a specific metallicity of the white dwarf is assumed. This is realized

Isotope	1	2	3	Isotope	1	2	3
^{12}C	$9.6\,10^{-2}$	$9.3\,10^{-2}$	$9.1\,10^{-2}$	^{44}Ti	$1.1\,10^{-5}$	$8.8\,10^{-6}$	$9.5\,10^{-6}$
^{16}O	$4.8\,10^{-1}$	$5.1\,10^{-1}$	$6.0\,10^{-1}$	^{46}Ti	$6.5\,10^{-10}$	$3.3\,10^{-5}$	$5.1\,10^{-5}$
^{20}Ne	$4.2\,10^{-2}$	$3.8\,10^{-2}$	$3.5\,10^{-2}$	^{48}Cr	$3.4\,10^{-4}$	$2.5\,10^{-4}$	$2.2\,10^{-4}$
^{24}Mg	$1.6\,10^{-1}$	$9.5\,10^{-2}$	$7.1\,10^{-2}$	^{50}Cr	$2.4\,10^{-7}$	$5.0\,10^{-4}$	$4.8\,10^{-4}$
^{26}Mg	$7.3\,10^{-6}$	$1.5\,10^{-3}$	$2.0\,10^{-3}$	^{52}Cr	$1.7\,10^{-9}$	$1.3\,10^{-4}$	$8.9\,10^{-5}$
^{27}Al	$7.3\,10^{-4}$	$5.3\,10^{-3}$	$4.6\,10^{-3}$	^{52}Fe	$6.1\,10^{-3}$	$4.8\,10^{-3}$	$3.9\,10^{-3}$
^{28}Si	$5.6\,10^{-1}$	$5.6\,10^{-1}$	$5.0\,10^{-1}$	^{53}Fe	$3.7\,10^{-5}$	$3.3\,10^{-4}$	$3.1\,10^{-4}$
^{30}Si	$1.3\,10^{-4}$	$1.3\,10^{-2}$	$1.2\,10^{-3}$	^{54}Fe	$1.7\,10^{-5}$	$3.1\,10^{-2}$	$3.1\,10^{-2}$
^{31}P	$2.8\,10^{-4}$	$2.6\,10^{-3}$	$2.4\,10^{-3}$	^{55}Fe	$1.2\,10^{-7}$	$2.6\,10^{-4}$	$2.2\,10^{-4}$
^{32}S	$1.9\,10^{-1}$	$1.9\,10^{-1}$	$2.0\,10^{-1}$	^{56}Fe	$< 10^{-10}$	$6.6\,10^{-4}$	$5.7\,10^{-4}$
^{34}S	$4.1\,10^{-6}$	$9.4\,10^{-3}$	$8.8\,10^{-3}$	^{55}Co	$5.2\,10^{-5}$	$2.7\,10^{-3}$	$2.4\,10^{-3}$
^{36}Ar	$3.1\,10^{-2}$	$2.5\,10^{-2}$	$3.0\,10^{-2}$	^{56}Ni	$1.2\,10^{-1}$	$1.1\,10^{-1}$	$8.1\,10^{-2}$
^{38}Ar	$1.9\,10^{-7}$	$3.5\,10^{-3}$	$4.1\,10^{-3}$	^{57}Ni	$3.5\,10^{-7}$	$1.3\,10^{-3}$	$1.1\,10^{-3}$
^{40}Ca	$2.5\,10^{-2}$	$1.9\,10^{-2}$	$2.2\,10^{-2}$	^{58}Ni	$2.9\,10^{-5}$	$2.1\,10^{-3}$	$2.1\,10^{-3}$

Table 3.2: Final composition of the ejecta of a merger of two $0.89M_\odot$ white dwarfs. Shown are the total masses (in units of $M_\odot$) of the most important isotopes for three different initial compositions of the white dwarfs as explained in the text.

by uniformly mixing ^{22}Ne into the initial carbon/oxygen fuel. ^{22}Ne is synthesized during helium burning from ^{14}N which again was produced during the CNO-cycle and correlates linearly with the metallicity of the progenitor star of the white dwarf. A ^{22}Ne mass fraction of 0.025 corresponds to solar metallicity. To obtain an estimate on the sensitivity of the nucleosynthesis on the initial composition, we do the post-processing for three different cases:

1. A white dwarf with a carbon/oxygen ratio of one and zero metallicity
2. A white dwarf with a carbon/oxygen ratio of one and solar metallicity
3. A white dwarf with a carbon/oxygen profile adopted from Salaris et al. (1997) and solar metallicity

For cases (1) and (2) we use the trajectories of the explosion simulation described above. For case (3) we repeat the explosion simulation, as the energy input from nuclear burning changes as the initial fuel has a smaller carbon mass fraction than 0.5. This simulation is, however, not entirely self-consistent, as we use still use the tables calibrated for a carbon fraction of 0.5 to determine the burning products as the detonation passes, because there are no tables available at the moment for different carbon fractions. We approximate the initial carbon/oxygen profile according to Figure 3 of Salaris et al. (1997) by assuming that the inner $0.6M_\odot$ have a carbon mass fraction of 0.33 and are surrounded by material with an carbon fraction of 0.5. Table 3.2 shows a compilation of the abundances of the most important isotopes in the ejecta.

The composition we obtain in case (1) is in very good agreement with the results of the hydrodynamical simulation, showing that the results of the post-processing are consistent with our assumptions on the nuclear burning products in our approximative burning description used there. It consists mainly of intermediate mass elements (^{24}Mg, ^{28}Si, ^{32}S), a lot of ^{16}O and only very little ^{56}Ni.

The densities of the unburned material are only of the order of 10^7g cm^{-3}. Under these conditions electron captures are negligible. Therefore the electron fraction Y_e is conserved during the nuclear burning. This explains the differences in the final composition between case (1) and (2). In case (1) the electron fraction is exactly 0.5. Thus, isotopes with an equal number of protons and neutrons, i.e. isotopes of the alpha-chain, dominate and neutron-rich isotopes are rare. In case (2), in contrast, the electron fraction is slightly lower, therefore the nuclei contain more neutrons than protons on average. This leads to a substantial buildup of neutron-rich isotopes. For elements like Ti, Cr and Ni this has direct consequences on the optical display of the supernova. The iron group elements in case (1) are completely dominated by ^{56}Ni and the amount of stable iron produced is smaller than $10^{-4} M_\odot$. In contrast, in case (2) about 10% less ^{56}Ni is synthesized, but about 20% of the iron group material is stable iron, mostly ^{54}Fe. The ejecta in case (2) also contain considerably more Ti and Cr as in case (1). This is, however, mainly due to the presence of considerable amounts of the stable, but neutron-rich isotopes ^{46}Ti and ^{50}Cr in case (2). The amounts of ^{44}Ti and ^{48}Cr, both part of the alpha-chain, are similar.

In Chandrasekhar-mass explosion models the carbon/oxygen ratio of the white dwarf only affects the asymptotic kinetic energy of the ejecta (Röpke et al., 2006a). In this merger model, however, owing to the low density, nuclear statistic equilibrium is not reached, but the nuclear reaction rates and the energy release during the burning determine the burning products. Therefore changing the carbon/oxygen ratio of the white dwarfs changes the final composition, as burning carbon releases more energy, leads to a higher temperature and allows the nuclear reactions to burn to heavier nuclei. In case (3), this does not change the basic pattern of the dominant isotopes, but in the end it leads to a slightly smaller production of iron group elements and more remaining unburned oxygen. It can, however, change the abundances of trace elements, i.e. the amount of ^{46}Ti increases by almost a factor of two from case (2) to (3). Therefore, if these trace elements are important for the optical display (like Ti, as discussed later), they introduce a serious uncertainty into its modeling.

3.4.6 Comparison with observations

The detailed abundance distribution of the zero metallicity case and the density structure of the ejecta are then mapped onto a 50^3 uniform Cartesian grid as described in section 5.3.2 and provide the input to radiative transfer modeling. Using the multi-dimensional Monte Carlo radiative transfer code ARTIS (Kromer & Sim, 2009) we obtain synthetic lightcurves and spectra as required to compare our model quantitatively with observations.

Figure 3.8 shows synthetic lightcurves of the explosion in different filter bands. Owing to the small ^{56}Ni mass synthesized during the nuclear burning, they are faint compared to

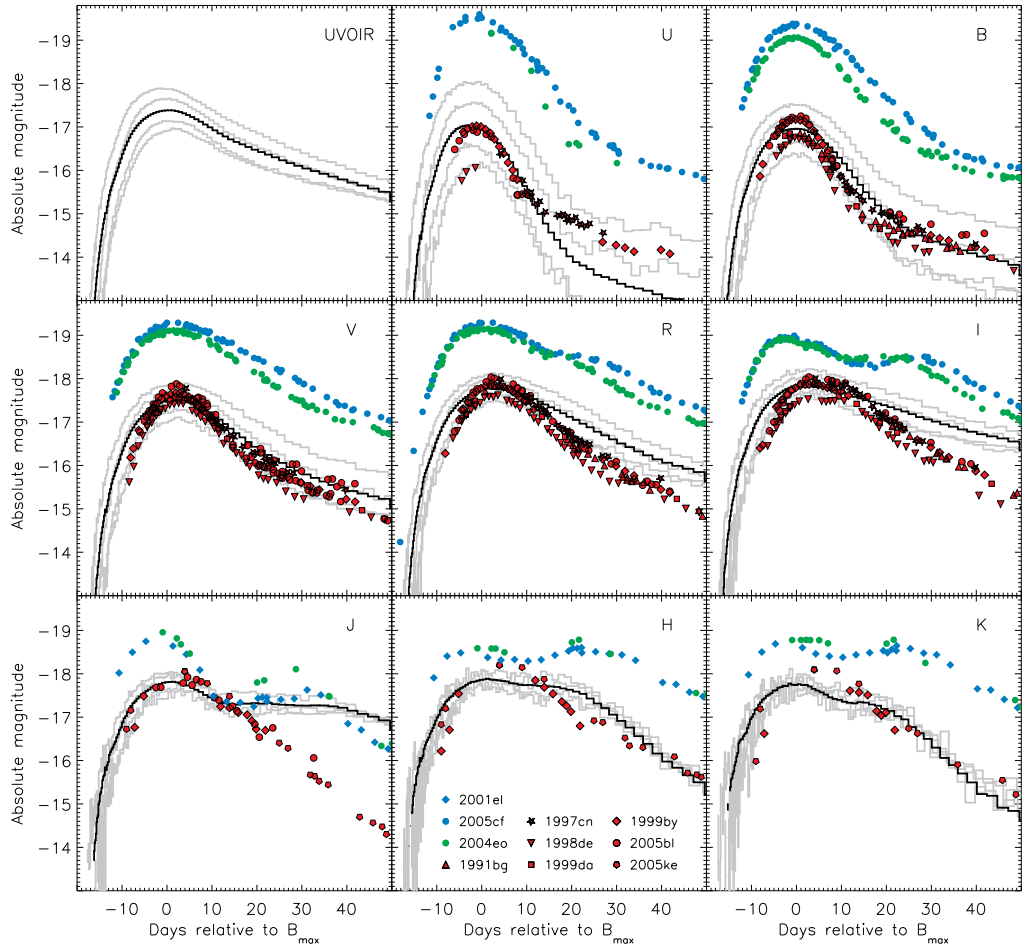

Figure 3.8: Synthetic light curves for the merger of two $0.89M_{\odot}$ white dwarfs. From top left to bottom right the histograms show ultraviolet-optical-infrared bolometric (UVOIR) and broad-band U,B,V,R,I,J,H,K synthetic light curves of our model. The black histograms show angle-averaged light curves. To indicate the scatter in brightness caused by the model asymmetries, four line-of-sight specific light curves (gray histograms) are overplotted. These have been selected from 100 equally sized solid-angle bins such that they represent the full range of the scatter. Time is given relative to B band maximum. Red symbols show observed 1991bg-like type Ia supernovae collected by Taubenberger et al. (2008). For comparison the light curves of the normal type Ia supernovae SN 2005cf (Pastorello et al., 2007b), SN 2001el (Krisciunas et al., 2003) and SN 2004eo (Pastorello et al., 2007a) which represents the faint end of normal type Ia supernovae are also shown. (courtesy: M. Kromer)

those of normal type Ia supernovae. They also decline rapidly, despite the large total ejecta mass of our simulation of $1.8M_{\odot}$. Given that there has been no fine-tuning of the explosion model, the light curves agree remarkably well with the sample of the 1991bg-like type Ia supernovae – both in absolute magnitude and color evolution. Moreover, our model naturally predicts the lack of secondary maxima in the near-infrared (J, H and K) light curves which is a peculiarity of 1991bg-like objects compared with normal type Ia supernovae.

We note that the exact light curve shapes are affected by details of both the nucleosynthesis and the radiative transfer and thus are very sensitive to any systematic shortcomings of the simulations. In particular, necessary approximations in the treatment of the ionization state of the ejecta can influence the decline of the light curves (Kromer & Sim, 2009). By overestimating the strength of the Ca infrared triplet this may be responsible for the excess of light in the I and J band at late times.

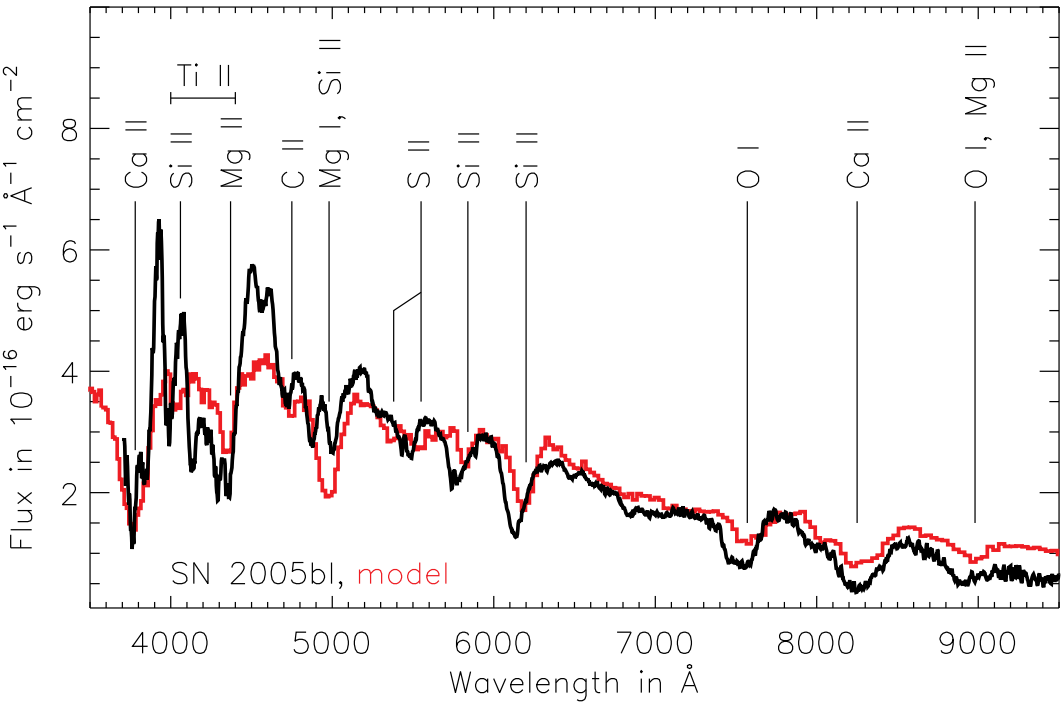

Figure 3.9: Synthetic spectrum for the merger of two $0.89 M_\odot$ white dwarfs. Comparison between SN 2005bl (Taubenberger et al., 2008) three days before B band maximum (black line) and an angle-averaged synthetic spectrum of our model at the corresponding epoch (red histogram). (courtesy: M. Kromer)

Figure 3.9 shows an angle-averaged spectrum of our model three days before maximum light in the B band. Both, the overall flux distribution and the individual spectroscopic features agree remarkably well. Although the features show some variation for different lines-of-sight these are small and the angle-averaged spectrum is representative.

Observationally, 1991bg-like supernovae are characterized by several distinct features. To show that our model can accommodate for all of these characteristics they will discussed one by one in detail in the following. We note, however, that since they are observational signatures, not all of them necessarily constrain the explosion physics but some are, from the explosion modeling perspective, details.

These characteristics are:

I) **Low luminosity**
We obtain a peak magnitude of ≈ −17 mag in B-band, exactly as required for 1991bg-like type Ia supernovae. This prediction is a direct consequence of the low ^{56}Ni mass synthesized in our simulations.

II) **Narrow light curves**
Our model predicts light curves which are narrow compared to those of typical type Ia supernovae. This is as observed for 1991bg-like type Ia supernovae. Close comparison shows that our synthetic light curves fade slightly less quickly after maximum than observations of 1991bg-likes suggest. However, there are caveats associated with the radiative transfer calculations which may affect the details here. Using a different approximation for the treatment of ionization in the ARTIS code produces a change of 0.3 in $\Delta m_{15}(B)$. This degree of sensitivity is comparable to the difference between its state-of-the-art NLTE treatment (which yields $\Delta m_{15}(B) = 1.4$) and the observed value ($\Delta m_{15}(B) \approx 1.8$). A discussion of the uncertainties of $\Delta m_{15}(B)$ can be found in Sim et al. (2010).

III) **Red colors**
The colors of our model are in excellent agreement with the observations of 1991bg-like events. For example, around maximum light our model gives a mean B-V color of 0.53, V-R of 0.27 and V-I of 0.36. Observed 1991bg-like SNe (SN2005bl, specifically) have B-V, V-R and V-I of 0.61, 0.21 and 0.25, respectively compared to 0.05, 0.06 and −0.16 for a normal type Ia supernovae (SN2004eo, specifically).

IV) **Secondary maxima in infrared lightcurves**
Normal type Ia supernovae (see e.g. blue/green points in Figure 3.8) show two distinct maxima in their near infrared light curves (J, H and K bands). 1991bg-likes do not. This characteristic is reproduced by our model.

V) **Low expansion velocities**
In agreement with observations of 1991bg-like SNe, our model predicts expansion velocities (which are measurable via line features in the spectrum) that are significantly low compared to normal type Ia supernovae. Low velocities are a generic and physical consequence of our model since it involves low explosion energies and high ejecta masses. The exact values, however, depend sensitively on details of the description of nuclear burning in the simulations. Comparing with the observations of SN 2005bl our predictions for the line velocities are slightly too low (e.g. by about 5% for the Ca II NIR triplet at maximum light and 25% for Si II and O I). However, discrepancies at this level are not a major challenge for the model but merely an indication that details of the nuclear burning physics would need to be treated more accurately for perfect agreement.

VI) **Relatively strong intermediate mass elements in the spectrum**
As incomplete silicon burning occurs in most of the material reached by the detonation, intermediate mass elements are synthesized in a large fraction of the ejecta. In agreement with observations of 199bg-like type Ia supernovae, our radiative transfer calculations show that this leads to strong features in the spectra.

VII) **Strong O I features in the spectrum**
Compared to many models for normal type Ia supernovae, our model predicts rather large masses of unburnt material (carbon/oxygen) in the outer ejecta. As can be seen in the spectrum (Figure 3.9), this material is responsible for strong O I features in the spectra, as observed for 1991bg-like SNe.

VIII) **Ti II in the spectrum**
Titanium is responsible for a very strong observational feature in the spectra of 1991bg-like objects between 4000A and 4440A. Although our model, which contains only $\approx 10^{-5} M_\odot$ of titanium, shows some hints of a titanium trough, it is not as deep as expected from observations. However, this feature can be readily formed with only a tiny amount of this element in the supernova ejecta. Titanium is synthesized as a trace element in the explosion, as discussed in paragraph 3.4.5. As such, the exact amount produced is very sensitive to the chemical composition of the progenitor and can easily vary by a large factor, as discussed above. We find, that already $\approx 8 \cdot 10^{-5} M_\odot$ of titanium are enough to reproduce observations, which is clearly within the uncertainties. Therefore, we conclude that the strong titanium feature is not a meaningful test of the explosion mechanism, but rather a powerful probe of the chemical composition of the progenitor.

IX) **Asphericity**
Polarization measurements of spectra are able to determine the geometry of the ejecta. Normal type Ia supernovae show no deviation from spherical symmetric of their ejecta. For SN 1999by, which belongs to the class of 91bg-like supernovae, there are observations that show an overall continuum polarization of $\approx$ 0.3% – 0.8% (Howell et al., 2001). This is consistent with a degree of asphericity of $\approx$ 20%, assuming that the object was observed equator-on. Our model provides a natural explanation for the polarization of spectra of 1991bg-like objects, as the explosion is intrinsically asymmetric. By extracting the shapes of the surfaces of photon last-scattering from the radiative transfer simulation we find an upper limit on the asphericity of around 40%. This is consistent with the ejecta structure as we see it in our hydrodynamical simulation (axis ratio of $2 : 1$) and the observed value for SN 1999by. If future studies confirm, that all 1991bg-like type Ia supernovae show polarization at the same level, this would strong support the merger scenario, as it is difficult to explain large scale asymmetries in the single-degenerate scenario where one single, at least initially spherical, white dwarf explodes.

X) **Preference for an old stellar population**
Recent observations find that rates of type Ia supernovae with broad light curves are proportional to the star formation rate in their environment while rates of type Ia supernovae with narrow light curves are not (Sullivan et al., 2006). This means, that we find a tendency for subluminous (narrow light curve) type Ia supernovae to occur preferably in old stellar populations compared to normal and bright (broad light curve) type Ia supernovae. Population synthesis calculations by A. Ruiter (personal communication) show that for all considered potential progenitor systems of normal type Ia supernovae, the ratio between the number of mergers of two white dwarfs with

a mass ratio of ≈ 1 and a primary mass of ≈ $0.9M_\odot$ and normal type Ia supernovae always increases strongly with delay time. Therefore, this class of progenitors is able to reproduce the preference for old stellar populations shown by subluminous type Ia supernovae.

To be able to explain the whole class of 1991bg-like type Ia supernovae with our merger scenario, these mergers have to be frequent enough to reproduce their observed rate. The rate of 1991bg-like type Ia supernovae, however, still carries some uncertainties. As supernova surveys are usually magnitude limited, they have a strong bias towards finding luminous type Ia supernovae, but miss subluminous ones. Therefore, to determine a rate per stellar mass, the observed rates from magnitude limited surveys have to be corrected for this bias. Of course, this introduces large uncertainties into the rate estimates. Recent estimates conclude that they may account for ≈ 10% of all type Ia supernovae, with an uncertainty of at least a factor of two.

Using the StarTrack population synthesis code (Ruiter et al., 2009; Belczynski et al., 2002, 2008), A. Ruiter calculated the rates expected for our scenario. Assuming that all mergers of two white dwarfs with a primary mass between $0.85M_\odot$ and $1.05M_\odot$ and a mass ratio $q > 0.9$ lead to a 1991bg-like type Ia supernova, they contribute ≈ 2 – 11% to the total type Ia supernova rate, depending on the choice for the main progenitor channel.

3.4.7 Changing the mass ratio

If the merger scenario we present here is frequent enough to account for a significant fraction of all type Ia supernovae, it has to work also for moderate mass differences between the two white dwarfs. Thus, we have to check how different mergers with the same primary white dwarf mass and a mass ratio slightly smaller than one compare to the equal mass merger discussed above. Only if it works in the same way for mergers with a range of smaller mass ratios, specifically the formation of a detonation, the scenario will be more than an exotic possibility. To test this, we compared three different mergers. All have the same primary mass of $0.9M_\odot$, but different secondary masses of $0.89M_\odot$, $0.81M_\odot$ and $0.7M_\odot$ which is equivalent to mass ratios of 0.99, 0.9 and 0.78. They have initial periods of 25 s, 33 s and 40 s respectively.

Figure 3.10 shows the density and temperature of all particles of these simulations at the time when the conditions are most favorable for a detonation and temperature slices through the centers of the binaries. Obviously, there are considerable differences between these three systems. First, with decreasing mass ratio, the merger becomes less violent. While the two mergers with mass ratios of 0.99 and 0.9 produce several hot particles that ignite carbon and reach temperatures above $2 \cdot 10^9$K, this is not the case for the merger with the smallest mass ratio. It is still possible, that when we resolve the interaction region better we will also find hotter particles, but at the moment it seems more likely that below a specific mass ratio the merger is just not violent enough to ignite a detonation. Another difference is the dynamical effect of the merger on the primary white dwarf. In a nearly equal mass merger the primary white dwarf is heavily distorted and its material mixed with hot material of the secondary white dwarf. For a mass ratio of 0.9, the primary white dwarf remains unaffected in the center, but its surface is distorted. For the smallest mass ratio of 0.78, it stays completely

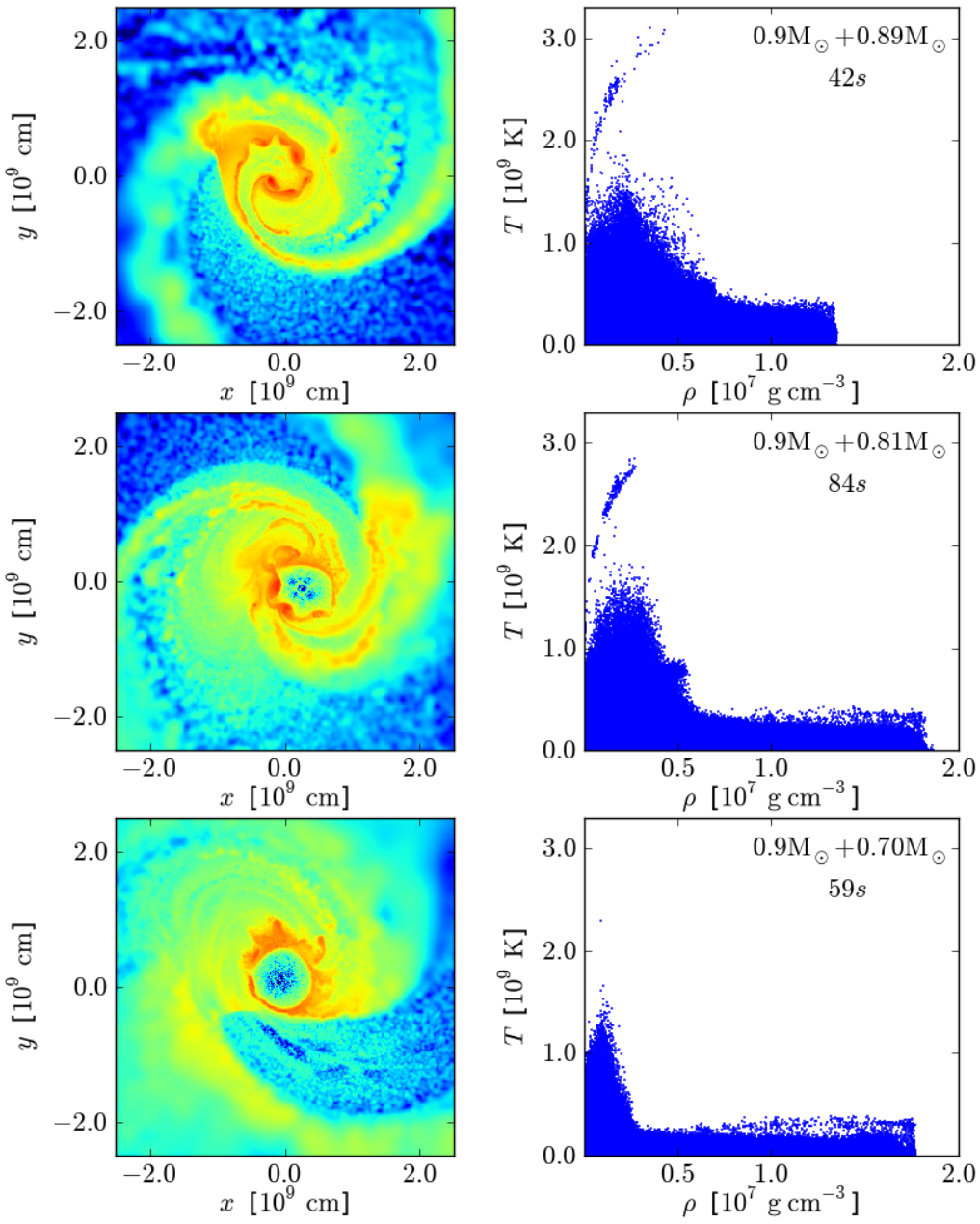

Figure 3.10: Temperature slice and density-temperature scatter diagram for three mergers with the same primary white dwarf, but different secondary white dwarfs. The rows show a temperature slice (on the left) and the distribution of all particles in temperature-density space (on the right) at the time that seems to provide the most favorable conditions for a detonation. Red/blue colors indicate high/low temperatures.

intact and cool surrounded by the material of the disrupted less massive companion. This difference can also be seen in the left panels in Figure 3.10. In the q = 0.99 merger the central density of the remaining white dwarf is smaller than in the other two cases. As for these mergers the amount of ^{56}Ni produced depends sensitively on the central density of the remaining white dwarf, this leads to higher ^{56}Ni masses in mergers with smaller mass ratios.

While this does not change the scenario fundamentally, it breaks the relation between mass of the primary white dwarf and the final ^{56}Ni mass of the explosion for dim explosions. For more massive explosions, however, where most of the ^{56}Ni is produced in nuclear statistical equilibrium, this will be a minor effect only.

3.5 Dark explosions from low-mass mergers

Carbon/oxygen white dwarfs are typically born with a mass smaller than $0.9M_\odot$. As shown above, there are good indications to assume that mergers of two $0.9M_\odot$ white dwarfs make up a significant fraction of all type Ia supernova events. Since less massive mergers can be expected to be even more frequent, it is interesting to look at their outcome theoretically and compare it to observational constraints. Therefore, we chose to model the merger of two $0.8M_\odot$ carbon/oxygen white dwarfs, the same way we modeled the more massive merger described above.

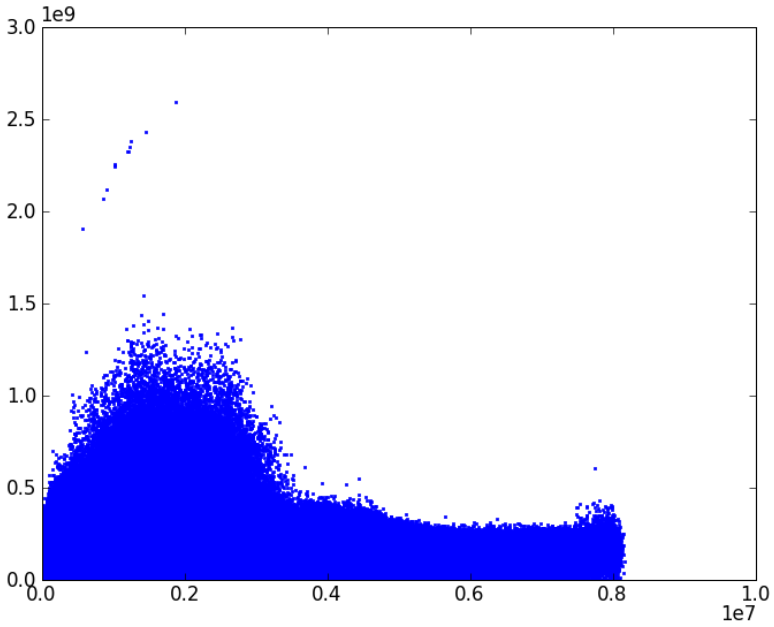

Figure 3.11: Density vs. Temperature scatter plot for all particles of the merger of two $0.8M_\odot$ white dwarfs after 49s.

Both white dwarfs are made up of pure carbon and oxygen with equal mass fractions. Their central densities are $8.7 \cdot 10^6$g cm^{-3}. As these densities are below the threshold of about 10^7g cm^{-3} at which a detonation produces iron group elements, any nuclear burning should produce only negligible amounts of ^{56}Ni, as long as there is no mechanism that increases the density prior to burning. The initial period of the binary system is 33 s. Both white dwarfs are represented by of 10^6 equally massive SPH particles.

Compared to a $0.9M_\odot$ white dwarf, the $0.8M_\odot$ white dwarfs are larger and less compact. Therefore, the merger itself is less violent. Figure 3.11 shows temperature vs. density for all particles 49 s after the start of the simulation. Whereas there are a few particles that become hot enough to ignite carbon burning, this happens at quite low densities below $2 \cdot 10^6$g cm^{-3}. Thus, according to the criteria for the conditions required to form a detonation (see, e.g. Seitenzahl et al., 2009) it seems unlikely that it is triggered. Nevertheless, we assume in the following that a detonation forms. The idea is to see how a hypothetical explosion in that case would look like and whether it compares to anything known from observations.

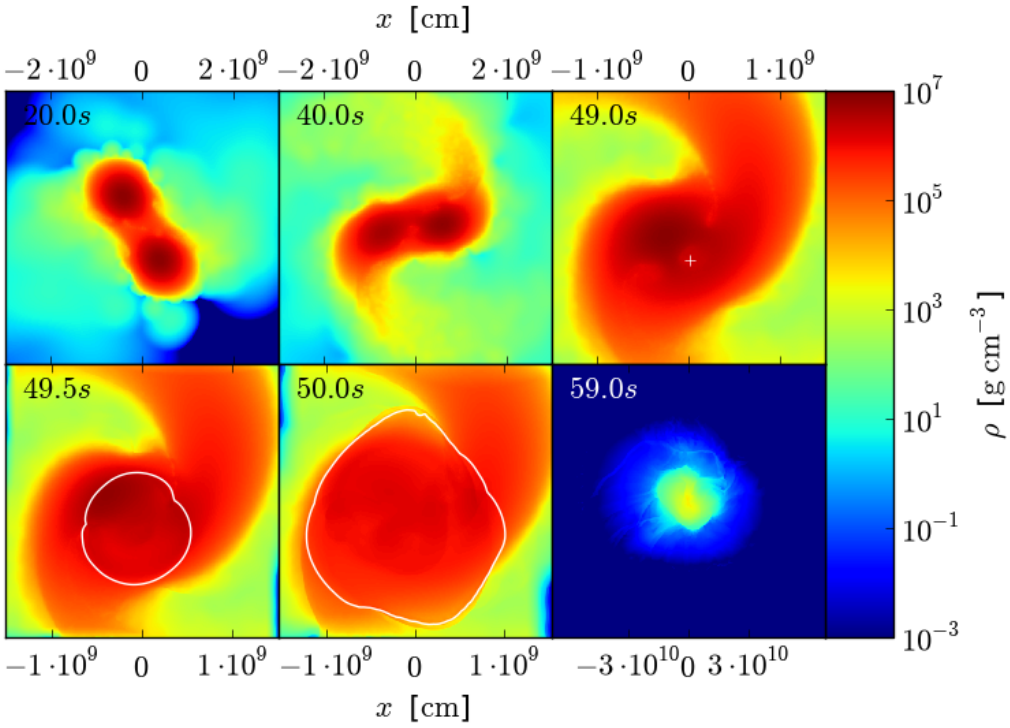

Figure 3.12: Density evolution of the merger and the explosion of two $0.8M_\odot$ carbon/oxygen white dwarf. Color-coded is the logarithm of the density. The white cross in the upper right panel indicates the point where the detonation is ignited. The white contours show the position of the detonation front.

Figure 3.12 shows the density evolution of the merger and the subsequent explosion. The white cross shows where the detonation has been started artificially after 49s. At that time the simulation was mapped from SPH onto a uniform Cartesian grid and 150,000 Lagrangian tracer particles were added to record temperature and density trajectories for subsequent post-processing.

At the time the detonation starts, the binary has already merged to a large extend and created a single, nearly spherical object that contains most of the mass of the initial system. The detonation takes only about one second to burn most of this object. The energy release

from nuclear burning is sufficient to unbind the merged object. After 100 s, when the ejecta have reached a state of homologous expansion, they have an asymptotic kinetic energy of $1.1 \cdot 10^{51}$erg.

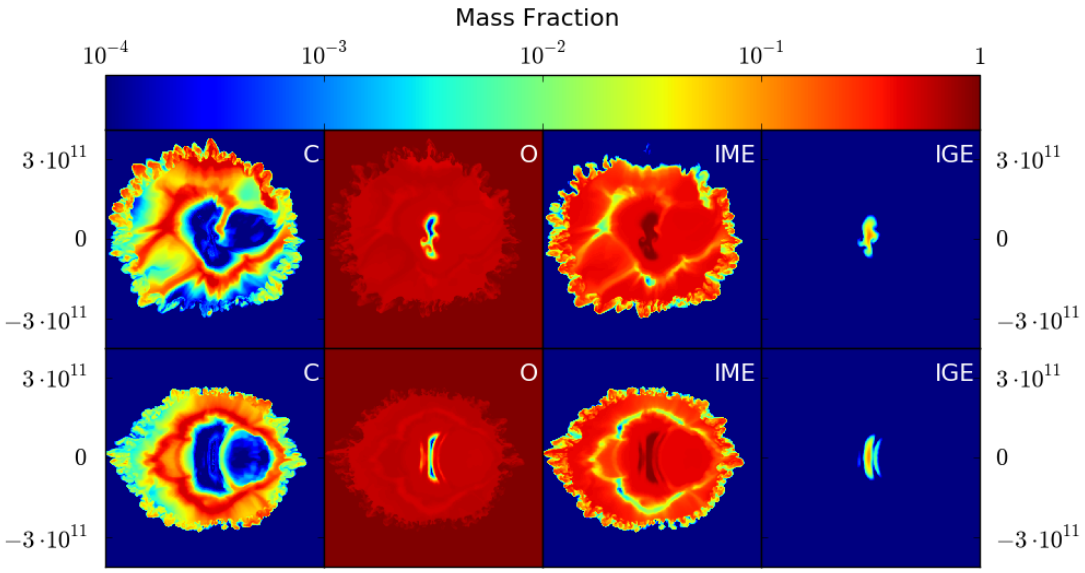

Figure 3.13: Final composition of the ejecta in homologous expansion 100s after the explosion. The panels show from the left to the right the abundances of carbon, oxygen, intermediate mass elements and iron group elements. The upper and lower panels show the system viewed face-on and edge-on, respectively.

The final composition contains less than $10^{-2}M_\odot$ of iron group elements, as expected. Most of the material ($0.91M_\odot$) has been burned to intermediate mass elements. Only $0.02M_\odot$ of carbon, but $0.58M_\odot$ of oxygen remain unburned. Figure 3.13 shows the spatial distribution of the composition after the ejecta have reached homologous expansion. Only the very center of the object consists of almost pure intermediate mass elements with a very small contribution of iron group elements. It is surrounded by a large, close to spherical, layer containing oxygen and intermediate mass elements. Using the trajectories recorded by the tracer particles to conduct a detailed nucleosynthesis study on the nuclear burning and assuming an initial pure carbon/oxygen composition (i.e. zero metallicity), we find that only $4 \cdot 10^{-3}M_\odot$ of ^{56}Ni and virtually no other iron group elements are synthesized in the explosion.

An explosion that produces only between $10^{-2}M_\odot$ and $10^{-3}M_\odot$ of ^{56}Ni is significantly fainter than the faintest observed type Ia supernovae, which are 1991bg-like events with a ^{56}Ni mass around $0.1M_\odot$. It is possible that events like this have not yet been observed, as

they are very faint and therefore could have been missed by observations. This, however, sounds unlikely, as recently type Ib supernovae have been found with inferred ^{56}Ni of about $10^{-2}M_\odot$ (see, e.g. Kawabata et al., 2010; Perets et al., 2010). There are speculations, that these events are of thermonuclear origin, as they occur in old, elliptical galaxies without recent star formation. As they show strong helium features, however, we can exclude that they have anything to do with mergers of two carbon/oxygen white dwarfs. Though they may be connected with mergers of white dwarfs with at least one of the consisting of helium.

All taken together, it seems unlikely that objects like the one we modeled exist. The simplest explanation for their non-existence is that during the merger no detonation forms. In this case, the merger creates a single object with a mass larger than the Chandrasekhar-mass. As the temperatures are high enough to ignite carbon, the object will convert all its carbon to oxygen and neon, turning it into an oxygen/neon white dwarf. When this white dwarf relaxes, its central density increases. Since it is too massive to be stable, it will collapse at some point, as shown by Saio & Nomoto (1985).

3.6 Normal type Ia supernovae from mergers of white dwarfs

Carbon/oygen white dwarfs that are born with larger masses are less frequent. Thus, mergers of two white dwarfs which both have a mass larger than $0.9M_\odot$ should be considerably less frequent than mergers of two $0.9M_\odot$ white dwarfs. Their merger, however, will be more violent as the white dwarfs are more compact. Thus, the conditions to form a detonation during the process of merging should be even better than for the merger of two $0.9M_\odot$ white dwarfs we studied. They should also produce more ^{56}Ni, as nuclear burning takes place at higher densities on average. Therefore, they may contribute some events in the brightness range of normal type Ia supernovae. They are, however, certainly not frequent enough to account for a dominant fraction of all type Ia supernovae. Nevertheless, they could contaminate cosmological samples, if they do not follow the Phillips relation.

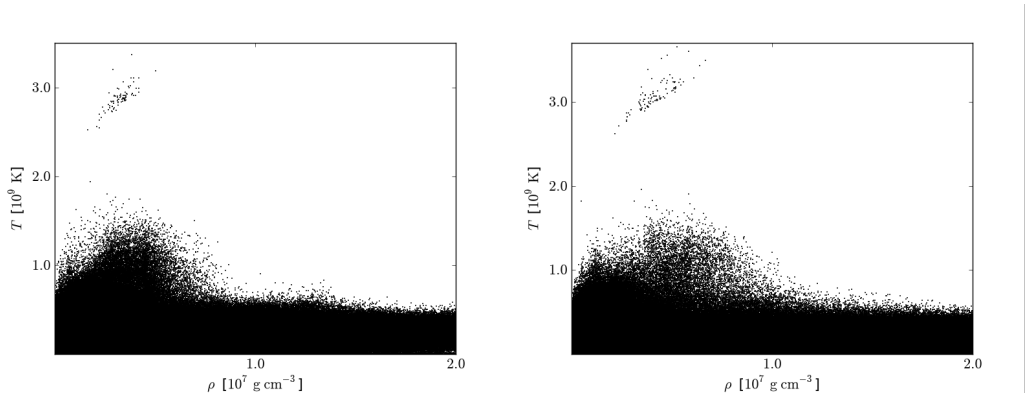

Figure 3.14: Density vs. Temperature scatter plot for all particles of the merger of two $1.0M_\odot$ white dwarfs after 42s (left panel) and the merger of two $1.1M_\odot$ white dwarfs after 40s (right panel).

Here, we study two mergers of two $1.0M_\odot$ and two $1.1M_\odot$ white dwarfs, respectively. The merger of two $1.0M_\odot$ white dwarfs starts with an initial orbital period of 21 s, the merger of two $1.1M_\odot$ with a period of 16 s. Both mergers contain a total of two million equally massive SPH particles. Thus, each white dwarf is resolved with one million particles. In both cases the binary is stable for more than 30s until one of the two white dwarfs breaks up under the influence of tidal forces from the other one. Figure 3.14 shows density and temperature of all particles for both mergers after 42 s and 40 s, respectively. At these times, in both simulations some particles have been heated up to temperatures larger than $3 \cdot 10^9$K at densities up to $5 \cdot 10^6$g cm^{-3}. As far as we know, these conditions are sufficient to allow the formation of a detonation. Thus, we map the simulations onto a grid, ignite the detonation at their hottest spots, and follow the explosions.

Figure 3.15 and Figure 3.16 show the evolution of the merger of the two $1.0M_\odot$ white dwarfs and the two $1.1M_\odot$, respectively. In both explosions, the white dwarf that is still intact is burned first, the remains of the disrupted secondary white dwarf afterwards. Iron group elements are only synthesized in the burning of the primary white dwarf, as the densities in the remains of the other are too low.

The merger of two carbon/oxygen $1.0M_\odot$ white dwarfs in the end produces $1.2M_\odot$ of intermediate mass elements and $0.4M_\odot$ of iron group elements. Less than $0.01M_\odot$ of carbon, but $0.4M_\odot$ of oxygen remain unburned. As the densities are too low to cause neutronization and we assume that the white dwarfs initially contain only carbon and oxygen, ^{56}Ni completely dominates the iron group elements. Virtually no stable iron group elements are synthesized. The ejecta reach homologous expansion after about 10s with a final asymptotic kinetic energy of $1.7 \cdot 10^{51}$erg.

As its remaining white dwarf is denser in the center, the merger of two $1.1M_\odot$ white dwarfs produces more ^{56}Ni. It synthesizes $0.7M_\odot$ of iron group elements (which is basically only ^{56}Ni, for the same reasons as before) and $1.3M_\odot$ of intermediate mass elements. The ejecta contain only about $0.15M_\odot$ of oxygen and less than $0.01M_\odot$ of carbon. Since the energy release from nuclear burning surpasses the gravitational binding energy of the merged object, it is disrupted and explodes. The asymptotic kinetic energy of the explosion reaches $2.2 \cdot 10^{51}$erg.

Figure 3.17 shows the distribution of the main groups of elements in velocity space for both mergers, when their ejecta are in homologous expansion. In both cases, the iron group elements are located mainly in the center of the ejecta. As their mass fraction becomes smaller with larger radius, the fraction of intermediate mass elements and oxygen increases. The outer parts of the ejecta are made up of intermediate mass elements and oxygen. Intermediate mass elements are basically present in the ejecta over the whole velocity range. This is at least partly a result of the non-spherical geometry of the ejecta, that can be seen in the lower right panels of Figures 3.15 and 3.16.

Compared to Chandrasekhar-mass models, kinetic energy and mass of the ejecta are larger. The specific kinetic energy is lower for the merger of two $1.0M_\odot$ white dwarfs and

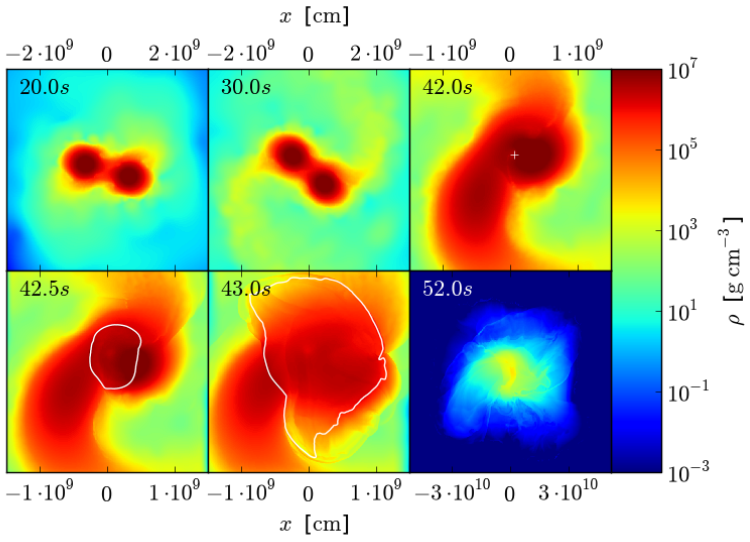

Figure 3.15: Density evolution of the merger and the explosion of two 1.0$M_\odot$ carbon/oxygen white dwarf. Color-coded is the logarithm of the density. The white cross in the upper right panel shows the point where the detonation is ignited. The white contours show the position of the detonation front.

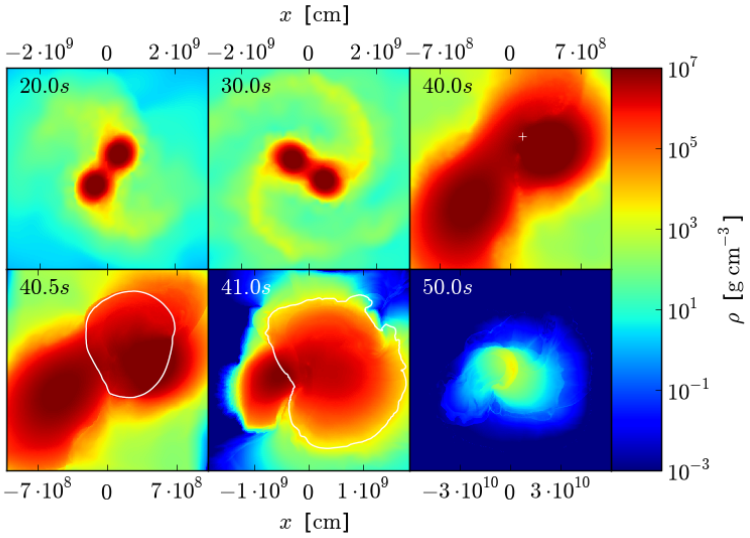

Figure 3.16: Density evolution of the merger and the explosion of two 1.1$M_\odot$ carbon/oxygen white dwarf. Color-coded is the logarithm of the density. The white cross in the upper right panel shows the point where the detonation is ignited. The white contours show the position of the detonation front.

higher for the merger of two 1.1$M_\odot$, compared to the standard W7 model that is often used as a reference for a normal type Ia supernova. This is a result of the average density ahead of the flame, that determines the outcome of nuclear burning. As most of the mass has higher

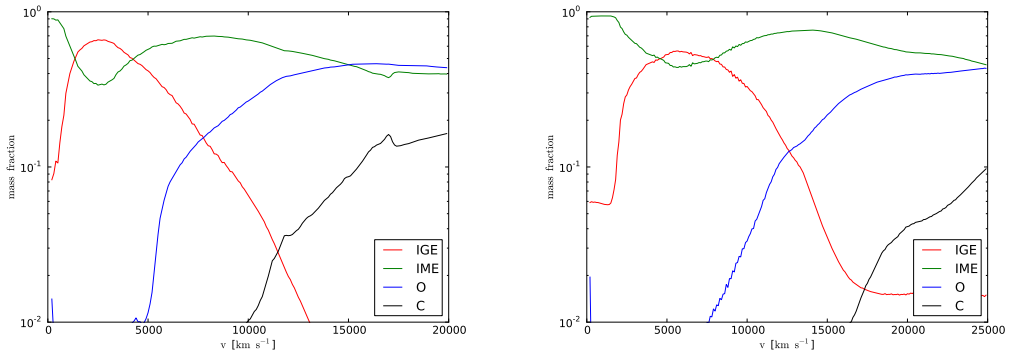

(a) $1.0M_{\odot} + 1.0M_{\odot}$ (b) $1.1M_{\odot} + 1.1M_{\odot}$

Figure 3.17: Composition in velocity space from the explosion of a merger of two equally massive carbon/oxygen white dwarfs

density in the more massive merger, nuclear burning proceeds further and more energy is released per mass burned. Thus, for these models there might be a trend, that more massive mergers show higher line velocities than less massive events.

Not surprisingly, both mergers fulfill the basic criteria that are needed to resemble a type Ia supernova. Their ejecta contain a core of iron group material surrounded by a layer of intermediate mass elements with carbon and oxygen only in the outer layers. They also have reasonable ^{56}Ni-masses and produce approximately the right amount of kinetic energy. However, to see whether their optical display will really resemble observed events, detailed radiative transfer modelling will be needed that allow us to compare synthetic light curves and spectra of these models to observed objects. Also, it has to be shown whether the asymmetries of the ejecta are in agreement with spectropolarimetry observations of normal type Ia supernovae that show no significant polarization (Wang & Wheeler, 2008).

3.7 Superluminous type Ia supernovae: mergers of the most massive CO white dwarfs?

In recent years, the class of superluminous objects has been added to the subclasses of type Ia supernovae. These objects, that were spectroscopically classified as type Ia supernovae due to their silicon line and lack of hydrogen and helium are considerably more luminous than all previously known type Ia supernovae and a factor of two more luminous than normal ones. Table 3.3 lists all analyses of superluminous type Ia supernovae published so far. A luminosity as high as for these objects is hard to explain in standard models of type Ia supernovae, in which the optical display is powered by the decay of ^{56}Ni only. There are, however, no indications that the lightcurves of superluminous type Ia supernovae are powered by additional sources of energy. The spectra do not contain any narrow emission lines that would be expected in case interaction with interstellar medium converts kinetic

into thermal energy and subsequently radiation. Also, the decay of the lightcurves is consistent with being powered by the initial decay of ^{56}Ni and later further decay of ^{56}Co only. Thus, any additional source of radiation would have to follow the same time dependence as the decay of ^{56}Ni. This basically excludes a significant contribution from the decay of other radioactive nuclei and puts strong constraints on any other mechanism that generates additional radiation.

Supernova	Publication	$M_{^{56}\mathrm{Ni}}$ [$\mathrm{M}_\odot$]	M_{ejected} [$\mathrm{M}_\odot$]
2003fg	Howell et al. (2006)	1.29 ± 0.07	~ 2.1
2006gz	Hicken et al. (2007)	1.20 ± 0.28	no estimate
2007if	Scalzo et al. (2010)	1.6 ± 0.1	2.4 ± 0.2
2007if	Yuan et al. (2010)	1.5	no estimate
2009dc	Yamanaka et al. (2009)	1.2 ± 0.3	no estimate
2009dc	Silverman et al. (2010)	1.7 ± 0.4	> 2

Table 3.3: List of analyses of superluminous type Ia supernovae published so far

Table 3.3 also shows estimates of the ^{56}Ni mass and the total ejected mass from light curve and spectral fitting for superluminous supernovae, all assuming that ^{56}Ni alone powers the lightcurves. The ^{56}Ni masses found range from $1.2\mathrm{M}_\odot$ up to $1.7\mathrm{M}_\odot$, the ejecta masses from $2\mathrm{M}_\odot$ to $2.4\mathrm{M}_\odot$. Although these estimates (in particular the estimates of the total ejecta mass) bare large uncertainties, these ^{56}Ni and ejecta masses are not allegeable within the framework of Chandrasekhar-mass or sub-Chandra models. Khokhlov et al. (1993) showed that a pure detonation of a Chandrasekhar-mass white dwarf solely produces iron group elements, but only $0.92\mathrm{M}_\odot$ of ^{56}Ni due to high neutronization in the center. If the Chandrasekhar-mass white dwarf is pre-expanded slightly for some reason before the detonation starts, this can be avoided. However, the explosion in this case also produces at most $1.1\mathrm{M}_\odot$ of ^{56}Ni (Meakin et al., 2009). In addition, any Chandrasekhar-mass model producing $1.2\mathrm{M}_\odot$ of ^{56}Ni will not produce enough intermediate mass elements to explain i.e. the strong Si II line. Furthermore, contrary to naive expectations, superluminous type Ia supernovae show very low line velocities, suggesting small specific kinetic energies and even larger ejecta masses compared to normal ones. Thus, summed up, there is clear evidence that these explosions originated from a super-Chandrasekhar-mass progenitor.

Given the high ^{56}Ni and ejecta mass inferred for the first superluminous type Ia supernova 2003fg, Howell et al. (2006) proposed that it may originate from differentially rotating super-Chandrasekhar white dwarfs as described by Yoon & Langer (2005). They speculated that such a massive white dwarf may arise from a very long accretion phase or the merger of two massive white dwarfs. Here, we present the first model of a merger of two massive ($1.0\mathrm{M}_\odot$ and $1.2\mathrm{M}_\odot$) white dwarfs.

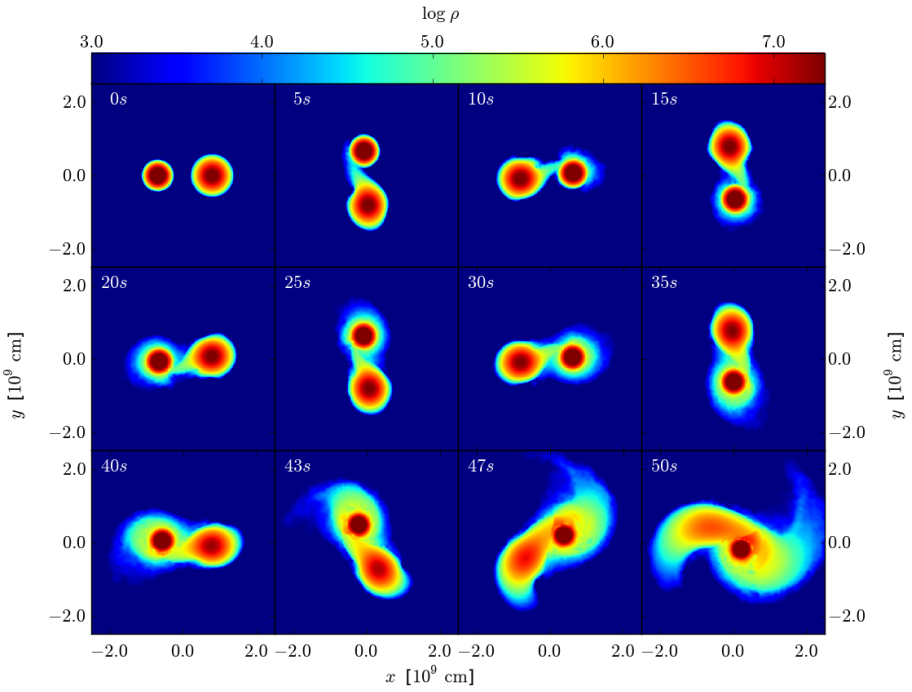

Figure 3.18: Density evolution of the merger of a $1.2M_{\odot}$ and a $1.0M_{\odot}$ white dwarf. Color-coded is the logarithm of the density.

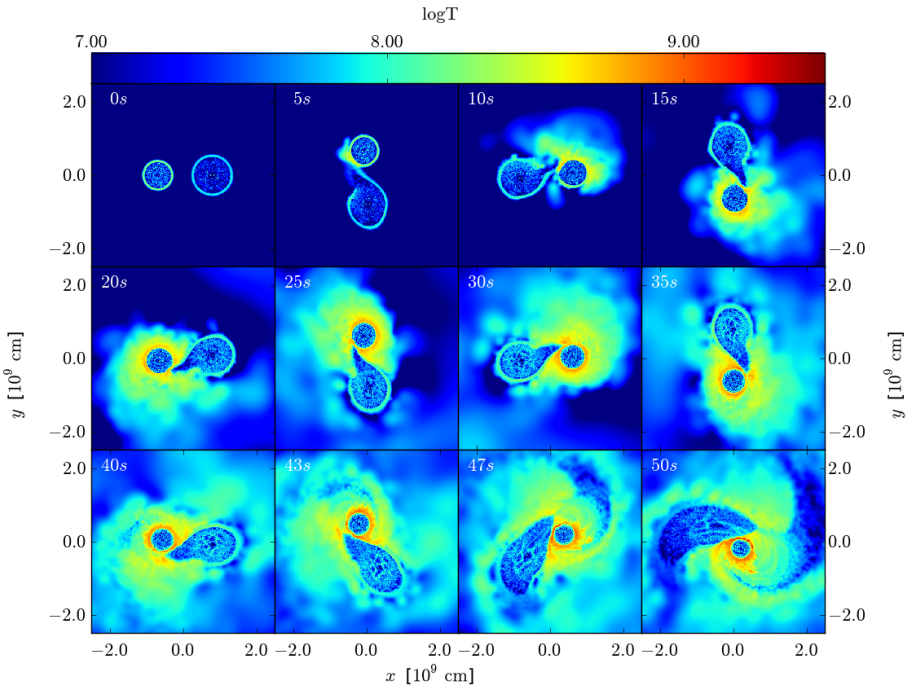

Figure 3.19: Temperature evolution of the merger of a $1.2M_{\odot}$ and a $1.0M_{\odot}$ white dwarf. Color-coded is the logarithm of the temperature.

3.7.1 Modeling the merger

The initial binary system consists of two white dwarfs of $1.0M_\odot$ and $1.2M_\odot$ (and thus a mass ratio of 0.83) with central densities of $1.2 \cdot 10^8$g cm^{-3} and $2.8 \cdot 10^7$g cm^{-3}, respectively. Both have an initial temperature of $5 \cdot 10^5$K and consist of 50% ^{12}C and 50% ^{16}O. The white dwarfs orbit around their common center of mass with an initial period of 21s. The primary, $1.2M_\odot$ white dwarf consists of 10^6 particles of equal mass. The secondary, $1.0M_\odot$ white dwarf is represented by $\sim 8.3 \cdot 10^5$ particles of the same mass as the particles of the primary white dwarf.

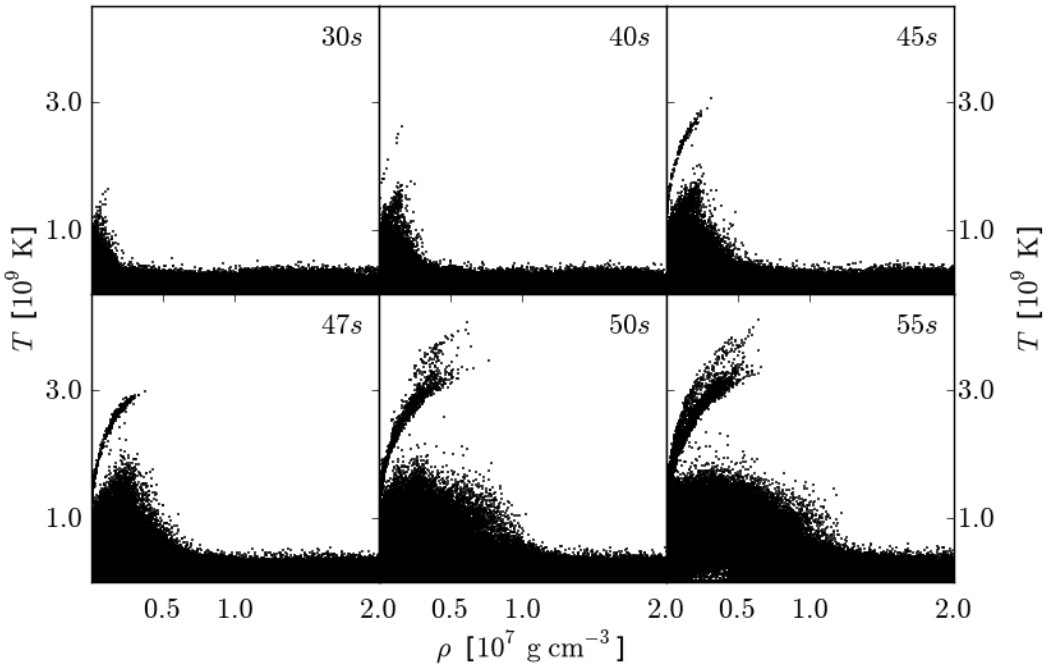

Figure 3.20: Density vs. Temperature scatter plot for all particles of the merger of a $1.2M_\odot$ and a $1.0M_\odot$ white dwarf.

Figures 3.18 and 3.2 show the density and temperature evolution of the binary system. The larger, less massive secondary white dwarf quickly fills its Roche-lobe and slow mass transfer onto the primary white dwarf starts. This mass transfer goes on for about two orbits heating the envelope of the primary white dwarf slightly. After about 40s the secondary white dwarf starts to break up and the mass transfer becomes more violent. Hence, temperatures on the surface of the primary white dwarf increase strongly up to values larger than $3 \cdot 10^9$K, high enough for carbon fusion. At the same time, the central density of the secondary white dwarf drops below 10^7g cm^{-3}. The temperature and density of all particles is shown in Figure 3.20 for different times. The maximum temperature stays below $2 \cdot 10^9$K during the mild accretion phase. After around 40s, when the accretion becomes violent, it starts to increase beyond $3 \cdot 10^9$K. A few seconds later a whole bunch of particles at the surface of

the primary white dwarf are hotter than $3 \cdot 10^9$K, some of them up to $4 \cdot 10^9$K, at densities of $5 \cdot 10^7$g cm^{-3}. Applying the criteria of Seitenzahl et al. (2009), these conditions should lead to the formation of a detonation. The merger is considerably more violent compared to the less massive mergers discussed above, as the primary white dwarf is heavier and more compact, even though the mass ratio is smaller.

3.7.2 The explosion

We map the merging object to our grid code after 47 s as described in Section 5.3.2 and start a detonation in the cell with the highest temperature. Figure 3.21 shows the propagation of the detonation and the subsequent evolution of the object until its complete disruption. In contrast to less massive mergers, in this case dynamic effects are important.

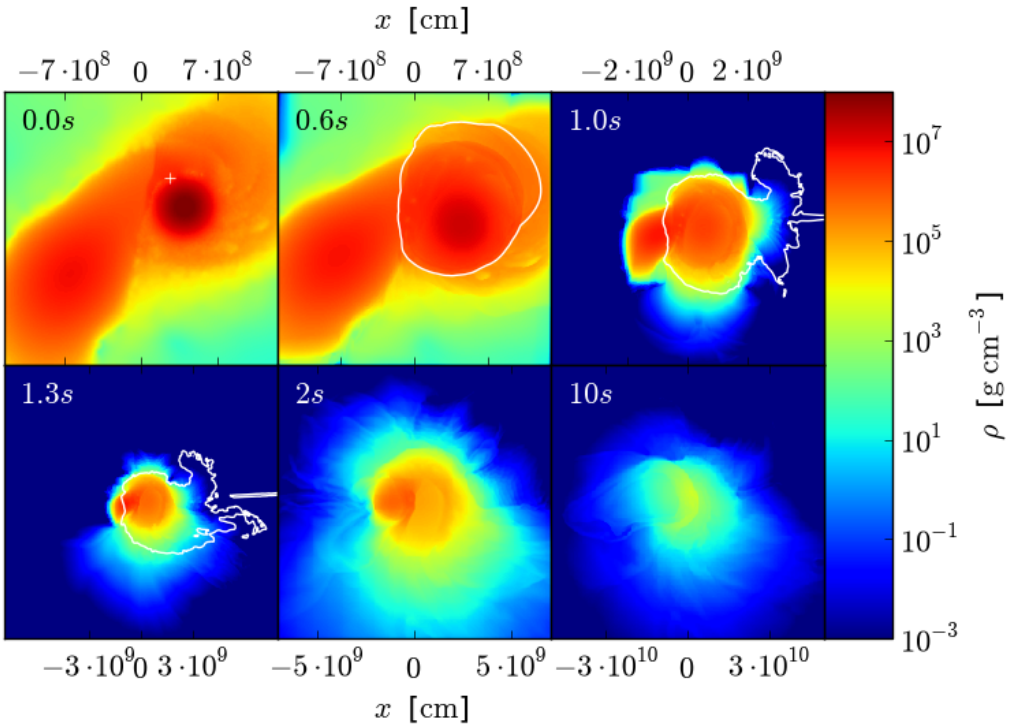

Figure 3.21: Density evolution of the thermonuclear explosion of a merger of a 1.2M$_\odot$ and a 1.0M$_\odot$ white dwarf. Color-coded is the logarithm of the density. The white cross in the upper left panel shows the point where the detonation is ignited. The white contours show the position of the detonation front.

The detonation starts at the surface of the primary white dwarf. As the primary has a larger density on average than the secondary white dwarf, the detonation moves faster there. In addition the primary is much smaller. Thus, the detonation flame completely burns the primary white dwarf before it starts to burn any part of the secondary white dwarf worth

mentioning. So, after one second the ashes of the primary white dwarf start to expand while the secondary is still mostly unburned. While the ashes expand, their density decreases and the remaining parts of the secondary white dwarf become the densest part of the object. At the same time, an asymmetry arises as the secondary blocks the expansion of the ashes at one side and they float around it. Finally, after two seconds also the secondary white dwarf has been burned completely. At that time the center of the object is dominated by material of the secondary white dwarf, as the ashes of the primary already expanded significantly.

In homologous expansion the ejecta reach an asymptotic kinetic energy of $2 \cdot 10^{51}$erg, which is about 1.5 times the kinetic energy of the standard W7 model, which models the explosion of a Chandrasekhar-mass white dwarf. The total mass of the ejecta adds up to $2.16 M_\odot$ or 1.6 Chandrasekhar masses. Thus, the average velocity of the ejecta is comparable or slightly lower the average velocity of normal Chandrasekhar mass explosion models.

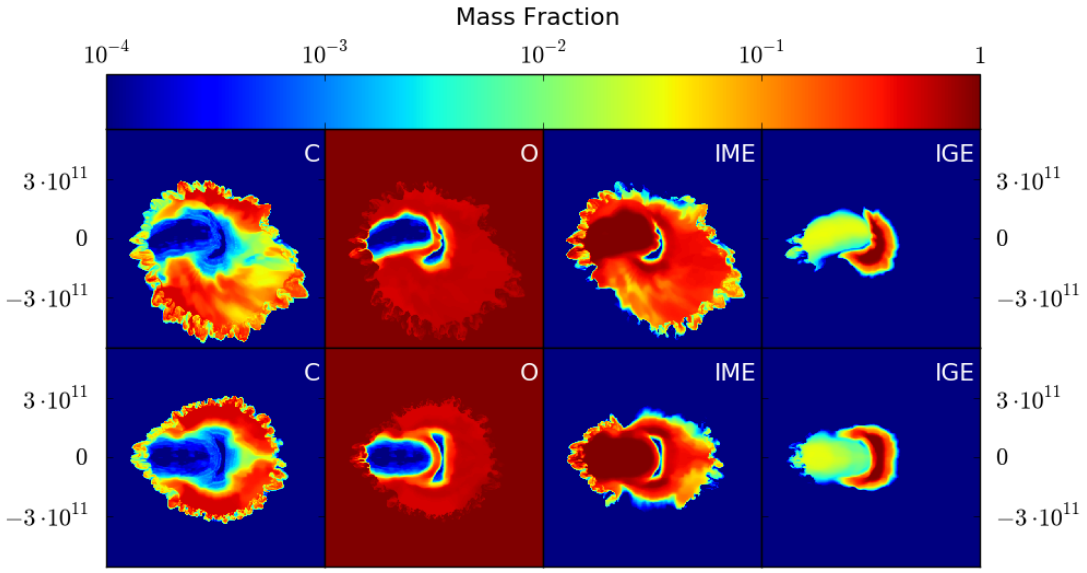

Figure 3.22: Final composition of the ejecta in homologous expansion 100s after the explosion. The panels show from the left to the right the abundances of carbon, oxygen, intermediate mass elements and iron group elements. The upper and lower panels show the system viewed face-on and edge-on respectively.

The explosion synthesizes $0.87 M_\odot$ of intermediate mass elements and $0.98 M_\odot$ of iron group elements. Less than $0.1 M_\odot$ of carbon and $0.3 M_\odot$ of oxygen are left unburned. The spatial distribution of the elements in the expanding ejecta are shown in Figure 3.22. The overall geometry of the ejecta is far from being spherical (compare with the final density distribution of the ejecta, shown in Figure 3.21). The primary white dwarf synthesized

dominantly iron group elements and only a very small fraction of intermediate mass elements. Owing to dynamic effects during the burning of the secondary white dwarf as described above, the distribution of iron group elements is peculiar. The very center of the object contains intermediate mass elements that were synthesized when the secondary white dwarf was burned. The iron group elements form a sphere around the center that is open to one side, the side where the secondary white dwarf was located. In contrast to the primary white dwarf, the secondary white dwarf produced mainly intermediate mass elements. Iron group elements are only produced at a mass fraction below 10%.

Isotope	Mass	Isotope	Mass
^{4}He	$3.8\,10^{-3}$	^{40}Ca	$1.3\,10^{-2}$
^{12}C	$5.7\,10^{-2}$	^{44}Ti	$8.5\,10^{-6}$
^{16}O	$4.4\,10^{-1}$	^{48}Cr	$2.2\,10^{-4}$
^{20}Ne	$2.9\,10^{-2}$	^{52}Fe	$4.7\,10^{-3}$
^{23}Na	$1.5\,10^{-4}$	^{54}Fe	$1.1\,10^{-5}$
^{24}Mg	$1.4\,10^{-1}$	^{55}Co	$7.4\,10^{-5}$
^{27}Al	$5.6\,10^{-4}$	^{57}Co	$1.1\,10^{-5}$
^{28}Si	$3.9\,10^{-1}$	^{56}Ni	$9.5\,10^{-1}$
^{29}Si	$2.9\,10^{-4}$	^{57}Ni	$1.1\,10^{-2}$
^{30}Si	$1.0\,10^{-4}$	^{58}Ni	$4.2\,10^{-3}$
^{31}P	$1.9\,10^{-4}$	^{59}Ni	$8.4\,10^{-4}$
^{32}S	$1.0\,10^{-1}$	^{60}Ni	$1.5\,10^{-3}$
^{33}S	$1.0\,10^{-4}$	^{60}Cu	$2.0\,10^{-3}$
^{36}Ar	$1.5\,10^{-2}$	^{60}Zn	$1.9\,10^{-3}$

Table 3.4: Final composition of the ejecta of a merger of a $1.2M_{\odot}$ and a $1.0M_{\odot}$ white dwarf. Shown are the total masses (in units of $M_{\odot}$) of the most abundant isotopes from detailed nucleosynthesis. An initial pure carbon/oxygen composition was assumed.

In a post-processing step, we reconstruct the detailed isotopic abundances of the ejecta using the trajectories of 150000 tracer particles, that were advected with the flow while the explosion took place. Table 3.4 shows the most abundant isotopes. The abundances are in good agreement with the results obtained in the hydrodynamical explosion simulation. Throughout the explosion the electron fraction stays more or less the same, as the densities at which the material is burned are too low for electron captures to play a role. As we use white dwarfs of zero metallicity (i.e. $y_e = 0.5$) the iron group elements are dominated by ^{56}Ni. Only negligible amounts of stable iron are produced. The iron group elements are produced almost only in the burning of the primary white dwarf, because the central density of the secondary white dwarf has already dropped significantly at the time it is burned, since it was disrupted in the merger. As expected for $y_e = 0.5$, the intermediate mass elements are dominated by alpha-elements (^{24}Mg, ^{28}Si, ^{32}S).

3.7.3 Comparison with Observations

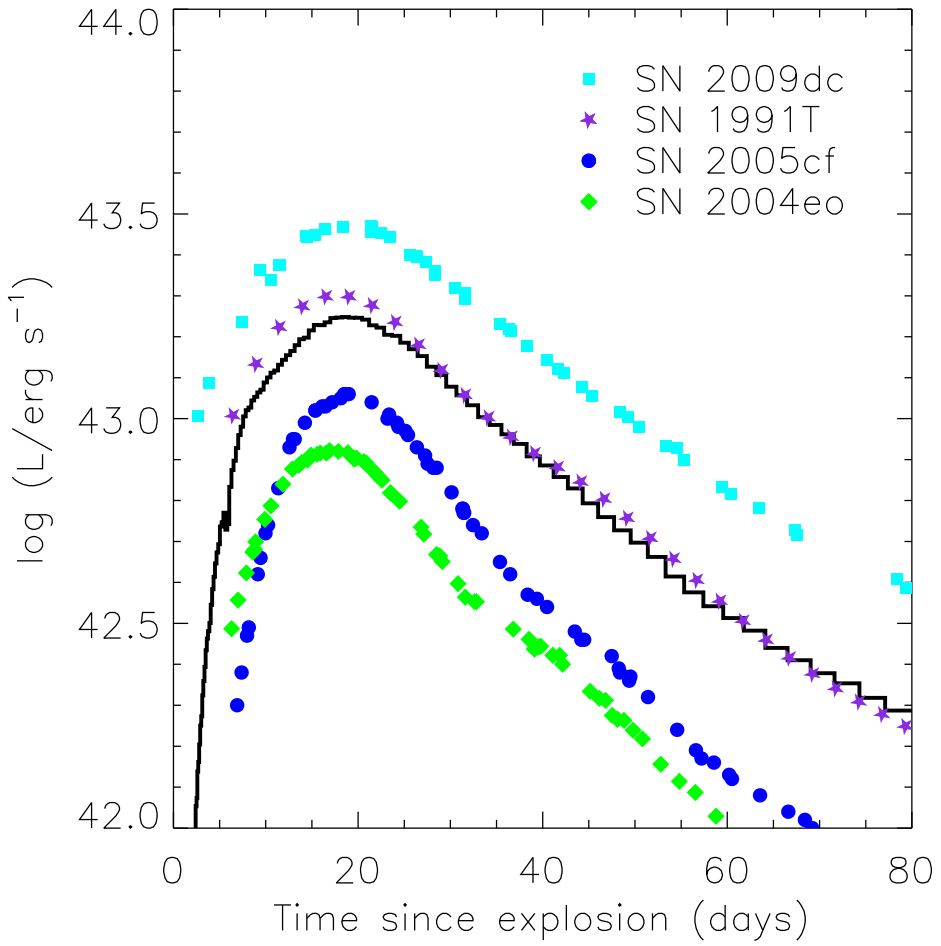

Figure 3.23: Bolometric light curve of the merger of two, 1.2$M_\odot$ and 1.0$M_\odot$, carbon/oxygen white dwarfs. The black line shows the synthetic bolometric lightcurve calculated from the model via 3D radiative transfer. Symbols show observed bolometric (sum over UBVRI bands) luminosity for four different type Ia supernovae. Light blue symbols show the superluminous SN 2009dc (Taubenberger, 2010). For comparison the light curves of the bright supernova SN 1991T (Phillips et al., 1992), the normal type Ia supernova SN 2005cf (Pastorello et al., 2007b) and SN 2004eo (Pastorello et al., 2007a) which represents the faint end of normal type Ia supernovae are also shown. (courtesy: M. Kromer)

The total mass of this merging system is enough to explain the ejecta masses found for superluminous type Ia supernovae. It is, however, not bright enough. With a ^{56}Ni mass of about one solar mass it is brighter than most of the normal type Ia supernovae, but clearly not luminous enough to explain the lightcurves of superluminous type Ia supernovae. This is illustrated very well in Figure 3.23. The light curve of the model agrees well with SN 1991T, which is expected, as modeling the light curve of SN 1991T leads to an estimate of the ^{56}Ni

mass of around one solar mass (Mazzali et al., 1995). The light curve of the superluminous object SN 2009dc, however, is considerably broader and more luminous, indicating that significantly more ^{56}Ni is necessary to power it.

Since the maximum mass at which carbon/oxygen white dwarfs are born is around $1.2M_{\odot}$, a binary system of more than $2M_{\odot}$ requires a high mass ratio, at which mass transfer is unstable. Since the merger is very violent, also for mass ratios smaller than one, it seems very unlikely that the formation of a detonation during the merger can be avoided. Thus, if these systems exist, they will explode during the merger, rather than form a very massive single white dwarf that is differentially rotating and has a high central density. Therefore, it seems that mergers of carbon/oxygen white dwarfs can be excluded as candidates for the scenario proposed by Howell et al. (2006).

It is possible that mergers of a massive carbon/oxygen white dwarf with an even more massive oxygen/neon white dwarf may be bright enough to explain superluminous type Ia supernovae. Such systems, however, will detonate less likely, as on the surface of the primary (oxygen/neon) white dwarf an oxygen or neon detonation has to form rather than a carbon detonation. They also release less energy when their material is burned to the same nucleosynthesis products than carbon/oxygen white dwarfs. Thus they may, provide a natural explanation for the very low expansion velocities of the ejecta of superluminous type Ia supernovae, which show some of the lowest expansion velocities ever observed for type Ia supernovae. A merger of two oxygen/neon white dwarfs, however, can be excluded, as some spectra of superluminous type Ia supernovae (e.g. SN 2009dc Yamanaka et al., 2009) show carbon lines.

Using spectropolarimetry Tanaka et al. (2010) find that SN 2009dc shows virtually no continuum polarization and only moderate line polarization. They interpret it such, that the lack of continuum polarization shows that overall geometry of the ejecta is spherically symmetric. The line polarization of the Si*II* and the Ca*II* lines is explained as a sign of the clumpy structure of the intermediate mass elements in the ejecta. Both properties seem to be not incompatible with a merger of two massive white dwarfs, but detailed radiative transfer studies to clarify this. The lack of continuum polarization may, however, be problematic to explain in this scenario, as the central ^{56}Ni core is not spherical.

In general, it is quite unclear, how frequent mergers of two massive ($M_{WD} > 1.0M_{\odot}$) really are. There are no observations of such systems yet and population synthesis studies carry huge uncertainties. However, as far as these studies can tell, such system should exist and merge in a reasonable timespan. In this case they should either look like known objects (very luminous type Ia supernovae) or be rare enough that we never had a chance to see one. Otherwise there will be a problem with the dynamic merger scenario as a whole, as they obviously do not explode for some reason.

3.8 Summary of the Dynamic Merger Model

In this Chapter, we explored mergers of carbon/oxygen white dwarfs with a mass ratio close to unity over a large range of masses. The masses of the primary, more massive white dwarfs range from $0.8M_\odot$ to $1.2M_\odot$. The general behavior of all these mergers shows many similarities. As the white dwarfs come close to each other, one of them is disrupted (in case of a mass ratio smaller than unity always the less massive white dwarf) and its material is accreted violently onto the remaining white dwarf. In this process, in all mergers we discussed with a primary mass larger than $0.9M_\odot$ and a mass ratio larger than 0.9 hot spots emerge at the surface of the remaining white dwarf that provide the conditions for a detonation to form there. Only for the merger of two $0.8M_\odot$ white dwarfs a detonation seems rather unlikely.

The subsequent thermonuclear explosions synthesize between $10^{-2}M_\odot$ and $1.0M_\odot$ of ^{56}Ni. Except for a small number of superluminous events, this covers the whole range of observed supernovae that are associated with thermonuclear explosions. A detailed study of the merger of two $0.9M_\odot$ white dwarfs revealed that it excellently reproduces objects of the hitherto theoretically unexplained subclass of 1991bg-like type Ia supernovae. For the other mergers, detailed radiative transfer studies applied on the outcome of the supernova explosion have yet to be done, to be able to compare them quantitatively with observational data.

Whereas mergers as studied here seem to provide a good explanation for the subclass of 1991bg-like objects, it seems unlikely that they contribute a significant fraction of brighter type Ia supernovae. However, they may be frequent enough for several objects to be found in upcoming surveys that attempt to increase the total number of known type Ia supernovae considerably. We also show that in contradiction to previous speculations (e.g. Howell et al., 2006), mergers of carbon/oxygen white dwarfs are not able to explain superluminous events. There is, however, still the possibility that these objects originate from a merger of a massive carbon/oxygen white dwarf with an oxygen/neon white dwarf, that needs to be tested.

4

The impact of type Ia supernova ejecta on their companions

As discussed in section 2.2.1, the progenitors of type Ia supernovae are still unknown. Observationally, it is hard to distinguish between the progenitor scenarios. One fundamental difference between the scenarios, however, is the presence of hydrogen. In the double degenerate scenario it is intrinsically absent, as it assumes a merger of two carbon/oxygen white dwarfs. In contrast, in the typical single degenerate scenario, hydrogen is the main constituent of the companion. An exception are helium-accretors in which a more evolved companion star has lost his hydrogen envelope. Thus, the WD accretes helium instead of hydrogen and hydrogen is missing in the system. Kato & Hachisu (2003) reported a possible detection of such an object. In the standard scenario, however, the companion star features a hydrogen envelope; and at least some part of it is expected to be carried away by the SN Ia ejecta impacting the companion. This, in principle, causes a problem for the single-degenerate scenario, because the astronomical classification of SNe Ia rests on the absence of hydrogen features in the spectra of these events. The hydrogen stripped off from the companion will have rather low velocities. It may thus be detectable in nebular spectra, if abundant enough. For the single-degenerate scenario it is therefore of critical importance that the mass of stripped material is sufficiently low to be still consistent with the observations.

4.1 Observational and theoretical constraints

There have been a few attempts to search for hydrogen in nebular spectra of type Ia supernovae. Mattila et al. (2005) studied nebular spectra of SN 2001el. From modeling them, they derived an upper limit of $0.03\,M_\odot$ of solar abundance material at velocities lower than $1000\,km\,s^{-1}$. Recently, Leonard (2007) studied nebular spectra of SN 2005am and SN 2005cf.

Based on the same model as Mattila et al. (2005), he estimated $\lesssim 0.01\,M_\odot$ of hydrogen-rich material in the ejecta of both objects. In addition, hydrogen has been detected indirectly by Patat et al. (2007) in circumstellar material of SN 2006X.

An alternative to this approach of observationally constraining the nature of the progenitor system is to directly search for the former companion star of the single-degenerate scenario in the remnants of historical galactic SNe Ia. Such a search has been carried out in the remnant of Tycho Brahe's supernova of 1572 by Ruiz-Lapuente et al. (2004), who claimed the identification of the binary companion. The star in question is a slightly evolved solar-type star, that moves with a radial velocity of $-108\,\mathrm{km\,s^{-1}}$ relative to the sun. It also has an atypical large tangential velocity of about $90\,\mathrm{km\,s^{-1}}$. A significantly larger velocity of the star compared to neighbours is expected as a result of the broken up binary orbit. Other stars observed in the same area with similar distances move only with average radial velocities of about -20 to $-40\,\mathrm{km\,s^{-1}}$, with a velocity dispersion of about $20\,\mathrm{km\,s^{-1}}$.

On the theory side, Marietta et al. (2000) presented two-dimensional hydrodynamical simulations of the impact of type Ia supernovae on their companions. They found that $0.15\,M_\odot$ were stripped from a Roche-lobe filling main-sequence companion. This would rule out a main-sequence plus white dwarf (MS+WD) system for the type Ia supernovae analyzed by Leonard (2007), if it was representative. Recently, Meng et al. (2007) pointed out that considering the effect of the mass transfer phase on the companion star may change the result significantly. They studied the impact of SNe Ia on different companion stars analytically. In contrast to Marietta et al. (2000), who assumed the structure of single main-sequence stars for the companion, Meng et al. (2007) evolved it through the binary evolution phase before the explosion of the white dwarf. They found at least $0.035\,M_\odot$ of stripped hydrogen for the companion. However, this result is only a lower limit, since they did not include mass loss by vaporization from the hot surface of the star. Thus, taken at face value, the currently available theoretical studies constitute a strong case against MS+WD progenitor systems for type Ia supernovae.

The aim of the following chapters is to check and update the Marietta et al. (2000) calculations with the results of recent detailed binary evolution models. Ivanova & Taam (2004) identified possible type Ia supernova progenitors from a parameter study of MS+WD binary evolution. Their results are in agreement with other studies in this field (e.g. Langer et al., 2000; Han & Podsiadlowski, 2004). Based on these results, we explore the effect of the impact of a type Ia supernova on different MS companions by means of 3D hydrodynamical simulations. For the first time, our simulations include the effects of mass transfer on the structure of the envelope of the donor.

4.2 Modeling approach

Two different codes are employed in this work: one to construct the companion stars mimicking a binary evolution and the other to investigate the hydrodynamical impact of the supernova on the companion star.

To evolve the companion stars we use the stellar evolution code GARSTEC of Weiss & Schlattl (2007). It evolves stars with a given mass and metallicity to a certain age and is used

to construct a solar-type companion star similar to the "HCV" scenario of Marietta et al. (2000) (see Sect. 4.3). The code also allows to include mass loss during the evolution but does not account for a binary evolution. In our study of a variety of progenitor models (see Sect. 4.4), we therefore rely on the parameters of the binary evolution study by Ivanova & Taam (2004) to construct our companion stars. For each of the models we first set up a star that fits the parameters at the onset of the mass transfer phase. At this point, a constant mass loss rate is assumed and the stellar evolution is followed for the duration of the mass transfer period. The mass loss rate employed here corresponds to the mass loss rate of the original binary models of Ivanova & Taam (2004) averaged over the entire mass transfer phase. After following this phase, we obtain a stellar configuration that approximates the outcome of a realistic binary evolution. It is used to study the process of the interaction with the explosion ejecta once the binary WD undergoes a type Ia supernova.

The impact of the supernova ejecta is simulated using the same modified smoothed particle hydrodynamics (SPH) code GADGET (Springel, 2005) as for the merger simulations. In order to set up the companion star here, we map the one-dimensional profiles of density, internal energy, and nuclear composition of the stellar evolution calculation to a particle distribution suitable for the SPH code. The mapping procedure is described in section 5.1.6. Using GADGET, these companion stars were relaxed passively in a separate step for $1.0 \cdot 10^4$ s to get rid of numerical artifacts that may have been introduced by the transformation (e.g. due to the placement of the particles).

A supernova was added to the simulation at a distance given by the orbital period of the binary system before the explosion. The supernova was set up based on the W7 model by Nomoto et al. (1984). This one-dimensional model is well tested and provides a good fit to observations of standard type Ia supernovae. It has a kinetic energy of $1.23 \cdot 10^{51}$ erg. At the time we add the supernova model to the simulation, it has reached already the phase of homologous expansion. The impact of the supernova ejecta and the following evolution of the ejecta and the companion star are simulated for about one hour. After this time, the companion star is already relaxing and its mass and velocity have reached constant values.

The code setup we use is quite similar to the merger simulations. We also use particles of equal mass and use the smoothing length of the particles also for the gravitational softening. We neglect, however, nuclear reactions. The latter is justified since Marietta et al. (2000) showed that the additional energy generated by shock-wave induced hydrogen burning caused by the impact is a marginal effect. The savings in computing time due to this approximation, however, are substantial.

4.3 Tests of implementation

One of the obvious questions arising in our approach is whether the 3D SPH scheme applied here leads to the same results as the 2D grid-based approach of Marietta et al. (2000). This is tested by using the initial parameters of the HCV scenario of Marietta et al. (2000) in our setup. In the HCV scenario, the supernova is realized as a W7 model. The companion is a solar like 1.017 $M_\odot$ main sequence star with a central hydrogen abundance of 0.58. The separation between supernova and companion star at the time of the explosion is $2.04 \cdot 10^{11}$ cm.

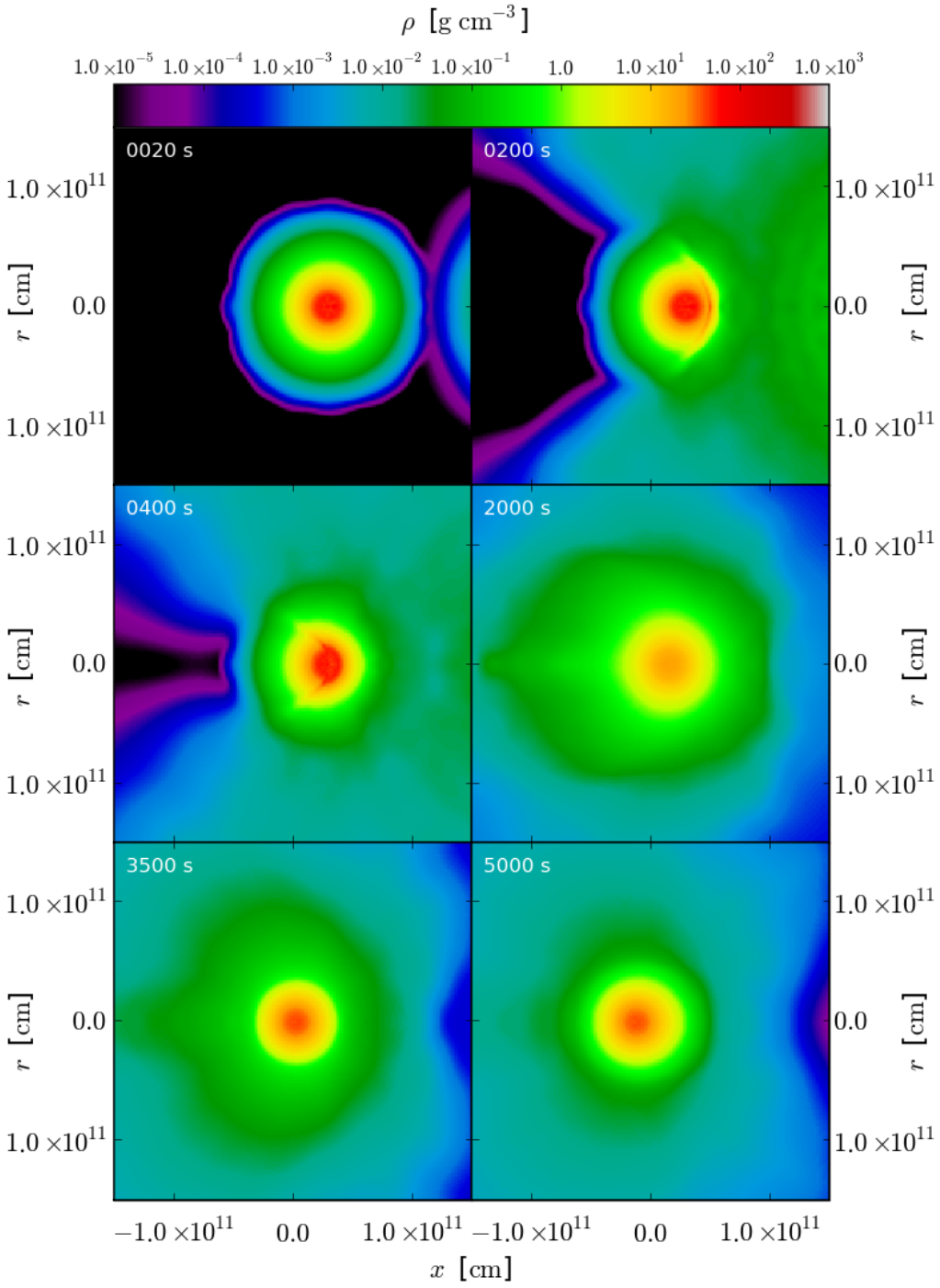

Figure 4.1: Snapshots of the evolution of the companion star in the HCV scenario. The plots use cylindrical coordinates. The radial coordinate is averaged over angle. Color-coded is the density.

Figure 4.1 shows the typical evolution of the companion star in our simulations. Here, an example with a total of 235499 SPH particles is illustrated starting out with the impact of the

outermost supernova ejecta on the companion and ending when they have passed the star and it relaxes again. The first image after 20 s shows the companion star at the instant when the first ejecta reach the companion from the right. In the second snapshot, taken after 200 s, the ejecta have hit the companion star. A shock wave forms and starts to propagate through it. Another 200 s later (third snapshot of Figure 4.1), the shock wave reaches the center of the star. In the fourth snapshot (~2000 s after the explosion) the shock wave has crossed the star completely. Material is ejected on its far side. The last two images show the star shrinking and relaxing again dynamically.

Qualitatively, this looks similar to the simulations of Marietta et al. (2000). However, our results do not show the hydrodynamical instabilities they observed at the interface of supernova ejecta and the stripped material in the wake of the star (note that some mixing of companion star material into the supernova ejecta is realized, see Figure 4.7). This difference is not surprising as SPH codes are known to suppress instabilities due to their large numerical viscosity (see, however, Fryer et al., 2007, showing that grid-based codes may under some circumstances not reproduce the mixing better than SPH codes). However, it is not a priori clear that this morphological difference significantly affects the effects and quantities we are interested in. The fundamental quantity upon which we base our comparison is the bound mass of the companion star, or, equivalently, the mass stripped away from it by the supernova ejecta.

As a first step, we perform a resolution study in order ensure a comparison with the Marietta et al. (2000) result based on a converged simulation. To test for numerical convergence we use different resolutions with $1.1 \cdot 10^5$ to $4.7 \cdot 10^6$ SPH particles (counted for the entire setup, i.e. supernova and companion star, as the total mass of the configuration is equally distributed on the particles).

Figure 4.2 shows the evolution of the mass loss from the companion star with time for different resolutions. This value is calculated by subtracting the sum over the masses of all particles that are gravitationally bound to the star from its initial mass. Whether or not a particle is bound to the star is decided by comparing its potential energy relative to the center of the star with the kinetic energy of its motion relative to the motion of the star. For this, the center and velocity of the star are taken from the previous snapshot. Then the current center and velocity of the star are calculated from all bound particles. In principle, the new position of the star's center should be used to recalculate which particles are bound to the star and this cycle should be iterated until convergence is reached. However, already the position and velocity of the star taken from the previous snapshot usually provide a sufficiently accurate approximation, and we thus avoid the iteration.

After ~3000 s the mass loss has stopped and the star has reached its final mass. There is a numerical artifact in the detection of the bound mass of the companion star around ~300 s after the explosion. For one snapshot the mass of the companion star seems to increase. This is due to a false detection of particles as unbound in the previous snapshot due to high radial velocities of particles, that point to the center of the star.

Table 4.1 lists some simulation properties for different resolutions after $2 \cdot 10^4$ s. Here, n_{star}, n_{tot}, and m_{particle} denote the number of particles the star is composed of, the total number of particles in the simulation, and the particle mass, respectively. The results of the simulations

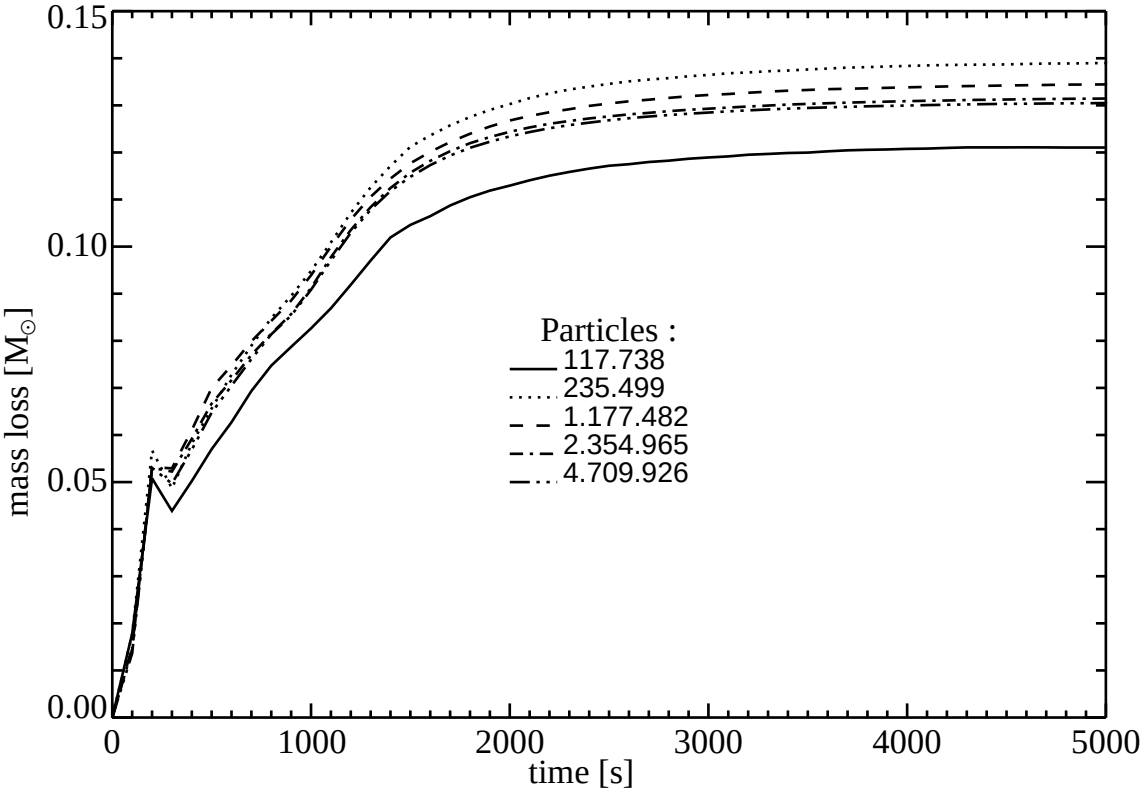

Figure 4.2: Mass loss of the companion star depending on the time after the supernova explosion for different resolutions.

are characterized by mass m_{stripped} stripped away from the companion star, its final mass m_{remnant}, and its velocity relative to the supernova v_{kick}.

Considering Table 4.1 and Figure 4.2, we conclude, that this simulation is numerically converged when using more than 10^6 particles. For the two simulations with 2.3 and 4.7 million particles, the graphs in Figure 4.2 are nearly identical. Note that the kick velocity converges slower than the stripped mass.

Numerical convergence, however, does not necessarily imply consistency with the physical solution. To check our results in this respect, we compare them to the results of Marietta et al. (2000). With the highest resolution of nearly 5 million particles the stripped mass after $2.0 \cdot 10^4$ s is $0.134\,M_\odot$. This is quite close to the result of $0.15\,M_\odot$ reported by Marietta et al. (2000).

As carried out here, however, the comparison is not yet based on exactly the same assumptions. Marietta et al. (2000) performed their simulations on a finite computational grid and therefore mass was lost over the domain boundaries. This mass was always assumed to be unbound from the companion star. We therefore recalculate the stripped mass in our simulations by assuming for comparison all particles to be unbound that are outside a cylindrical box equal to the simulation volume of Marietta et al. (2000). In this approach we find a stripped mass of $0.143\,M_\odot$ for our highest resolved simulation. This result is in excellent agreement with the $0.15\,M_\odot$ of stripped mass found by Marietta et al. (2000). Moreover,

n_{star}	n_{tot}	m_{particle} $[\mathrm{M}_\odot]$	m_{stripped} $[\mathrm{M}_\odot]$	m_{remnant} $[\mathrm{M}_\odot]$	v_{kick} $[\mathrm{km\,s^{-1}}]$
50000	117738	$2.03 \cdot 10^{-5}$	0.126	0.891	101.1
100000	235499	$1.02 \cdot 10^{-5}$	0.144	0.873	95.4
500000	1177482	$2.03 \cdot 10^{-6}$	0.138	0.879	85.3
1000000	2352965	$1.02 \cdot 10^{-6}$	0.135	0.882	80.3
2000000	4709926	$5.09 \cdot 10^{-7}$	0.134	0.884	81.6

Table 4.1: Resolution test

Model	$M_{\mathrm{c,i}}$ $[\mathrm{M}_\odot]$	$M_{\mathrm{c,f}}$ $[\mathrm{M}_\odot]$	Δt_{tr} [yr]	P_{f} [d]	a_{f} $[10^{11}\,\mathrm{cm}]$	M_{stripped} $(M_\odot)$	v_{kick} $[\mathrm{km\,s^{-1}}]$
rp3_28a	2.8	0.6	$7.7 \cdot 10^5$	1.7	5.21	0.032	52.8
rp3_20a	2.0	1.17	$3.9 \cdot 10^6$	0.55	2.68	0.032	46.6
rp3_20b	2.0	1.25	$2.0 \cdot 10^6$	1.08	4.26	0.0095	24.1
rp3_25a	2.5	1.37	$1.7 \cdot 10^6$	0.51	2.62	0.058	60.5
rp3_24a	2.4	1.4	$8.4 \cdot 10^5$	1.1	4.39	0.010	26.6
rp3_20c	2.0	1.46	$2.6 \cdot 10^6$	1.44	5.29	0.012	17.0

Table 4.2: Parameters of the progenitor models

the remnant star velocities at this time (85.7 $\mathrm{km\,s^{-1}}$ reported by Marietta et al., 2000, vs. our 81.4 $\mathrm{km\,s^{-1}}$) agree very well.

We therefore conclude that our SPH approach is capable of capturing the main dynamical effects of the supernova impact on the companion star. The global quantities of the Marietta et al. (2000) study are reproduced down to the percent level. The differences in the occurrence of hydrodynamic instabilities are obviously a minor effect with respect to the overall results such as the stripped mass and the velocity of the companion star caused by the kick by the supernova ejecta. The instabilities suppressed in our SPH approach may, however, enhance the mixing between supernova ejecta and stripped material from the companion in reality.

4.4 Parameter studies

Three major physical parameters of the progenitor system are expected to influence the dynamics of the supernova impact on the companion star: the kinetic energy of the supernova ejecta (powered by the thermonuclear burning in the explosion), the separation between supernova and companion, and the structure of the companion star at the time of the ex-

plosion.

In reality, of course, separation and companion structure are not independent, but result from the characteristics of the original binary system and its evolution through the mass transfer phase. Moreover, the dependence of the supernova explosion energy on other parameters is unknown and thus treated as an independent physical parameter in this study. In any system with Roch-lobe overflow, the solid angle under which the companion star is seen from the white dwarf depends only on the mass ratio of its components. However, in order to determine how changing the distance affects the results it is treated here as an independent parameter. This is motivated partially by the possibility that the WD and the companion star disconnect shortly before the explosion, as suggested by Patat et al. (2007) for SN 2006X.

Our main emphasis, however, will be on the structure of the companion star. In order to model the progenitor systems, we take parameters from the study of Ivanova & Taam (2004) and a typical Population I metallicity of 0.02 for all stars. Ivanova & Taam (2004) analyzed the evolution of possible type Ia supernova progenitor systems consisting of a WD and an evolved MS star. Detailed calculations of 65 different systems were carried out, varying the initial mass of both objects and the initial distance to cover the parameter space. From the resulting sample, they pick six representative models which are believed to be likely to evolve into a type Ia supernova. These are the systems we select for our study. Their properties are listed in table 4.2. In addition, characteristics of the companion star after interaction with the supernova ejecta are given.

Values taken from Ivanova & Taam (2004) are: masses of the companion star at the beginning of the mass transfer $M_{\mathrm{d,i}}$ and at the time of the explosion $M_{\mathrm{d,f}}$, length of the mass transfer period Δt_{tr}, orbital period P_{f}, distance between white dwarf and its companion star just before the explosion a_{f}.

Results of the simulations are: mass stripped from the companion M_{stripped} and its kick velocity v_{kick}, 5000 s after the explosion.

The three parameters of the progenitor system are individually discussed in the following paragraphs. While the simulations testing the effects of the explosion energy and the binary separation were carried out with $2{\cdot}10^5$ particles in the companion star, the study based on the realistic progenitor system structure was set up with $2 \cdot 10^6$ and $4 \cdot 10^6$ particles representing the companion. Therewith, the mass of the single particles and, as all particles had the same mass by construction, the number of particles representing the supernova explosion were fixed.

4.4.1 Explosion energy

The influence of the supernova explosion energy on the interaction with the companion is studied on the basis of model rp3_20a. All parameters but the supernova energy were kept constant with the values of the original model (see Table 4.2).

The kinetic energy of the supernova was varied in the range $0.8 \ldots 1.6\,\mathrm{B}$ ($= 0.8 \ldots 1.6 \cdot 10^{51}$ erg). The lower limit corresponds to lowest kinetic energies of simulated deflagration SNe Ia. The upper limit is the maximum energy a SN Ia can have, assuming that a Chandrasekhar-mass WD consisting of an equal-by-mass mixture of C and O burns com-

pletely to ^{56}Ni. The kinetic energy of the supernova ejecta $E'_{kin,SN}$ was adjusted by scaling the velocities $\vec{v}'$ of the supernova particles (originally representing the W7 model with $E^{W7}_{kin,SN}$ and $\vec{v}^{W7}$) according to

$$\vec{v}' = \sqrt{\frac{E'_{kin,SN}}{E^{W7}_{kin,SN}}} \cdot \vec{v}^{W7}. \tag{4.1}$$

This scaling preserves the homologous expansion ($v \propto r$) of the ejecta.

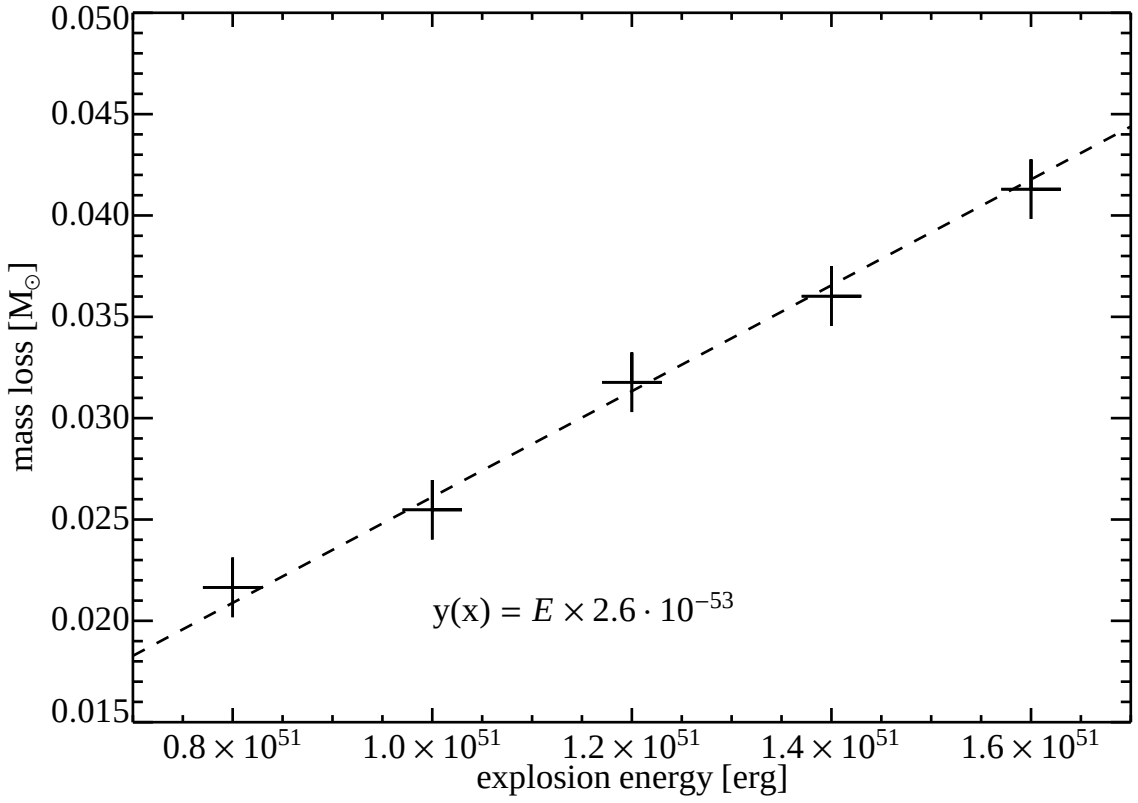

Figure 4.3: Stripped mass for different supernova energies in model rp3_20a. The dashed line corresponds to the fit shown in the plot.

The stripped mass as a function of the supernova energy is shown in Figure 4.3. The relation is linear in good approximation and can be fitted by

$$M_{\text{stripped}} = 2.6 \cdot 10^{-2} \frac{E_{\text{kin,SN}}}{10^{51}\text{erg}} \, \text{M}_\odot, \tag{4.2}$$

assuming that the offset is zero (without this constraint the offset is only $1.3 \cdot 10^{-3}$). We emphasize that, although the functional form of the relation may be generic, the particular parameters of the fit apply to model rp3_20a only. For different companion structures, for instance, the values of the parameters are expected to change. This should be kept in mind for the fits presented below as well.

Note that the studied energy range covers only a factor of 2 and therefore the stripped mass also changes only by a factor of 2. The energy of the W7 model of $1.23 \cdot 10^{51}$ erg corresponds to

an intermediate case. These results indicate that changes in the supernova energy have only a small effect on the stripped mass as compared to the other parameters discussed below. The kick velocity can be fitted by a power law as

$$v_{\mathrm{kick}} = 2.8 \cdot 10^6 \left(\frac{E_{\mathrm{kin,SN}}}{10^{51}\mathrm{erg}} \right)^{0.55} \mathrm{cm\,s^{-1}}. \tag{4.3}$$

A simple argument for this behavior may be that velocity of the companion is mainly given by the momentum exchange from the supernova ejecta that hit the star. As the velocity of the ejecta increases with the square root of the kinetic energy, the velocity of the star should increase accordingly. The exponent in eq. (4.3) is only slightly larger than 1/2 and thus this simple picture captures the process rather well.

4.4.2 Distance

In order to test the influence of the separation, we again choose model rp3_20a (see Table 4.2 for the parameters). Here, the distance d between WD and companion was varied in the range of $1.5 \ldots 3 \cdot 10^{11}$ cm. All other parameters were kept constant. The relation between distance and stripped mass for this model is shown in Figure 4.4. From the largest to the smallest distance the stripped mass increases by a factor of ten. The relation follows a power law in good approximation and can be fitted to

$$M_{\mathrm{stripped}} = 0.08 \cdot \left(\frac{d}{2 \cdot 10^{11}\mathrm{cm}} \right)^{-3.49} \mathrm{M_\odot}. \tag{4.4}$$

The kick velocity depending on the separation d also follows a power law. It is approximately given by

$$v_{\mathrm{kick}} = 1.0 \cdot 10^7 \left(\frac{d}{2 \cdot 10^{11}\mathrm{cm}} \right)^{-1.45} \mathrm{cm\,s^{-1}}. \tag{4.5}$$

The fraction of the supernova ejecta that hits the star scales with the inverse square of the distance treated as an independent parameter as discussed above. Remembering that the stripped mass seems to scale linearly with the explosion energy, one may expect a geometrical scaling as $M_{\mathrm{stripped}} \propto d^{-2}$. This does clearly not fit our results. It indicates that the connection is more complex, and the linear correlation between explosion energy and stripped mass is possibly only a result of the small energy range tested. In addition the simple scaling neglects that the companion star is not a flat disc but a sphere. The whole process also seems to depend on the time evolution of the density of the ejecta hitting the star.

4.4.3 Companion star

Table 4.2 shows the stripped masses and the kick velocities of the remnants for the six different progenitor systems suggested by Ivanova & Taam (2004). The supernova model used in all models is the original W7 model with a total kinetic energy of $1.23 \cdot 10^{51}$ erg. The variations in the stripped mass between the $2 \cdot 10^6$ particles and the $4 \cdot 10^6$ particles simulations were less than a few percent indicating numerically converged results.

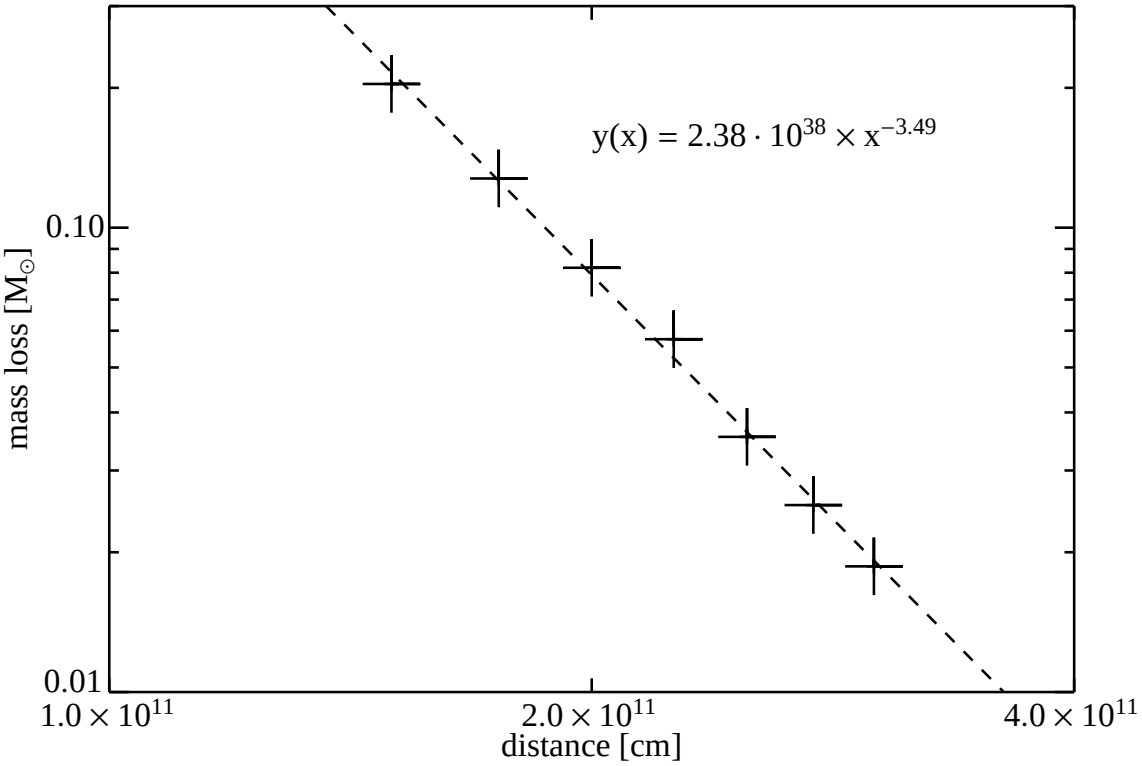

Figure 4.4: Stripped mass versus binary separation for model rp3_20a.

The stripped masses range from $0.01\,M_\odot$ to $0.06\,M_\odot$ for the different setups. This is significantly less than previous results reported by other authors (Marietta et al., 2000; Meng et al., 2007). Compared to the $0.15\,M_\odot$ result of Marietta et al. (2000) we find a factor of 3–15 less stripped material.

This deviation is attributed to the binary evolution of the progenitor we take into account in the present study. The binary evolution significantly affects the properties of both the companion star and the geometry of the binary configuration.

The main effect on the companion star is illustrated in Figure 4.5, where the density profile of the companion star in model rp3_20a at the time of the explosion is plotted in comparison with the density profile of a star in thermal equilibrium that was evolved as a single object to the same mass and nuclear age. The equilibrium star features a much larger radius than the binary companion. This is a result of the mass transfer phase in the binary system, that removes the outer layers and leads to a more compact star. The mass loss occurs rather rapidly: the duration of the mass transfer phase is about a factor of ten less than the Kelvin-Helmholtz timescale of the stars in our models. Therefore, the star is not able to adjust its structure to the loss of the outer layers and it shrinks into a more compact object. Finding less stripped mass when taking into account the modification of the companion structure due to the binary evolution is thus not surprising.

In order to corroborate this interpretation, we set up model rp3_20a with a companion structure that corresponds to that of a star of equal mass in thermal equilibrium. In this model, $0.066\,M_\odot$ are stripped from the companion by the supernova. This is a factor of 2

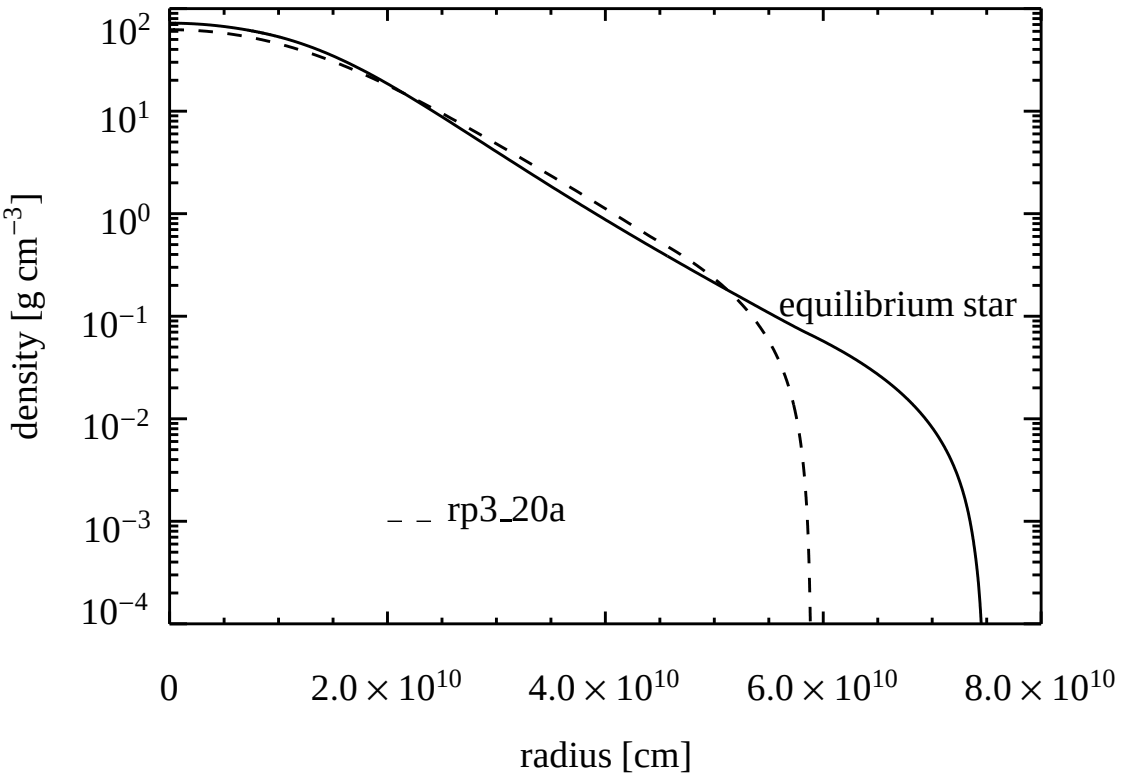

Figure 4.5: Comparison of density profiles of the companion star in model rp3_20a at the time of the explosion and a single star with the same mass and nuclear age.

more than for the original rp3_20a model. The difference can be explained by the larger, less bound envelope of the equilibrium star that can be stripped away more easily. Moreover, the larger radius causes an extended interaction area that also leads to a slightly larger kick velocity of 51.2 km s^{-1} for the equilibrium companion star model evolved in isolation as compared to the 46.6 km s^{-1} of the binary star companion model.

Additionally, in the model we use the companion star is slightly more massive (1.17 $M_\odot$ at the time of the explosion) than the solar mass companion star of Marietta et al. (2000). This leads to a slightly larger radius of the equilibrium star companion and therewith a larger separation distance and a decreased stripped mass.

These effects together explain the significant difference between our results and the previous work of Marietta et al. (2000), who used a companion with the structure of an isolated equilibrium star. We note, however, that our interpretation is not in agreement with the work of Meng et al. (2007), who found a lower limit on the stripped mass of 0.035 $M_\odot$ taking into account binary evolution. This is probably due to oversimplifying assumptions they made in their analytical treatment of the ejecta-companion star interaction.

The kick velocities of the companion star after the impact of the supernova ejecta we find in our models vary from 17 km s^{-1} to 61 km s^{-1} (see Table 4.2). The velocities roughly increase with the size of the companion stars (as the cross section increases) and decrease

with larger separation distances (as the transferred momentum decreases) and masses (for the same transferred momentum) of the companion stars.

4.5 Observational implications

Observations that may help to constrain the nature of the SN Ia progenitor systems are the detection of hydrogen in the spectra of these events, signatures in the spectropolarimetry data due to an asymmetric morphology of the ejecta as a result of the interaction with the companion star, and a direct observation of companions in supernova remnants. We discuss these possibilities in the light of the presented study.

4.5.1 Hydrogen detection in SN Ia spectra

Our results are consistent with the constraints on hydrogen in the ejecta as given by Leonard (2007) and Mattila et al. (2005). However, none of our models has stripped hydrogen mass far below the upper limit of Leonard (2007) of $0.01\,M_\odot$. As these limits result from a non-detection of hydrogen in nebular spectra, our simulations predict hydrogen detection not far below these values. Conclusions on the validity of the single-degenerate scenario depend on whether the systems studied here are representative for Chandrasekhar mass WD+MS SN Ia progenitors and whether the observed events fall into this class. If both were true, lowering the observational upper limits of hydrogen in the ejecta of SNe Ia by another order of magnitude would exclude this progenitor scenario.

Yet it is important to note that a quite simple model was employed by Leonard (2007) and Mattila et al. (2005) to constrain limits on the hydrogen mass from the observations. A more rigorous approach would be to use the results of hydrodynamical simulations such as presented here as an input for full radiative transport calculations. From these calculations it will be possible to predict whether hydrogen lines should be visible in the spectra and how strong they should be at a given epoch.

4.5.2 Hole in the ejecta

The supernova ejecta do not only affect the companion star, but are also affected themselves by the impact. Figure 4.6 shows the material after the impact. The left column shows both the supernova ejecta and the companion star material including the hydrogen stripped from the star. The right column shows only the material that was part of the supernova ejecta at the beginning of the simulation.

The supernova ejecta that were spherically symmetric in the beginning are clearly asymmetric after the impact. In the wake of the companion star, a cone-like hole in the supernova ejecta is visible. To some degree it is filled with material that is ejected from the companion star. At the borders of this hole, the supernova ejecta are slightly denser, because the material missing in the hole was transfered there. The opening angle of the cone-like hole is about 45° (see the top row of Figure 4.6 showing the ejecta 1000 s after the explosion). This result is consistent with the findings of Marietta et al. (2000). However, the area in which the supernova ejecta are affected by the impact on the companion star is as large as 90° (see

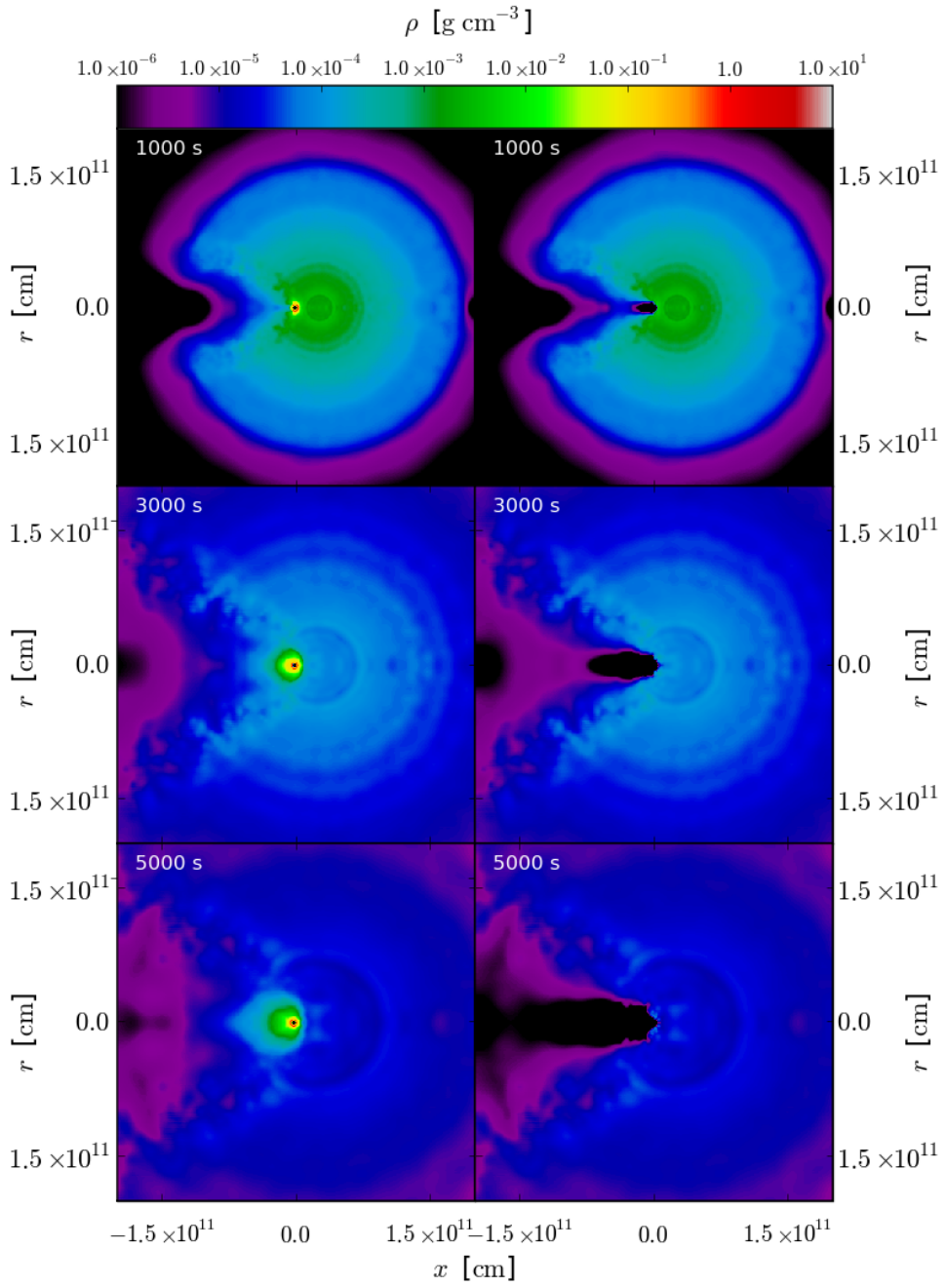

Figure 4.6: Snapshots of the evolution of the supernova ejecta in the rp3_20a scenario. The left column shows supernova ejecta and the companion star. In the right column all material of the companion is cut out, leaving only the supernova material. The plots use cylindrical coordinates. The radial coordinate is averaged over angle. Color-coded is the density.

middle and the lower row of Figure 4.6 showing the density of supernova ejecta after 3000 s and 5000 s).

A more detailed view of how the supernova ejecta are mixed with the material stripped from the companion star is given in figure 4.7. It shows for the same setup the relative

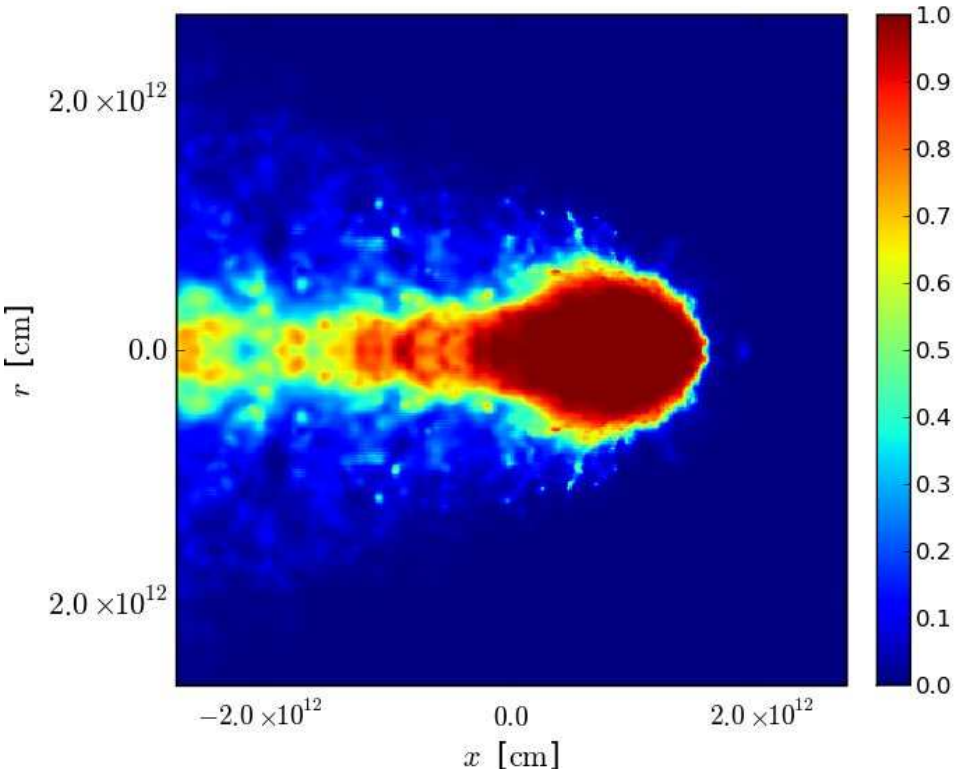

Figure 4.7: Snapshot of simulation rp3_20a taken 5000 s after the explosion. Color-coded is the of the relative amount of material originally belonging to the companion star (red) with respect to the total material (blue corresponds to supernova material). Cylindrical coordinates with the radial coordinate averaged over angle are used.

amount of material that originally belonged to the companion star with respect to the total amount of material.

Qualitatively, the structure of the ejecta resembles the simple model used by Kasen et al. (2004) to explore the effect of a hole in the ejecta on spectra and luminosity of type Ia supernovae. With it he was able to reproduce observed spectropolarimetry observations of type Ia supernovae.

4.5.3 Identifying companion stars in supernova remnants

The remaining companion star should have a different velocity than its surrounding stars. This velocity is determined by the orbital velocity of the star at the moment the white dwarf explodes and of the kick it gets from the impact of the supernova ejecta. The former is perpendicular to the connecting line between the white dwarf and the companion star. For our models it ranges between 130 km s^{-1} (rp3_20c) and 380 km s^{-1} (rp3_28a). The latter velocity is a result of the impact of the ejecta and is therefore aligned with the connecting line. In our simulations it reaches values from 17km s^{-1} to 50 km s^{-1}. Therefore, the orbital velocity clearly dominates the velocity of the companion star relative to the center of the supernova remnants. The velocity of the star Tycho G which was identified as progenitor of Tycho

Brahe's supernova by Ruiz-Lapuente et al. (2004) features a modulus of its spatial velocity of 136 km s^{-1}. It thus falls into the lowest part of the range we find in our simulations. The properties of Tycho G are thus consistent with the predictions of our models. It, however, does not rotate fast (Kerzendorf et al., 2009), which would be expected as a result of tidal locking in the close binary system with mass transfer. Thus, more work has to be done to really figure out whether it really is the remaining companion star of the white dwarf that exploded 400 years ago.

4.6 Massive main sequence companion stars

In the single degenerate scenario the white dwarf has to accrete several tenths of a solar mass to reach the Chandrasekhar mass. For stable hydrogen burning on the surface of the white dwarf, the accretion rate has to be in a small range around $10^{-7} - 10^{-6}\,M_\odot yr^{-1}$ (Nomoto, 1982; Nomoto et al., 2007). This leads to constraints on the mass ratio of the binary and therefore the mass of the companion star. Ruiter et al. (2009) find, that only white dwarfs with companions that have an initial zero age main sequence (ZAMS) mass between $0.7 - 2.7M_\odot$ reach the Chandrasekhar mass. More massive secondaries lead to higher accretion rates, unstable mass transfer and the formation of a common envelope rather than stable growth of the white dwarf. As shown recently by Ruiter et al. (2009), using these constraints their population synthesis simulations predict that the single degenerate scenario is not frequent enough by at least a factor of 10 to explain the observed type Ia supernova rates.

One possibility that may fix this problem has been proposed by Hachisu et al. (1999): A high mass transfer rate may lead to the formation of a strong, optically thick wind emerging from the white dwarf. This wind may be able to stabilize the mass transfer also for large mass ratios, therefore preventing the formation of a common envelope. This would allow stable mass transfer onto the white dwarfs from companion stars with initial masses as high as $6M_\odot$ (Hachisu et al., 2008) and increase the rates expected for the single degenerate scenario significantly. There is, however, a drawback in this scenario. As the companion is significantly more massive and has a much more extended envelope, it may be more susceptible to hydrogen being stripped by the impact of the supernova ejecta. To check whether this effect should have any observable consequences, we simulated the impact of a type Ia supernova on such a model. The detailed model was kindly provided by I. Hachisu. In this model, the secondary main sequence star had a initial zero age main sequence mass of $5M_\odot$. At the time the white dwarf reaches its Chandrasekhar mass, it has shrunk to $2.1M_\odot$. At this time, the orbital period of the binary system is 15h, equivalent to a separation of $3.2 \cdot 10^{11}$ cm. The setup was done the same way as described above, W7 was used again to model the supernova ejecta.

Figure 4.8 shows the impact of the supernova onto its massive companion. The behavior is similar to the models described above. The main difference is, that the companion star itself is significantly less affected by the shock originating from the impact. Mass stripping from the envelope, however, is more severe than for less massive companions. In this case, $0.1M_\odot$ of hydrogen-rich material is stripped from the surface of the companion star and

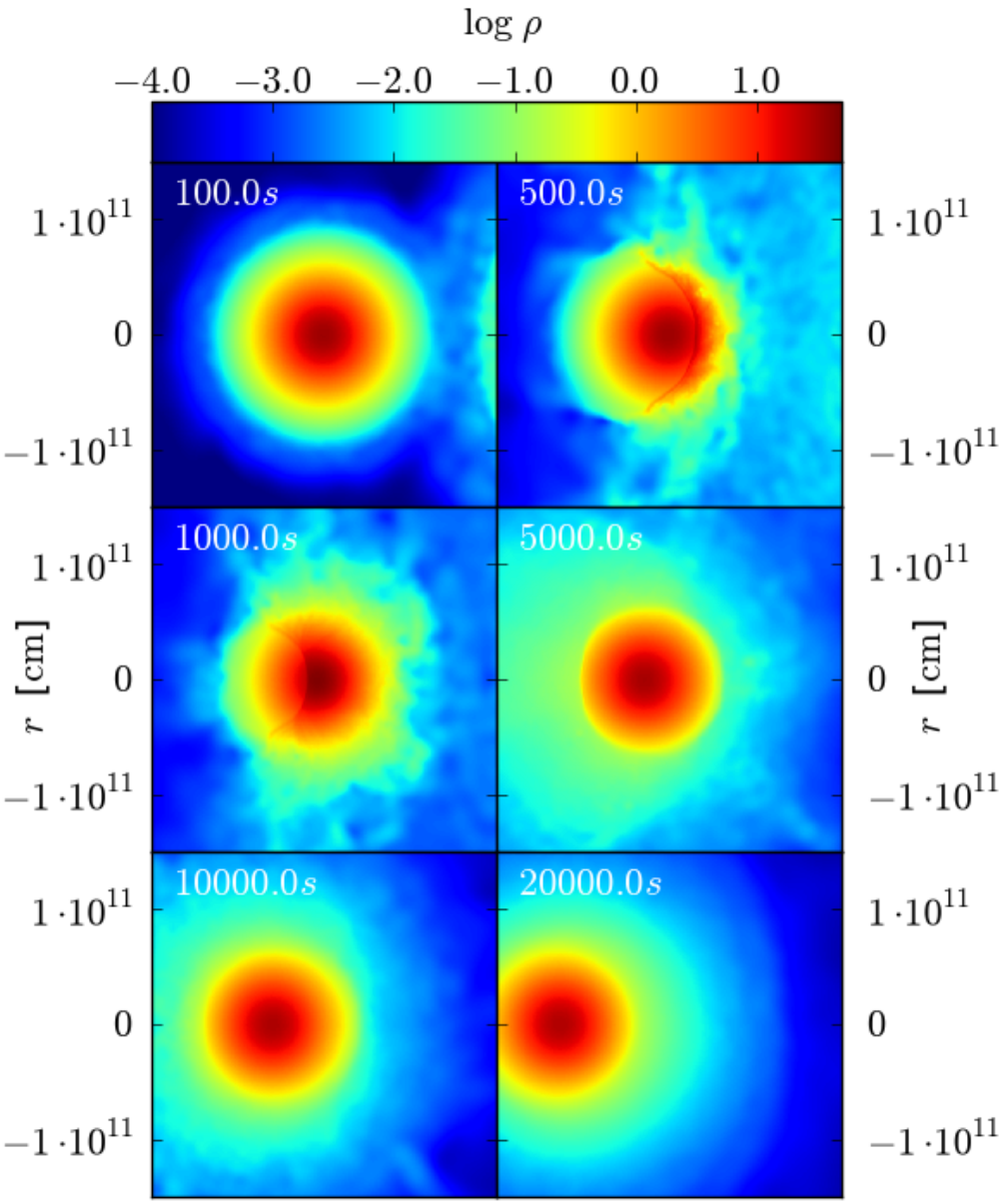

Figure 4.8: The impact of the ejecta of a type Ia supernova on a massive main sequence companion star. Shown are slices through the simulation. Color-coded is the logarithm of the density.

mixed into the supernova ejecta. This is in contradiction to the most recent upper limits on hydrogen contamination of the ejecta by Leonard (2007). A way to fix this could be not to look at most massive possible companion stars, but only slightly more massive ones. In this case it might be expected that since the companion is more compact, less material will be

stripped. However, this again reduces the parameter space of single degenerate models that can accrete up to the Chandrasekhar mass in the first place.

5 Codes

This chapter presents the different codes used for this work. As for most numerical calculations, existing, but heavily modified codes were used, the basics of the codes are only discussed briefly. Emphasis is placed on the modifications and extensions of the codes that were developed for this work, which are explained in detail. To solve the equations of hydrodynamics, two fundamentally different approaches, a Lagrangian smoothed particle hydrodynamics code and an Eulerian grid code are used. Both are discussed separately in the following two sections. Using both code together for one model requires to map from a particle distribution onto a grid and vice versa. The methods used for the mapping are discussed in section 5.3.

5.1 Stellar Gadget

GADGET (Springel, 2005) is a smoothed particle hydrodynamics (SPH) code. One of its distinguished features is its scalability. Using a hybrid MPI/pthread parallelization scheme it can be used efficiently for small problems on small machines as well as for big problems on large supercomputers with more than 10^9 SPH particles (Gottloeber et al., 2006). With a few exceptions (e.g., Morris & Podsiadlowski, 2006, 2007), it was so far only used for cosmological simulations. Thus, to apply it to stellar astrophysics, several modifications and extensions were needed:

- Solving the energy equation instead of the entropy equation that is chosen by default in the original GADGET code
- Fixing the gravitational softening of the particles to their individual smoothing length
- A stellar equation of state that accounts for an arbitrarily degenerate and relativistic electron gas, radiation and electron-positron pairs

- A state of the art nuclear reaction network coupled to hydrodynamics
- A wakeup mechanism that treats fast shocks accurately within a scheme that assigns individual time-step to all particles
- A method to generate reasonably stable initial conditions from one-dimensional input models
- A relaxation scheme that stabilizes the initial conditions and removes numerical noise introduced by the setup

The basic equations and their implementation in the GADGET code are described in Springel (2005). We use the latest development version GADGET3 as basis for our modifications. It contains several technical improvements that reduce memory consumption and increase the performance. We always restrict our simulations to particles of equal mass. This avoids numerical problems in regions where particles of considerably different masses interact. As usual, each particle represents some amount of mass m_i at a position $\vec{r}_i$ with a velocity $\vec{v}_i$. Our thermodynamical variable of choice is the internal energy u_i. In addition we introduce the nuclear composition $\vec{X}_i$ of a particle. The following part will describe our modifications and extensions in more detail.

5.1.1 Energy equation

In contrast to the original implementation in GADGET that uses the entropy equation, we solve the energy equation. This is mainly due to convenience, as using the internal energy as conserved variable makes it easier to connect the hydrodynamics with a nuclear reaction network. We use the energy equation in the form

$$\begin{aligned}\frac{\mathrm{d}u_i}{\mathrm{d}t} = -\sum_{j=1}^{N} \frac{m_j}{2} \quad & \left[\frac{P_i}{\rho_i^2} \nabla_i W\left(\left|\vec{r}_i - \vec{r}_j\right|, h_i\right) + \right. \\ + \quad & \frac{P_j}{\rho_j^2} \nabla_i W\left(\left|\vec{r}_i - \vec{r}_j\right|, h_j\right) + \\ + \quad & \left. \Pi_{ij} \vec{v}_{ij} \cdot \nabla_i \overline{W_{ij}} \right] \\ + \quad & \frac{\mathrm{d}e_{nuc,i}}{\mathrm{d}t} \end{aligned} \tag{5.1}$$

where ρ_i is the density at the position of a particle; P_i, h_i are its pressure and smoothing length. $W(r,h)$, $\overline{W_{ij}}$ and Π_{ij} are the kernel function the symmetrized kernel and the artificial viscosity tensor as defined in Springel (2005). The sum includes all neighbors of a particle that are closer than the maximum of the smoothing lengths of the particle and its neighbor. The nuclear energy release due to changes in the composition of a particle by nuclear reactions is represented by $e_{nuc,i}$.

5.1.2 Gravitational softening

The gravitational force between two point-particles diverges as the distance between them approaches zero. To avoid this divergence, the mass of the particles is assumed to be smeared out over a finite volume instead of a discrete point mass. The form of the density distribution function $W(r, h_{\mathrm{SPH}})$ used is identical to the kernel function used in the SPH part. In cosmological simulations, the gravitational softening length h_{Grav} is usually the same for all collision-less (dark matter) particles. To treat the gravitational forces of the SPH particles consistently, the same softening length is used for them as for the collision-less particles. It is, however, sometimes difficult to choose an appropriate softening length that holds for all particles. As we only use SPH particles, and these particles already have a characteristic size given by their smoothing length, we use the smoothing length also as gravitational softening length. While this choice significantly improves the stability of compact objects, it comes at a prize. Changing the smoothing length of a particle now also changes its gravitational potential. This can potentially lead to errors in the total energy of the system for large changes of the smoothing length, but should not be a problem for our models. As described in Price & Monaghan (2007), there is a way to get rid of this drawback completely, by adding additional terms to the evaluation of the gravitational force, that we plan to implement in the future.

5.1.3 Equation of state

The equation of state (EOS) contains all intrinsic properties of the material. It is needed to relate the thermodynamical quantities internal energy u, temperature T and pressure P with each other, given density and composition. For an ideal gas, this can be solved analytically. For white dwarf matter, however, the EOS is more difficult and includes several different components. It is usually split into four parts:

$$p = f_{EOS}\left(\rho, T, x_i\right) = p_{nuclei} + p_{electrons} + p_{positrons} + p_{radiation} \tag{5.2}$$

The nuclei are treated as ideal gas. Electrons and positrons are described as an arbitrarily degenerate and relativistic Fermi gas. All nuclei are assumed to be completely ionized. The radiation is treated as a black body with the local temperature according to the Stefan-Boltzmann law. The nuclei and radiation parts are easy to compute, the part of the electrons and positrons, however, require the evaluation of Fermi integrals (Cox & Giuli, 1968). As this is computationally very demanding, the contributions of electrons and positrons to pressure and internal energy are tabulated depending on density, temperature and electron fraction y_e. The table is derived from the Timmes EOS (as described in Timmes & Arnett, 1999) that solves the Fermi integrals to very high numerical precision. The table used for this work ranges from $\log_{10} \rho[\mathrm{gcm}^{-3}] = [1;11]$, $\log_{10} T[\mathrm{K}] = [2;11]$ and $y_e = [0.4;1.0]$. At densities below the tabulated range we assume the electrons to be an ideal gas. To get the pressure or internal energy for a given temperature, density and electron fraction we interpolate trilinearly in this table.

As the internal energy is our thermodynamical variable of choice, most calls of the EOS, have the internal energy as input. As it is in general not possible to invert the EOS in a closed

form, it is necessary to iterate on the temperature first. This iteration is done using a Newton method. Then all other quantities are calculated using the temperature. Due to numerical errors (e.g. the internal energy is smaller then the energy of the degenerate electron gas), it may not be possible to find a valid temperature for a given internal energy. In this case, or if the temperature drops below the minimum temperature allowed, we assign a temperature of 100K and calculate all other quantities but the internal energy from this temperature.

5.1.4 Nuclear reaction network

SPH is a purely Lagrangian method, thus the composition of a particle can only be changed by nuclear reactions. As the nuclear reactions depend only on local quantities, they can be computed independently of the equations of hydrodynamics. The change of the abundance of one species is given by

$$\frac{\mathrm{d}Y_j}{\mathrm{d}t} = \sum_k \mathcal{R}_k \left(\rho, T, \vec{Y}\right) \tag{5.3}$$

where $Y_j = \frac{X_j}{A_j}$ is the number fraction of the particles and the sum includes all nuclear reactions that create or destroy nuclei j. The reaction rates depend on density, temperature and abundances of all reactants involved. They are taken from the latest (2009) release of the REACLIB database (Rauscher & Thielemann, 2000). As the timescales for nuclear reactions are much smaller then the dynamical dynamical timescale, it is possible to assume that the density is constant over a hydrodynamical time-step. This is, however, in general not a good approximation for the temperature. As the nuclear reactions release energy, the temperature increases. Since the reaction rates depend on the temperature to a high power, this has to be included when the reaction network is evolved. This is done by adding an additional equation to the network, which changes the temperature according to the energy release from the network.

$$\frac{\mathrm{d}T}{\mathrm{d}t} = \frac{\mathrm{d}E}{\mathrm{d}t}\frac{\partial T}{\partial E}\bigg|_{\rho=\mathrm{const}} + \sum_{j=1}^{N_{species}} \frac{\mathrm{d}Y_j}{\mathrm{d}t}\frac{\partial T}{\partial Y_j} \tag{5.4}$$

Together with equation 5.3 for all species this creates a network of $N_{species}+1$ partial differential equations with $N_{species}+1$ variables. As the nuclear reactions in our scenario typically act on timescales much smaller than the dynamical timescale, it is reasonable to integrate the reaction network separately from the hydrodynamics. So for each hydrodynamical time-step of a particle, the nuclear network is evolved over several internal time-steps for the same timespan using the Bader-Deuflhard method (Bader & Deuflhard, 1983) and the method described in Deuflhard (1983) to determine the network time-steps. We restrict evolving the nuclear network to all particles with a temperature higher than 10^7K. For our purpose this is a very conservative estimate, as carbon burning only starts at around 10^9K.

After evolving the nuclear network for the duration of the hydrodynamical time-step, the composition of a particle is changed according to the nuclear reaction network. Knowing the rate of change of the abundances of the different species, we can also calculate the amount

of energy that is released or consumed by nuclear reactions.

$$\frac{\mathrm{d}e_{nuc}}{\mathrm{d}t} = \sum_{j=1}^{N_{species}} N_A \, M_j c^2 \, \frac{\mathrm{d}Y_i}{\mathrm{d}t}. \tag{5.5}$$

Here, N_A is Avogadro's constant and $M_j c^2$ is the rest mass energy of species j. This is then included as a source term in the energy equation 5.1.

5.1.5 Wakeup mechanism

GADGET assigns individual time-steps to all particles, depending on the conditions in their local environment, and evolves each particle on its own time-step. While this greatly reduces the computational costs to run a simulation, it can cause severe problems if strong shocks are involved. A good example for these problems is the shock wave of a supernova hitting its companion star as shown in chapter 4. The outermost, fastest particles of the supernova ejecta travel at a velocity of $2 \cdot 10^9$cm s^{-1}. The outermost particles of the companion star have a smoothing length of about $5 \cdot 10^{10}$cm and a local time-step of 77 s. Thus, during one of their time-steps, the supernova particles can cross a distance about three times their smoothing length without being noticed. Only when the star particles become active, they recognize the supernova particles and their next time-step will be much smaller. As this behavior can obviously lead to completely unphysical results, we implement a so-called "Wakeup mechanism". Similar to the method proposed by Saitoh & Makino (2009), it should wake up inactive particles as other particles approach them which evolve on much slower time-steps.

The hydrodynamical time-step of a SPH particle is calculated as

$$\Delta t_i = \frac{C_{\mathrm{courant}} \, h_i}{\max_j (v_{ij}^{\mathrm{signal}})} \tag{5.6}$$

where C_{courant} is the Courant factor, h_i the smoothing length of the particle and denominator on the right side of the equation finds the maximum of the signal velocities between this particle and all its neighbors as defined in Springel (2005) (equation 13). The resulting maximum signal velocity of a particle is stored. In each time-step we then check for all active particles, whether there are any inactive neighbors having a maximum signal velocity that is smaller than the newly calculated signal velocity between the active particle and its inactive neighbor. If yes, we flag the particle to be woken up.

$$v_i^{\mathrm{maxsignal}} < w \cdot v_{ij}^{\mathrm{signal}} \tag{5.7}$$

Our usual choice for the wakeup factor w is 4.1. The check can be done very efficiently, as the active particle has to loop over all its neighbors anyway to calculate the local pressure force. After finishing the time-step, we change the time-step of all particles that have been flagged to wake up so that they become active in the next global time-step. After a particle has been active in a time-step, its properties are predicted half a time step into the future using their actual rates of change. Thus, we have to correct this extrapolation when we shorten the

time step afterwards by the difference between the estimated time step and the time step the particle really experiences until it becomes active again. This correction is done consistently for all quantities.

5.1.6 Initial conditions

To setup a compact object in GADGET we start from a one-dimensional model of it. We then have to find a stable three-dimensional particle distribution, that represents the density and pressure profile of this model. We use three different methods to construct the particle distribution:

A) Random shell method

B) Cube deformation method

C) Healpix method

First, we will describe all methods in detail, then we will show how they compare to each other for a specific example.

Random shell method

The idea of this method is to divide the object into several (typically ~ 1000) shells of equal radius. We then calculate the mass each shell contains. As all particles should have the same mass this immediately tells us how many particles we have to put into each shell. Assuming that the density is constant in one shell, we calculate a random position in this shell for each particle we put into it. As the particles should be uniformly distributed in the volume of the shell, we calculate the position of a particle as

$$\begin{aligned} r &= \left(\text{random}() \cdot \left(r_{\text{upper}}^3 - r_{\text{lower}}^3\right) + r_{\text{lower}}^3\right)^{\frac{1}{3}} \\ \theta &= \text{random}() \cdot 2\pi \\ \phi &= \text{acos}\left(2 \cdot \text{random}() - 1\right) \end{aligned}$$

Here, r_{lower} and r_{upper} are the lower and upper radius of the shell and random() is a uniform random number in the range $[0,1]$. To obtain the random numbers the Mersenne twister (Matsumoto & Nishimura, 1998) algorithm is used. The initial velocity of all particles is set to zero. The internal energy and composition of a particle is set to the values of the initial one-dimensional model at a radius equal to the radial coordinate of the particle.

Cube deformation method

The cube deformation method starts from a three-dimensional cubical uniform Cartesian grid of particles. This cube is then deformed so that it resembles the intended density profile. The initial grid has to be large enough to cover a sphere that contains the number of particles we want to have in our object. We start by setting the origin of our system of coordinates to

the center of the cube. Then we sort all particles according to their distance from the origin. As in the random shell method, we divide our initial one-dimensional profile into shells and calculate the number of particles we want to put into each shell. We then start to fill up the shells starting from the center using the particles in order of their distance to the center. For the i-th particle in a shell we calculate its new radial coordinate by

$$r_i^{\text{new}} = \left(\frac{i+1}{N_{\text{shell}}} \cdot \left(r_{\text{upper}}^3 - r_{\text{lower}}^3 \right) + r_{\text{lower}}^3 \right)^{\frac{1}{3}} \tag{5.8}$$

where r_{lower} and r_{upper} are the lower and upper radius of the shell, N_{shell} is the number of particles in the shell. Its new position is then given by

$$\vec{x}_i^{\,\text{new}} = \vec{x}_i^{\,\text{cube}} \cdot \frac{r_i^{\text{new}}}{\left| \vec{x}_i^{\,\text{cube}} \right|}. \tag{5.9}$$

Finally, the internal energy and composition of the particle is set to the values of the initial one-dimensional model at a radius equal to its new radial coordinate.

Healpix method

The healpix method tries to find an initial setup, where a roughly cubical volume is attributed to all particles. To this end it uses the healpix library (Górski et al., 2005) to tessellate the surface of a sphere into $12 \cdot n^2$ approximately quadratical pieces of the same area with the healpix number n being a non-negative integer. The idea is to construct the star from several shells where the width of the shells is chosen such that it is of the same size as the edges of the pieces. This condition can be satisfied using a simple method to determine the width of the shells.

We start to construct the star shell by shell from the center. Thus, we always know the lower radius r_{lower} of a shell and want to determine is upper radius r_{upper}. For a given upper radius, the width of a shell and its mass is given by

$$d_{\text{shell}} = r_{\text{upper}} - r_{\text{lower}} \tag{5.10}$$

$$m_{\text{shell}} = 4\pi \int_{r_{\text{lower}}}^{r_{\text{upper}}} \rho(r) \mathrm{d}r. \tag{5.11}$$

The mass increases with increasing r_{upper}. As we fix the uniform particle mass in the beginning, we can then calculate the number of particles that need to be placed in this shell as

$$N_{\text{particles}} = \frac{m_{\text{shell}}}{m_{\text{particle}}}. \tag{5.12}$$

This translates into an healpix number of

$$n_1^{\text{healpix}} = \sqrt{\frac{m_{\text{shell}}}{12 \cdot m_{\text{particle}}}}, \tag{5.13}$$

which also increases with increasing width of the shell. The other constraint on our shell is the requirement of cubical volumes. The surface area of a shell is approximately given by

$$S = 4\pi r^2 = 4\pi \left(r_{\text{lower}} + r_{\text{upper}} \right)^2 . \tag{5.14}$$

As each shell contains $12 \cdot N^2$ particles, the approximate edge size of one piece on the surface can be written as

$$a_{\text{particle}} = \sqrt{S_{\text{particle}}} = \sqrt{\frac{\pi}{12}} \left(r_{\text{lower}} + r_{\text{upper}} \right) \frac{1}{n_2^{\text{healpix}}}. \tag{5.15}$$

This edge size should be equal to the width of the shell. Solving for the healpix number leads to

$$n_2^{\text{healpix}} = \sqrt{\frac{\pi}{12}} \frac{r_{\text{lower}} + r_{\text{upper}}}{r_{\text{upper}} - r_{\text{lower}}}. \tag{5.16}$$

As the upper radius of the shell increases, this second healpix number decreases. Therefore we can always find an upper radius at which both healpix numbers are equal. Having found this radius, we place a shell of particles at the center of the shell using the coordinates from the healpix library and continue with the next shell. Internal energy and composition of the particle are chosen according to the radial coordinate of the particles.

Comparison

Figure 5.1 shows a comparison of the initial conditions with the same number of particles generated for the same $0.9 M_\odot$ white dwarf. The random shell method clearly shows the largest scatter for the density. This is a direct consequence of the Poisson noise introduced by the setup. It leads to local clustering of particles, which in turn influences the density estimate. SPH by construction estimates the density only at the positions of the particles, and there are more particles in over-dense than in under-dense spots. Thus, the average density of the particles is significantly overestimated. In fact, the configuration obtained by the random shell method tends to be not stable. Compared to that, the cube deformation method shows considerably less noise. It also leads to correct density estimates throughout most of the star. Only at the outermost parts, where the number of particles becomes small, the density is overestimated for some particles. The averaged density estimated there, however, is still quite good. The healpix method eventually shows the smallest scatter. The very regular setup avoids any noteworthy discrepancies from the initial density profile.

5.1.7 Relaxation

To get rid of numerical noise introduced by the setup, we relax the object before we start the actual simulation. To this end we use two different approaches, active and passive relaxation.

For *passive relaxation* the object is evolved for several dynamic timescales (for white dwarfs typically for 100s) using the GADGET code. Thus, only artificial and numerical

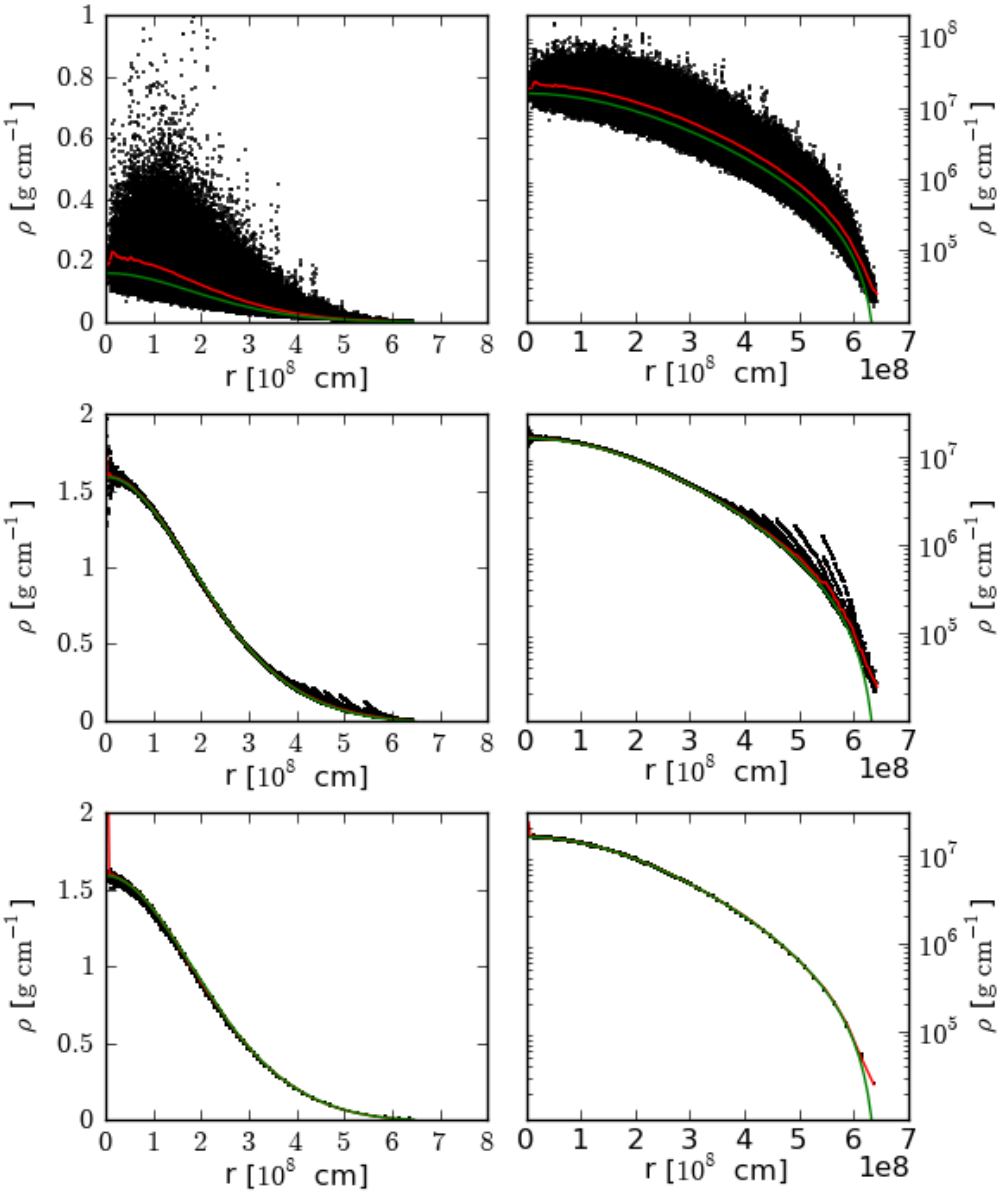

Figure 5.1: Comparison of the initial conditions of a $0.9 M_\odot$ white dwarf generated by the random shell method (top row), the cube deformation method (middle row) and the healpix method (bottom row). Black points show radius actual SPH density of all particles. The green line shows the initial one-dimensional density profile. The red line is the average of the densities of the particles at a given radius. Left and right column show the same data, but use a linear/logarithmic scale for the density.

viscosity dampen the initial noise. As this is quite inefficient, the *active relaxation* adds an explicit damping force similar to that used in Rosswog et al. (2004) that slows down motions.

$$\frac{\mathrm{d}\vec{v}_i}{\mathrm{d}t} = -\frac{\vec{v}_i}{\tau} \tag{5.17}$$

The damping timescale τ controls the strength of the damping term. The smaller it is, the

stronger is the damping. We vary the damping timescale with time as

$$\frac{1}{\tau} = \begin{cases} \dfrac{1}{\tau_0} & t \leq 0.2\ t_{\max} \\ \dfrac{1}{\tau_0 \cdot 10^{\frac{3(t-0.2\ t_{\max})}{0.6\ t_{\max}}}} & 0.2\ t_{\max} \leq t \leq 0.8\ t_{\max} \\ 0 & t > 0.8\ t_{\max} \end{cases} \tag{5.18}$$

The total time the relaxation is run for, $t_{\max}$, should be chosen to be at least several dynamical timescales. The initial damping timescale τ_0 should be much smaller than the dynamical timescale. In the beginning we use a strong damping. After some time, we reduce it continuously until it is switched off completely. If the relaxation was successful, the particle motions will now stay close to zero, even without a damping force. Otherwise, assuming that the initial model is not intrinsically unstable, the relaxation parameters have to be adjusted. Typical choices for a white dwarf applied in this work are $\tau_0 = 0.002$s and $t_{\max} = 100$s.

5.2 LEAFS

LEAFS is a three-dimensional grid-based finite volume hydrodynamics code. It is designed in particular to model thin flames in astrophysical objects, where the burning in the flame is dynamically important. The code uses an uniform Cartesian grid. It is based on the Prometheus code by Fryxell et al. (1989), its basics are described in Reinecke (2001). The equations of hydrodynamics area are solved using the Piecewise Parabolic Method (PPM) (Colella & Woodward, 1984) and an approximate Riemann solver for real gases by Colella & Glaz (1985). The equation of state described above (Section 5.1.3) is also used in this code. The burning front is modeled using the levelset technique. There it is associated with the zero-level of a signed distance function – positive in the ashes and negative in the fuel. The fraction of each computational cell swept by the burning front in a time step is burned at once into ash and the difference in binding energy between fuel and ash increases the internal energy of the cell. The composition of the ashes and the velocity the flame is propagated with are tabulated depending on the fuel density. Following the first version of the code, several important improvements have been made.

Whereas the original implementation was only able to follow subsonic deflagration flames, modifications have been made to enable it to model detonations also (Golombek & Niemeyer, 2005; Röpke & Niemeyer, 2007). Our simulations only contain detonations, thus we do not make use of the implementation of the deflagration. The tables that determine the final burning products have been calibrated by an iterative procedure using the large post processing network under the assumption that the fuel consists of 50% carbon and 50% oxygen (Fink et al., 2010). Above $\sim 10^7$g cm^{-3} the fuel is burned to iron group elements. Below $\sim\ 2 \cdot 10^6$g cm^{-3} only carbon burns to oxygen. In between the fuel is converted to intermediate mass elements. The velocity of the burning front is taken from Gamezo et al. (1999). To determine the pre-shock density, we store the density of all cells that are further

away from the burning front than 6 cells separately in each time step. As the detonation propagates supersonically, the material ahead of the shock front is unaffected by the shock. Thus, when the burning front crosses a cell, we can use its last stored density value in good approximation as the pre-shock density.

After a supernova explosion, its ejecta expand rapidly. To be able to follow them to homologous expansion, an expanding grid was implemented (Röpke, 2005). It increases the size of all grid cells at same rate as the expanding explosion cloud, therefore keeping the grid uniform.

In contrast to explosions of Chandrasekhar mass white dwarfs, a merger of two white dwarfs creates a very asymmetric object. As this object explodes, the original monopole gravity approximation is not sufficient. To treat the gravitational forces accurately, a new gravity solver based on a Fast Fourier Transformation was implemented. To avoid errors from the periodicity of the FFT, it is done on a box twice as large as our hydro grid. Outside the hydro grid, it is padded with zeros. This approach requires to perform the FFT on a grid twice as large as the hydrodynamics grid. Unfortunately this strongly dominates the computing time. Therefore, to save computing time, we interpolate the density linearly on a grid that is coarser by a factor of two, solve the FFT on it and interpolate the resulting potential back onto the finer grid. This still leads to a very accurate gravitational potential (the relative difference is smaller than 10^{-3}) and speeds up the whole simulation significantly. For both interpolations, we use the three-dimensional tri-linear stencil by Mohr & Wienands (2004).

The LEAFS code includes an approximate description of nuclear burning that contains only five species (He, C, O and one representative each of intermediate mass elements and iron group elements) Thus, the details of nucleosynthesis have to be recovered from the simulation data in a post-processing step. For this purpose, equal-mass Lagrangian tracer particles (typically about 10^5) are distributed in the object when it is mapped onto the grid. These particles are passively advected with the flow and their thermodynamical trajectories are recorded. The trajectories are input to a reaction network calculation which involves 384 nuclei (Travaglio et al., 2004). From this, the detailed composition of the final ejecta is obtained. It is a non-trivial task to create an initial tracer distribution that resembles the mass distribution, as the mass is distributed very non-uniformly. The procedure used is described in section 5.3.

5.3 Mapping

As we use both, grid (PPM) and particle (SPH, tracer) methods together to simulate one model, we need to be able to map from a grid to a particle distribution and vice versa.

5.3.1 Grid to particles

There are two important steps where we have to map from a grid to particles. The first step is generating the initial conditions for the SPH simulations. There, we apply special methods that make use of the spherical symmetry of the stellar models. These methods are described in Section 5.1.6. Finding the initial distribution of the tracer particles is the second step. In this case we need to find a particle distribution that represents an arbitrary, irregular density field. To achieve this, we use a Monte Carlo approach. We start by assigning to each cell the probability that one tracer particle should be placed into it. As we want to resemble the mass distribution, this probability is given by the relative mass of the cell compared to the total mass on the grid.

$$p_i = \frac{m_i}{M_{\text{tot}}} \tag{5.19}$$

Then we draw uniformly distributed random points on the grid. For each point we determine its parent cell. As we use an uniform Cartesian grid, the probability to find a point in a cell is the same for all cells. Knowing the cell, we draw another uniform random number in the range $[0, 1]$. If this number is smaller then the probability p_i of this cell, we accept the point and place a tracer particle there. Otherwise we reject the point and continue to draw another one. As soon as we reach the intended number of tracer particles, we stop. As we can do several points at the same time, this method is easy to parallelize.

5.3.2 Particles to grid

Mapping a particle distribution onto a grid is necessary to change from SPH to PPM when the detonation starts in the merger simulations and to reconstruct the final detailed abundances of the supernova explosion from the tracer particles on a grid to be used for radiative transfer.

To map from SPH to a grid, we can directly use the SPH prescription to calculate the density at any point $\vec{r}_i$ in space using the kernel function $W(|r|, h)$.

$$\rho(\vec{r}_i) = \sum_j m_j W(|\vec{r}_j - \vec{r}_i|, h) \tag{5.20}$$

The smoothing length h_i of a particle at position $\vec{r}_i$ is given by

$$\frac{4\pi}{3} h_i^3 \rho_i = N_{sph} m, \tag{5.21}$$

where m is the mass of one particle. Together with equation 5.20, this equation has to be solved iteratively to determine h_i. We use the standard GADGET kernel function

$$W(\vec{r}, h) = \frac{8}{\pi h^3} \begin{cases} (1 - 6u^2 + 6u^3) & 0 \le u \le \frac{1}{2} \\ 2(1-u)^3 & \frac{1}{2} \le u \le 1 \\ 0 & u > 1 \end{cases} \tag{5.22}$$

with $u = r/h$.

By evaluating the density at the center of each grid cell and using the result as value for the cell, we construct a density grid. There are three possible choices for the smoothing length h, which lead to the same results if all particles have the same smoothing length, but differ for variable smoothing lengths.

The possibilities to choose h are:

- $h = h_i$: the *gather* approach
  To calculate the density at the position of a particle, all other particles within a sphere with the radius of the smoothing length of this particle contribute. This also guarantees that only a limited number of local particles contribute and it can be evaluated locally. However, if we want to use this approach to map SPH particles on a grid, we first have to calculate the smoothing lengths of hypothetical particles at the centers of the grid cells.

- $h = h_j$: the *scatter* approach
  All particles contribute to all points closer than the smoothing length of the particle. Therefore it is possible that particles with a large smoothing length also contribute to points in the local neighborhood of particles with a much smaller smoothing length. In this case, many more particles than the average number of neighbors can contribute to some points. This approach has the advantage that we do not need to compute any smoothing lengths, as we already know the smoothing lengths of the particles when we map SPH particles on a grid.

- $h = f(h_i, h_j)$: a mixture of both approaches described above
  We do not consider this as a useful approach to our problem, as it combines the disadvantages (need to compute smoothing lengths, contributions from distant particles) of both other approaches.

SPH particles to hydro grid

Typically the number of SPH particles ($\sim 10^6$) is by far lower than the number of grid cells (512^3). Thus, although SPH is highly adaptive, the resolution of the uniform grid is still better than the smallest smoothing length and we are able to resolve all structure of the SPH simulation on the grid. To map the SPH particles on the grid, we only use the scatter approach, as it saves us the computation of additional smoothing lengths. In addition to the density, we compute the velocity components v_x, v_y, v_z, the internal energy u and the nuclear mass fractions X_k of the cell by

$$A_i = \frac{\sum_j A_j m_j W(|\vec{r}_j - \vec{r}_i|, h_j)}{\sum_j m_j W(|\vec{r}_j - \vec{r}_i|, h_j)} = \frac{1}{\rho(\vec{r}_i)} \sum_j A_j m_j W(|\vec{r}_j - \vec{r}_i|, h_j) \tag{5.23}$$

where A is to be replaced by the particular scalar quantities. The density ρ_j of the SPH particles is not needed. All other thermodynamical quantities are then calculated from the equation of state.

Tracer particles to radiative transfer grid

Extracting an abundance grid from the tracer particles is a different task. The tracer particles are similar to the SPH particles as they are Lagrangian, but they are advected with the flow rather than subject to real hydrodynamical and gravitational forces. Just sorting the tracer particles into cells, however, does not work, as we typically have only 150000 tracer particles compared to 50^3 grid cells on the radiative transfer grid. Thus there are many cells that do not contain any tracer particle. To avoid this problem, and to find reasonable values for all cells, we use an SPH-like approach for the mapping. So we define a "smoothing length" for each particle and then use the SPH approach to construct the grid.

We consider three different ways to find the smoothing length of a particle:

A) Solving equation 5.21 for the smoothing length

$$h_i = \left(\frac{3 N_{sph} m_i}{4 \pi \rho_i} \right)^{\frac{1}{3}} \tag{5.24}$$

As we know the mass of the tracer particle and the density at its position, we can define some number of neighbors N_{sph} and use this equation to calculate a smoothing length for the particle. This approach is quite fast and gives reasonable, adaptive results. However, there is no intrinsic reason that using the hydrodynamic density here is justified.

B) Treating the tracer particles completely like SPH particles
So we solve equations 5.20 and 5.21 iteratively for a given N_{sph} for each particle. In this case the number of "real" neighbors, i.e. the number of neighbors of a particle closer than its smoothing length can differ from N_{sph}.

C) Choosing the smoothing length by the number of neighbors directly
In contrast to the definition by equation 5.21, we define the smoothing length of a particle as the radius of a sphere around it that contains exactly N_{sph} other particles. Using the gather-approach to calculate other quantities at a given point, this definition ensures that always the same number of most nearby particles contribute to that point.

To do the radiative transfer we need to know density and composition on a grid. We take the density from the hydrodynamics output. So the tracer particles only influence the composition. Therefore, it is not important, whether we get a good density estimate from the tracer particles, but only that the composition on the grid conserves the global and local abundance distribution. Given that we typically use 150000 tracer ($> 50^3$), the global composition of the tracer particles should be converged (Seitenzahl et al., 2010). If the grid resolution is comparable or better than the tracer resolution, also the global composition on the grid is well conserved, no matter which approach we use. To conserve the abundances locally is more difficult. In addition, the radiative transfer results not only depend on the structure of the distribution of the different elements, but also on their precise position. Considering this, our best choice is to use the gather approach together with a choice of the smoothing length that guarantees that always the same number of particles contribute.

This way we avoid any contamination of the composition in a specific region by distant, but "large" particles. Such a contamination is a natural result of a larger smoothing length or the scatter approach and typically smears out the composition over larger scales and can lead to significant differences in the synthetic observables derived from subsequent radiative transfer simulations.

6 Summary

The goal of this thesis was to shed light on the two fundamental questions of type Ia supernovae, that of the progenitor system and of that of the explosion mechanism. We investigated both proposed progenitor scenarios, the single degenerate and the double degenerate scenario, in different ways. To find out whether there is an explosion mechanism that leads to a type Ia supernova from a double degenerate progenitor system, we explored mergers of two white dwarfs of similar mass with the aim to determine whether they will lead to thermonuclear explosions and whether a thermonuclear explosion of such a system will look like a type Ia supernova. In a complementary study, we investigated the consequences of the impact of the ejecta of a type Ia supernova explosion on a hydrogen-rich companion star in the single degenerate scenario to find observational constraints on this scenario.

To figure out the final fate of a merging binary system of two white dwarfs, we followed it from the inspiral through its evolution until we finally calculated synthetic spectra and lightcurves. These allowed us to quantitatively compare with observations. Since there are many different physical processes involved, we developed a simulation chain consisting of different codes each used to model a specific phase of the evolution. We adapted the SPH code GADGET to stellar problems to simulate the inspiral and merger of the binary system. Given that the merger leads to the ignition of a detonation, we used the LEAFS code to follow the propagation of the flame and the nuclear burning until the ejecta fly apart and finally reach homologous expansion. Using a large nuclear network, we reconstructed the detailed isotopic composition of the ejecta. Together with the density structure of the ejecta, the composition was used as an input to the radiative transfer code ARTIS to compute synthetic lightcurves and spectra for some of our models. Finally, we compared these in a qualitative and quantitative manner with observational data.

We found, that a merger of two carbon/oxygen white dwarfs with masses of at least

$0.9M_\odot$ and a mass ratio larger than 0.8 to 0.9 is so violent that during the merger itself a detonation forms. This detonation then burns and disrupts the whole merged objects within seconds. Thus we were able to show for the first time, that at least some mergers of white dwarfs can indeed lead to thermonuclear explosions, in contrast to previous assumptions that these systems always end up with an accretion induced collapse (Saio & Nomoto, 1998, 1985). This assumption, however, may still be correct for mergers of two white dwarfs with a smaller mass ratio. In this case, we found that the merger itself is not violent enough, and a detonation therefore cannot form. It still remains a subject to be solved in future studies what mass ratio is exactly required to get a detonation and whether the mass ratio depends on the total mass of both white dwarfs.

We carried out an extensive study of the merger of two carbon/oxygen white dwarfs of $0.9M_\odot$ each. We observed, that they produce only $0.1M_\odot$ of ^{56}Ni and thus are subluminous compared to normal type Ia supernovae (with $M(^{56}\mathrm{Ni}) \sim 0.4$ to $0.8M_\odot$). There is, however, the subclass of 1991bg-like type Ia supernovae, that is also subluminous compared to normal events and has eluded a theoretical explanation so far. We showed, that a merger of two $0.9M_\odot$ white dwarfs leads to a thermonuclear explosion, whose synthetic observables are in excellent agreement with observed 1991bg-like supernovae. We found, that qualitatively it shares all important features of the lightcurve and the spectra, and that synthetic and observed lightcurves and spectra also agree very well quantitatively.

Moreover, we explored the mergers of two carbon/oxygen white dwarfs of more and less mass, again with a mass ratio close to one. We found, that changing the mass changes how violent the merger is. More massive white dwarfs have smaller radii, and have thus deeper gravitational potentials. Thus, the mergers becomes more violent and the conditions are more favorable for the formation of a detonation. We observed, that less massive mergers with white dwarf masses of $0.8M_\odot$ or smaller will probably not end up in a thermonuclear explosion. For mergers with masses larger or equal to $0.9M_\odot$ and a mass ratio close to one, however, the formation of a detonation and a subsequent thermonuclear explosion seem hard to avoid.

Our simulations showed that with increasing mass of the primary, more massive white dwarf the amount of ^{56}Ni produced in the explosion increases and the explosion becomes brighter. In the most massive merger of a $1.0M_\odot$ with a $1.2M_\odot$ white dwarf, $\sim 1.0M_\odot$ of ^{56}Ni was synthesized. This at the same time is an upper limit for the amount of ^{56}Ni produced in the merger of two carbon/oxygen white dwarfs, since such white dwarfs are born with a maximum mass of $1.2M_\odot$ and because the secondary white dwarf is destroyed in the merger only in the primary white dwarf the density is high enough to produce ^{56}Ni in the explosion. Therefore, in contrast to previous speculations (Howell et al., 2006), we can now exclude the merger of two carbon/oxygen white dwarfs as progenitor system of the most luminous type Ia supernovae, that require $1.2M_\odot$ to $1.7M_\odot$ of ^{56}Ni (Howell et al., 2006; Hicken et al., 2007; Silverman et al., 2010, see, e.g.). However, it may still be possible, that they are the result of a merger of a carbon/oxygen white dwarf with an oxygen/neon white dwarf (which can have a mass up to the Chandrasekhar-mass). This should be investigated in the future.

The second part of the this thesis aimed at finding direct constraints to the single degenerate progenitor system from observations. To this end, we modeled the impact of the supernova ejecta on the companion of the exploding white dwarf in the single degenerate progenitor scenario. As in this scenario the companion star is typically hydrogen-rich, some hydrogen-rich material is stripped from the companion star by the impact and mixed into the ejecta. We found, that the amount of hydrogen mixed into the ejecta is of the order of only $0.01 M_{\odot}$. This is significantly less than predicted by previous results of Marietta et al. (2000). The main reason for this difference is a modified, more compact stellar structure of the companion star resulting from a more realistic treatment of the binary evolution in combination with a resulting variation in the separation distance of the progenitor system. In particular the more compact state of the companion impedes the mass loss in the impact.

The reduced amount of hydrogen mixed into the ejecta of the supernova as predicted by our simulations leads to an agreement with observational studies of type Ia supernova nebular spectra (Mattila et al., 2005; Leonard, 2007). This removes the former disagreement between the available observations and simulations of the single degenerate progenitor system. Thus, to current knowledge, the progenitor scenario is admissible in the context discussed here. However, since the hydrogen masses predicted by our simulations are not far below the current observational upper limits, it may be possible in the near future to confirm or reject the studied progenitor scenario by either detecting hydrogen in type Ia supernovae, or lowering the limits by another order of magnitude. A stringent way of analysis would be to calculate synthetic spectra directly from the presented simulations and to compare the results with observations. This should be done in further studies.

This work stands for a significant step on the path to understand the progenitor systems and the explosion mechanism of type Ia supernovae. It showed, that mergers of two white dwarfs are very likely the progenitors of some type Ia supernovae, but are not the dominant systems. In addition, it was demonstrated that hydrogen-accreting single-degenerate progenitor systems are still marginally consistent with observations, but future observations may soon rule them out or confirm them.

Acknowledgements

This work would not have been possible without the support of a lot of people. Thus, I would like to thank them here. Most importantly I want to thank Fritz Röpke and Wolfgang Hillebrandt who gave me the opportunity to work on my thesis at the Max-Planck-Institut für Astrophysik. They also supervised my work and were always happy to discuss my work and provide help when I needed it.

Special thanks go to M. Kromer, who did radiative transfer simulations for most of my merger models and kindly allowed me to use some of his plots in this thesis. Similarly I would like to thank A. Ruiter for population synthesis calculations of the merger scenario which played an important part toward understanding the scenario. U. Nöhbauer deserves my thanks for carefully reading the introduction of this thesis offering his comments. Last but not least, Ludwig and Karl earned my thanks by providing a red pen and thus preventing further delay of this thesis.

I would like to thank all the people who I talked to and worked with at MPA in the last 3.5 years. They helped create a very nice and inspiring atmosphere. In particular, the type Ia supernova group at MPA provided a great working environment. I want to mention A. Marek, F. Miczek, S. Hachinger, F. Ciaraldi-Schoolmann, J. von Groote and all the other people who shared an office with me in the last years. The atmosphere and (sometimes scientific) discussions in our office were just great. It is also important to mention the regular Schafkopf-team consisting of I. Seitenzahl, S. Taubenberger, U. Nöhbauer, S. Sim and all the guests joining us from time to time.

Outside MPA, I would like to thank Gabi, Hätschi, Jens, Klaus and Tina, for all the time we spent together. Finally I am very grateful to my parents for always supporting me, regardless of what I was doing.

Bibliography

Almgren, A. S., Bell, J. B., Rendleman, C. A., & Zingale, M. 2006, ApJ, 637, 922, [arXiv:astro-ph/0509892]

Arafune, J. & Fukugita, M. 1987, Physical Review Letters, 59, 367

Arnett, W. D. 1979, ApJ, 230, L37

Arnett, W. D. 1982, ApJ, 253, 785

Bader, G. & Deuflhard, P. 1983, Numerische Mathematik, 41, 373

Belczynski, K., Kalogera, V., & Bulik, T. 2002, ApJ, 572, 407, [arXiv:astro-ph/0111452]

Belczynski, K., Kalogera, V., Rasio, F. A., et al. 2008, ApJS, 174, 223, [arXiv:astro-ph/0511811]

Benz, W., Cameron, A. G. W., Press, W. H., & Bowers, R. L. 1990, ApJ, 348, 647

Body, K. M. 1997, PhD thesis, Department of Mechanical Engineering, McGill University, Montreal, Quebec, Canada

Branch, D., Fisher, A., & Nugent, P. 1993, AJ, 106, 2383

Bravo, E. & García-Senz, D. 2006, ApJ, 642, L157, [arXiv:astro-ph/0604025]

Chandrasekhar, S. 1931, ApJ, 74, 81

Colella, P. & Glaz, H. M. 1985, Journal of Computational Physics, 59, 264

Colella, P. & Woodward, P. R. 1984, Journal of Computational Physics, 54, 174

Cox, J. P. & Giuli, R. T. 1968, Principles of Stellar Structure, Vol. 2 (New York: Gordon and Breach)

Deuflhard, P. 1983, Numerische Mathematik, 41, 399

Filippenko, A. V. 1997, ARA&A, 35, 309

Fink, M., Hillebrandt, W., & Röpke, F. K. 2007, A&A, 476, 1133, [arXiv:0710.5486]

Fink, M., Röpke, F. K., Hillebrandt, W., et al. 2010, A&A, 514, A53+

Fryer, C. L., Hungerford, A. L., & Rockefeller, G. 2007, International Journal of Modern Physics D, 16, 941

Fryxell, B. A., Müller, E., & Arnett, W. D. 1989, Hydrodynamics and nuclear burning, MPA Green Report 449, Max-Planck-Institut für Astrophysik, Garching

Gamezo, V. N., Wheeler, J. C., Khokhlov, A. M., & Oran, E. S. 1999, ApJ, 512, 827

Gilfanov, M. & Bogdán, Á. 2010, Nature, 463, 924, [1002.3359]

Golombek, I. & Niemeyer, J. C. 2005, A&A, 438, 611, [arXiv:astro-ph/0503617]

Górski, K. M., Hivon, E., Banday, A. J., et al. 2005, ApJ, 622, 759, [arXiv:astro-ph/0409513]

Gottloeber, S., Yepes, G., Wagner, C., & Sevilla, R. 2006, [arXiv:astro-ph/0608289]

Guerrero, J., García-Berro, E., & Isern, J. 2004, A&A, 413, 257

Guillochon, J., Dan, M., Ramirez-Ruiz, E., & Rosswog, S. 2010, ApJ, 709, L64, [0911.0416]

Hachinger, S., Mazzali, P. A., Taubenberger, S., Pakmor, R., & Hillebrandt, W. 2009, ArXiv e-prints, [0907.2542]

Hachisu, I., Kato, M., & Nomoto, K. 1999, ApJ, 522, 487, [arXiv:astro-ph/9902304]

Hachisu, I., Kato, M., & Nomoto, K. 2008, ApJ, 683, L127, [0805.2102]

Han, Z. & Podsiadlowski, P. 2004, MNRAS, 350, 1301, [arXiv:astro-ph/0309618]

Hicken, M., Garnavich, P. M., Prieto, J. L., et al. 2007, ApJ, 669, L17, [0709.1501]

Hicken, M., Wood-Vasey, W. M., Blondin, S., et al. 2009, ApJ, 700, 1097, [0901.4804]

Howell, D. A., Höflich, P., Wang, L., & Wheeler, J. C. 2001, ApJ, 556, 302, [arXiv:astro-ph/0101520]

Howell, D. A., Sullivan, M., Nugent, P. E., et al. 2006, Nature, 443, 308, [arXiv:astro-ph/0609616]

Hoyle, F. & Fowler, W. A. 1960, ApJ, 132, 565

Iben, Jr., I. & Tutukov, A. V. 1984, ApJS, 54, 335

Ivanova, N. & Taam, R. E. 2004, ApJ, 601, 1058, [arXiv:astro-ph/0310126]

Janka, H., Langanke, K., Marek, A., Martínez-Pinedo, G., & Müller, B. 2007, Phys. Rep., 442, 38, [arXiv:astro-ph/0612072]

Jha, S., Branch, D., Chornock, R., et al. 2006, AJ, 132, 189, [arXiv:astro-ph/0602250]

Jordan, IV, G. C., Fisher, R. T., Townsley, D. M., et al. 2008, ApJ, 681, 1448

Kahabka, P. & van den Heuvel, E. P. J. 1997, ARA&A, 35, 69

Kasen, D., Nugent, P., Thomas, R. C., & Wang, L. 2004, ApJ, 610, 876, [arXiv:astro-ph/0311009]

Kasen, D., Röpke, F. K., & Woosley, S. E. 2009, Nature, 460, 869, [0907.0708]

Kato, M. & Hachisu, I. 2003, ApJ, 598, L107, [arXiv:astro-ph/0310351]

Kawabata, K. S., Maeda, K., Nomoto, K., et al. 2010, Nature, 465, 326, [0906.2811]

Kerzendorf, W. E., Schmidt, B. P., Asplund, M., et al. 2009, ApJ, 701, 1665, [0906.0982]

Khokhlov, A., Mueller, E., & Hoeflich, P. 1993, A&A, 270, 223

Khokhlov, A. M. 1991, A&A, 245, 114

Krisciunas, K., Suntzeff, N. B., Candia, P., et al. 2003, AJ, 125, 166, [arXiv:astro-ph/0210327]

Kromer, M. & Sim, S. A. 2009, MNRAS, 398, 1809, [0906.3152]

Kromer, M., Sim, S. A., Fink, M., et al. 2010, ApJ, 719, 1067, [1006.4489]

Langer, N., Deutschmann, A., Wellstein, S., & Höflich, P. 2000, A&A, 362, 1046, [arXiv:astro-ph/0008444]

Leibundgut, B., Kirshner, R. P., Phillips, M. M., et al. 1993, AJ, 105, 301

Leonard, D. C. 2007, ApJ, 670, 1275, [arXiv:0710.3166]

Li, W., Filippenko, A. V., Treffers, R. R., et al. 2001, ApJ, 546, 734, [arXiv:astro-ph/0006292]

Lisewski, A. M., Hillebrandt, W., & Woosley, S. E. 2000, ApJ, 538, 831, [arXiv:astro-ph/9910056]

Livio, M. 2000, in Type Ia Supernovae, Theory and Cosmology. Edited by J. C. Niemeyer and J. W. Truran. Published by Cambridge University Press, 2000., p.33, ed. J. C. Niemeyer & J. W. Truran, 33–48

Livne, E. & Arnett, D. 1995, ApJ, 452, 62

Lorén-Aguilar, P., Isern, J., & García-Berro, E. 2009, American Institute of Physics Conference Series, 1122, 320

Marek, A. & Janka, H. 2009, ApJ, 694, 664, [0708.3372]

Marietta, E., Burrows, A., & Fryxell, B. 2000, ApJS, 128, 615, [arXiv:astro-ph/9908116]

Matsumoto, M. & Nishimura, T. 1998, ACM Trans. Model. Comput. Simul., 8, 3

Mattila, S., Lundqvist, P., Sollerman, J., et al. 2005, A&A, 443, 649, [arXiv:astro-ph/0501433]

Mattila, S., Smartt, S. J., Eldridge, J. J., et al. 2008, ApJ, 688, L91, [0809.0206]

Maund, J. R. & Smartt, S. J. 2009, Science, 324, 486, [0903.3772]

Maund, J. R., Smartt, S. J., & Danziger, I. J. 2005, MNRAS, 364, L33, [arXiv:astro-ph/0507502]

Mazzali, P. A., Chugai, N., Turatto, M., et al. 1997, MNRAS, 284, 151

Mazzali, P. A., Danziger, I. J., & Turatto, M. 1995, A&A, 297, 509

Meakin, C. A., Seitenzahl, I., Townsley, D., et al. 2009, ApJ, 693, 1188, [0806.4972]

Meng, X., Chen, X., & Han, Z. 2007, PASJ, 59, 835

Mohr, M. & Wienands, R. 2004, Computing and Visualization in Science, 7, 129

Morris, T. & Podsiadlowski, P. 2006, MNRAS, 365, 2, [arXiv:astro-ph/0502288]

Morris, T. & Podsiadlowski, P. 2007, Science, 315, 1103, [arXiv:astro-ph/0703317]

Motl, P. M., Frank, J., Tohline, J. E., & D'Souza, M. C. R. 2007, ApJ, 670, 1314, [arXiv:astro-ph/0702388]

Napiwotzki, R., Karl, C., Nelemans, G., et al. 2004, in Revista Mexicana de Astronomia y Astrofisica Conference Series, Vol. 20, Revista Mexicana de Astronomia y Astrofisica Conference Series, ed. G. Tovmassian & E. Sion, 113–116

Niemeyer, J. C. 1999, ApJ, 523, L57, [arXiv:astro-ph/9906142]

Niemeyer, J. C. & Hillebrandt, W. 1995, ApJ, 452, 779

Niemeyer, J. C. & Woosley, S. E. 1997, ApJ, 475, 740, [arXiv:astro-ph/9607032]

Nomoto, K. 1982, ApJ, 253, 798

Nomoto, K. & Kondo, Y. 1991, ApJ, 367, L19

Nomoto, K., Saio, H., Kato, M., & Hachisu, I. 2007, ApJ, 663, 1269, [arXiv:astro-ph/0603351]

Nomoto, K., Thielemann, F.-K., & Yokoi, K. 1984, ApJ, 286, 644

Osher, S. & Sethian, J. A. 1988, Journal of Computational Physics, 79, 12

Paczyński, B. 1967, Acta Astronomica, 17, 287

Pastorello, A., Mazzali, P. A., Pignata, G., et al. 2007a, MNRAS, 377, 1531, [arXiv:astro-ph/0702565]

Pastorello, A., Taubenberger, S., Elias-Rosa, N., et al. 2007b, MNRAS, 376, 1301, [arXiv:astro-ph/0702566]

Patat, F., Chandra, P., Chevalier, R., et al. 2007, Science, 317, 924, [arXiv:0707.2793]

Perets, H. B., Gal-Yam, A., Mazzali, P. A., et al. 2010, Nature, 465, 322, [0906.2003]

Perlmutter, S., Aldering, G., Goldhaber, G., et al. 1999, ApJ, 517, 565, [arXiv:astro-ph/9812133]

Pfannes, J. M. M., Niemeyer, J. C., & Schmidt, W. 2010a, A&A, 509, A75+, [0911.3545]

Pfannes, J. M. M., Niemeyer, J. C., Schmidt, W., & Klingenberg, C. 2010b, A&A, 509, A74+, [0911.3540]

Phillips, M. M., Li, W., Frieman, J. A., et al. 2007, PASP, 119, 360, [arXiv:astro-ph/0611295]

Phillips, M. M., Lira, P., Suntzeff, N. B., et al. 1999, AJ, 118, 1766, [arXiv:astro-ph/9907052]

Phillips, M. M., Wells, L. A., Suntzeff, N. B., et al. 1992, AJ, 103, 1632

Plewa, T., Calder, A. C., & Lamb, D. Q. 2004, ApJ, 612, L37, [arXiv:astro-ph/0405163]

Price, D. J. & Monaghan, J. J. 2007, MNRAS, 374, 1347, [arXiv:astro-ph/0610872]

Rauscher, T. & Thielemann, F.-K. 2000, Atomic Data and Nuclear Data Tables, 75, 1, [arXiv:astro-ph/0004059]

Reinecke, M. A. 2001, PhD thesis, Technical University of Munich, available at http://tumb1.biblio.tu-muenchen.de/publ/diss/allgemein.html

Riess, A. G., Filippenko, A. V., Challis, P., et al. 1998a, AJ, 116, 1009, [arXiv:astro-ph/9805201]

Riess, A. G., Nugent, P., Filippenko, A. V., Kirshner, R. P., & Perlmutter, S. 1998b, ApJ, 504, 935, [arXiv:astro-ph/9804065]

Roelofs, G., Bassa, C., Voss, R., & Nelemans, G. 2008, MNRAS, 391, 290, [0802.2097]

Röpke, F. K. 2005, A&A, 432, 969, [arXiv:astro-ph/0408296]

Röpke, F. K., Gieseler, M., Reinecke, M., Travaglio, C., & Hillebrandt, W. 2006a, A&A, 453, 203, [arXiv:astro-ph/0506107]

Röpke, F. K., Hillebrandt, W., Niemeyer, J. C., & Woosley, S. E. 2006b, A&A, 448, 1, [arXiv:astro-ph/0510474]

Röpke, F. K., Hillebrandt, W., Schmidt, W., et al. 2007a, ApJ, 668, 1132, [arXiv:0707.1024]

Röpke, F. K. & Niemeyer, J. C. 2007, A&A, 464, 683, [arXiv:astro-ph/0703378]

Röpke, F. K., Woosley, S. E., & Hillebrandt, W. 2007b, ApJ, 660, 1344, [arXiv:astro-ph/0609088]

Rosswog, S., Speith, R., & Wynn, G. A. 2004, MNRAS, 351, 1121, [arXiv:astro-ph/0403500]

Ruiter, A. J., Belczynski, K., & Fryer, C. 2009, ApJ, 699, 2026, [0904.3108]

Ruiz-Lapuente, P., Comeron, F., Méndez, J., et al. 2004, Nature, 431, 1069, [arXiv:astro-ph/0410673]

Saio, H. & Nomoto, K. 1985, A&A, 150, L21

Saio, H. & Nomoto, K. 1998, ApJ, 500, 388, [arXiv:astro-ph/9801084]

Saitoh, T. R. & Makino, J. 2009, ApJ, 697, L99, [0808.0773]

Salaris, M., Dominguez, I., Garcia-Berro, E., et al. 1997, ApJ, 486, 413, [arXiv:astro-ph/9704038]

Scalzo, R. A., Aldering, G., Antilogus, P., et al. 2010, ApJ, 713, 1073, [1003.2217]

Schmidt, W. & Niemeyer, J. C. 2006, A&A, 446, 627, [arXiv:astro-ph/0510427]

Seitenzahl, I. R., Meakin, C. A., Townsley, D. M., Lamb, D. Q., & Truran, J. W. 2009, ApJ, 696, 515, [0901.3677]

Seitenzahl, I. R., Röpke, F. K., Fink, M., & Pakmor, R. 2010, MNRAS, 407, 2297, [1005.5071]

Silverman, J. M., Ganeshalingam, M., Li, W., et al. 2010, ArXiv e-prints, [1003.2417]

Sim, S. A., Röpke, F. K., Hillebrandt, W., et al. 2010, ApJ, 714, L52, [1003.2917]

Sim, S. A., Sauer, D. N., Röpke, F. K., & Hillebrandt, W. 2007, MNRAS, 378, 2, [arXiv:astro-ph/0703764]

Sonneborn, G., Altner, B., & Kirshner, R. P. 1987, ApJ, 323, L35

Springel, V. 2005, MNRAS, 364, 1105, [arXiv:astro-ph/0505010]

Stanishev, V., Goobar, A., Benetti, S., et al. 2007, A&A, 469, 645, [0704.1244]

Stehle, M., Mazzali, P. A., Benetti, S., & Hillebrandt, W. 2005, MNRAS, 360, 1231, [arXiv:astro-ph/0409342]

Sullivan, M., Le Borgne, D., Pritchet, C. J., et al. 2006, ApJ, 648, 868, [arXiv:astro-ph/0605455]

Tanaka, M., Kawabata, K. S., Yamanaka, M., et al. 2010, ApJ, 714, 1209, [0908.2057]

Taubenberger, S. 2010

Taubenberger, S., Hachinger, S., Pignata, G., et al. 2008, MNRAS, 385, 75, [0711.4548]

Timmes, F. X. & Arnett, D. 1999, ApJS, 125, 277

Travaglio, C., Hillebrandt, W., Reinecke, M., & Thielemann, F.-K. 2004, A&A, 425, 1029, [arXiv:astro-ph/0406281]

Voss, R. & Nelemans, G. 2008, Nature, 451, 802, [0802.2082]

Wang, L., Baade, D., & Patat, F. 2007, Science, 315, 212, [arXiv:astro-ph/0611902]

Wang, L. & Wheeler, J. C. 2008, ARA&A, 46, 433, [0811.1054]

Weiss, A. & Schlattl, H. 2007, Ap&SS, 341

Woosley, S. E. 2007, ApJ, 668, 1109, [arXiv:0709.4237]

Woosley, S. E., Kasen, D., Blinnikov, S., & Sorokina, E. 2007, ApJ, 662, 487, [arXiv:astro-ph/0609562]

Woosley, S. E., Kerstein, A. R., Sankaran, V., Aspden, A. J., & Röpke, F. K. 2009, ApJ, 704, 255, [0811.3610]

Woosley, S. E. & Weaver, T. A. 1986, ARA&A, 24, 205

Woosley, S. E. & Weaver, T. A. 1994, ApJ, 423, 371

Woosley, S. E. & Weaver, T. A. 1995, ApJS, 101, 181

Yamanaka, M., Kawabata, K. S., Kinugasa, K., et al. 2009, ApJ, 707, L118, [0908.2059]

Yoon, S. & Langer, N. 2005, A&A, 435, 967, [arXiv:astro-ph/0502133]

Yoon, S.-C. & Langer, N. 2004, A&A, 419, 623, [arXiv:astro-ph/0402287]

Yoon, S.-C., Podsiadlowski, P., & Rosswog, S. 2007, MNRAS, 380, 933, [0704.0297]

Yuan, F., Quimby, R. M., Wheeler, J. C., et al. 2010, ApJ, 715, 1338, [1004.3329]

Zel'dovich, Y. B., Librovich, V. B., Makhviladze, G. M., & Sivashinskii, G. I. 1970, Journal of Applied Mechanics and Technical Physics, 11, 264

Zingale, M., Almgren, A. S., Bell, J. B., Nonaka, A., & Woosley, S. E. 2009, ApJ, 704, 196, [0908.2668]